# Role of Thyristor Controlled Series Compensators in Damping Sub-synchronous Resonance in Power Systems

by

Dilini Buddhima Rathnayaka Weerakoon

A thesis submitted to the Faculty of Graduate Studies in partial fulfillment of the requirements for the degree of Doctor Of Philosophy

Department of Electrical and Computer Engineering
The University of Manitoba
Winnipeg, Manitoba, Canada

To my parents, brother and my husband...

# Acknowledgments

The realization of this thesis is owed to the support of many good people. I am grateful to all those who supported me throughout the journey of my PhD.

I am deeply thankful to my advisor, Professor Udaya Annakkage, for his invaluable advices, continuous support, and encouragement throughout the course of this project. I feel privileged to have worked under his supervision. I express my gratitude to my co-advisor, Dr. Chandana Karawita, for his guidance and sharing his expertise, for the advancement of this research. I extend my sincere thanks to the members of my advisory committee, Professor Shaahin Filizadeh and Professor Carl Ho, for their insightful feedback and suggestions provided to this research.

This work would not have been possible without the financial support from RTDS Technologies, MITACS and University of Manitoba. Special thanks to Dr. Yi Zhang from RTDS Technologies for his valuable inputs.

I greatly appreciate the support extended by the team at TransGrid Solutions Inc. The knowledge and experience I've gained at TransGrid Solutions is invaluable. Special thanks to Dr. Hiranya Suriyaarachchi from TransGrid Solutions for his valuable inputs to this research. I also extend many thanks to my friends and the staff of the Department of Electrical and Computer Engineering for their continuous support throughout my time at the University of Manitoba.

I extend my heartfelt gratitude to my parents and brother back home in Sri Lanka for their unwavering support and motivation. I'm also thankful to the companionship and encouragement from my best friend and housemates in Winnipeg. Finally, I sincerely thank my husband for his patience, understanding and belief in me.

Dilini Rathnayaka Weerakoon

August 2024

# Summary

Sub-Synchronous Oscillations (SSOs) have been identified to pose significant challenges to both conventional and modern power grids. Over many years, the power industry has relied on series compensation using Fixed Series Compensators (FSCs) for long distance ac power transmission. However, presence of heavily series compensated lines is one of the major causes for SSOs in the power system. With the availability of Thyristor Controlled Series Compensators (TCSCs), utilities have the option of using them instead of FSCs to exploit the advantage of their flexibility and controllability.

Most Thyristor Controlled Series Compensator (TCSC) applications utilizes Sub-Synchronous Damping Controllers (SSDCs) to avoid SSR. The TCSC inherently provides some level of damping in the sub-synchronous frequency range even without SSDCs. Even-though there have been studies on the use of TCSCs to avoid SSOs, the mechanism behind the inherent damping capability of the TCSC is not well established. Furthermore, there remains uncertainty regarding the extent to which the inherent damping capability can be relied upon to mitigate SSOs and the need for supplementary damping controllers.

This thesis investigates the role of TCSCs in damping SSOs in power systems, mainly considering its inherent damping nature, while accommodating SSDCs when required. To accomplish this task, a simplified Dynamic Phasor (DP) small signal model of the TCSC is proposed for SSO studies, which accurately represent its inherent damping capability in the sub-synchronous frequency range. The adequacy of the proposed small signal model for SSR analysis is assessed upon validation against EMT simulations. The proposed model is used to evaluate the inherent damping capability of the TCSC for Induction Generator Effect (IGE) and Torsional Interactions

(TIs) in conventional power systems as well as Wind-Sub-Synchronous Controller Interactions (W-SSCIs) in systems with Type 3 Wind Power Plants, through DP based small signal stability analysis.

The study reveals that proper selection of TCSC parameters improves its inherent damping capability. The network resonance is eliminated when the TCSC is operated close to its highly non-linear range (without SSDCs). It is shown that the inherent damping capability of the TCSC is adequate to avoid IGE and W-SSCIs even at low levels of TCSCs. However, to mitigate TIs in Conventional Turbine Generator (CTG) systems with low mechanical damping, high levels of TCSCs and operation near highly non-linear region are necessary. Consequently, the utilization of SSDCs becomes imperative to ensure effective TI mitigation.

In networks with multiple series compensated lines and CTGs, there can be many network resonances which can excite IGE and TIs with nearby generators. This thesis proposes a study procedure to replace critical FSCs with TCSCs to address existing SSO problems in such networks. The procedure starts with screening using frequency scans to identify critical FSCs, followed by a detailed analysis through DP based small signal stability analysis and Electromagnetic Transient Simulation(EMT) to determine TCSC parameters and design of SSDCs where necessary.

The outcomes of this research would serve as a guide for understanding and addressing SSO issues in power systems. Analytical methods proposed in this thesis would be useful to determine the applicability of TCSCs to mitigate SSOs.

# Use of Copyrighted Material

I would like to acknowledge the use of content from the following publications in this thesis, with approval from the authors and in compliance with copyright provisions. Only the content from publications where I am the first author is included in this thesis.

1. **D. R. Weerakoon**, C. Karawita, and U. D. Annakkage, "Evaluation of Inherent Damping Introduced by Thyristor Controlled Series Compensators," in *IEEE Open Access Journal of Power and Energy*, 2023. Available at `https://ieeexplore.ieee.org/stamp/stamp.jsp?tp=&arnumber=10049433`

2. **D. R. Weerakoon**, U. D. Annakkage, and C. Karawita, "A Review on Sub-Synchronous Resonance Damping with Thyristor Controlled Series Compensators," in *Journal of Advances in Engineering and Technology*, 2023. Available at `https://rda.sliit.lk/handle/123456789/3370`

3. **D. R. Weerakoon**, U. D. Annakkage, and C. Karawita, "Analysis of Sub Synchronous Resonant Modes in Series Compensated Networks Using Multiple Frequency Scans," in *2020 CIGRE Canada* Conference in Toronto. Available at `https://www.e-cigre.org/publications/detail/coll-tor-2020-colloquium-toronto-2020.html`

# Acronyms

| | |
|---|---|
| CTG | Conventional Turbine Generator |
| DDSO | Device Dependant Sub-synchronous Oscillation |
| DFIG | Doubly Fed Induction Generator |
| DP | Dynamic Phasor |
| DTA | Damping Torque Analysis |
| EM | Electro-Mechanical |
| EMT | Electro Magnetic Transient |
| FACTS | Flexible AC Transmission System |
| FSC | Fixed Series Compensator |
| GSC | Grid Side Converter |
| HVDC | High Voltage DC Converter |
| IGE | Induction Generator Effect |
| PED | Power Electronic Device |
| PLL | Phase Locked Loop |
| POC | Point Of Coupling |
| PSS | Power System Stabilizer |
| RF | Radiality Factor |
| RSC | Rotor Side Converter |
| SSDC | Sub Synchronous Damping Controller |
| SSO | Sub Synchronous Oscillation |
| SSR | Sub-Synchronous Resonance |
| SSTI | Sub-Synchronous Torsional Interaction |
| SVR | Synchronous Voltage Reversal |
| TCSC | Thyristor Controlled Series Compensator |
| TA | Torque Amplification |
| TCR | Thyristor Controlled Reactor |
| TI | Torsional Interaction |
| TM | Torsional Mode |
| UIF | Unit Interaction Factor |
| WPP | Wind Power Plant |
| W-SSCI | Wind Sub Synchronous Controller Interaction |

# Table of Contents

# List of Figures

# List of Tables

# Chapter 1

# Introduction

Series compensation of transmission lines has been used to facilitate long distance ac power transmission. It is known to improve the power transfer capability and enhance the transient stability limits of the power system [1]. Previously, utilities predominantly utilized series capacitors, also known as Fixed Series Compensators (FSCs), for series compensation due to their simplicity and cost-effectiveness. However, presence of FSCs in the network may cause adverse interactions with other power system devices such as Conventional Turbine Generators (CTGs) and power electronic converters [1]- [2] leading to growing Sub-Synchronous Oscillations (SSOs). SSOs are oscillations in the power network at frequencies below the nominal frequency of the system (typically below 50/60 Hz), excluding Electro-Mechanical (EM) oscillations.

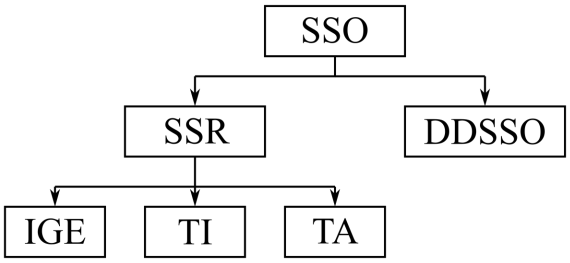


Figure 1.1: Classification of SSO - IEEE - 1992

## 1.1 Incidents and Classification of SSOs

Problems associated with application of series capacitors were initially discussed in 1937 [3]. It was discussed that under certain conditions, synchronous machines in series compensated networks may behave as induction machines, amplifying sub-synchronous currents. Subsequently, this phenomenon came to be known as the Induction Generator Effect (IGE). SSOs have been extensively studied since the first two consecutive incidents occurred at Mohave generating station in Southern Nevada in 1970 and 71 [4]. The incident was due to Torsional Interactions (TIs) and resulted in severe damage to the turbine generator shaft system. The main cause for TIs was identified as the FSCs in transmission lines [5].

SSOs extend beyond series compensated networks and CTGs. In 1977, it was found that High Voltage DC (HVDC)converters also can interact with CTGs at sub-synchronous frequencies even in the absence of series compensation [6]. Furthermore, devices such as HVDC converters [7], Power System Stabilizers (PSSs), Static Var Compensators (SVCs) [8], high-speed governor controls [9] and variable-speed drive controls may interact with nearby CTGs. Consequently, the term Device Dependant Sub-Synchronous Oscillations (DDSSOs) was introduced by IEEE working group to characterize the emerging category of interactions between CTGs and fast acting

controls. [10–12].

In 1992, the IEEE working group proposed standard definitions and classifications for SSOs, as illustrated in the classification shown in Fig. 1.1. The classification identifies two main categorizes, namely: (1) Sub-Synchornous Resonance (SSR) and (2) DDSO. SSR is further classified into IGE, TIs and Torque Amplification (TA). SSR is defined in [13] as a condition that arises when the turbine generator and electric network exchange energy at one or more natural frequencies of the combined system below the synchronous frequency of the system. TIs are interactions between the mechanical system of the generator against the network and occur when the network resonant frequency is close to any of the torsional modes of the turbine generator shaft system. This can lead to sustained or growing torsional oscillations if the combined electrical and mechanical damping is insufficient. TA occurs following large disturbances, while other types of SSOs may arise from small disturbances. If the network resonant frequency is close to the torsional frequencies of the turbine generator shaft, large swings in shaft torques can occur following large disturbances.

The integration of renewable generation and power electronic devices into the network has led to the emergence of different types of SSOs in the modern power system. Apart from SSR incidents involving CTGs, a new phenomenon named Sub-Synchronous Controller Interactions (SSCIs) was introduced after an incident in 2009, where interactions between a Type-3 Wind Power Plant (WPP) (Doubly-Fed Induction Generators (DFIGs)) and a series compensated transmission line was reported [2]. Since then, many studies on SSOs associated with WPPs are reported in literature [14–16]. An incident of SSOs linked to a Type-4 WPP was reported in China in 2015 [17].

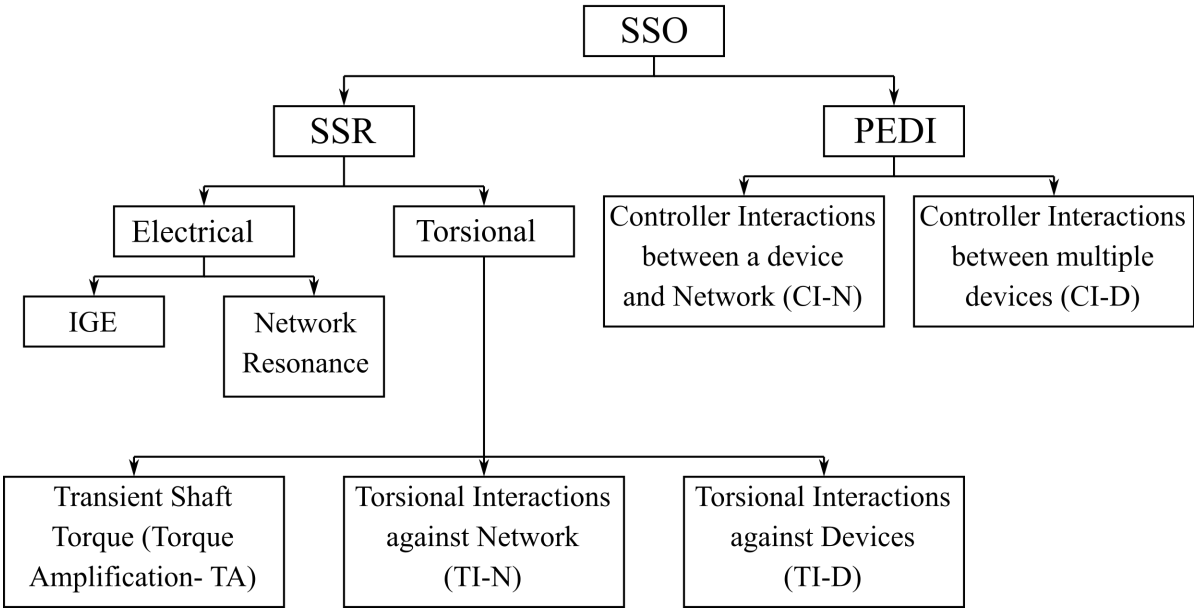


Figure 1.2: Classification of SSO - CIGRE - 2023

In response to the evolving dynamic characteristics of the power system, IEEE has re-visited and expanded the classification of previously defined stability terms to incorporate the response of fast-acting power electronic devices [18]. This has resulted in two new categories, namely: (1) Resonance stability and, (2) Converter-driven stability.

- **Resonance stability**: Includes SSR , whether it is torsional or purely an electrical resonance, and DDSSO. Resonance stability is further divided into (1) Torsional resonance and (2) Electrical resonance. In contrast to IEEE's previous classification, this category encompasses SSCIs occurring in DFIG systems connected to series compensated networks under the sub-category "Electrical resonance".

- **Converter-driven stability**: Includes stability issues associated with control systems of power electronic based systems and various components of the power

system such as the transmission network, generator stator dynamics and other power electronic devices over a wide range of frequencies. While this category is expansive, encompassing phenomena like harmonic instabilities, it also includes stability issues related to sub-synchronous frequency oscillations.

Given the diverse nature of interactions observed in various SSO phenomena, a new classification has been proposed in the CIGRE TB 909 [19]. This classification categorizes SSOs into two main groups, namely: (1) SSR, and (2) Power Electronic Device Interactions (PEDIs), which are further divided into sub-categories as shown in Fig 1.2. The SSR category of this classification is consistent with the "Resonance stability" category of the latest IEEE stability classification. The PEDI category includes a SSO related converter-driven stability issues and it further classifies interactions into, (1) interactions between power electronic devices against the network (CI-N) and (2) interaction between two power electronic devices across the network (CI-D).

## 1.2 Sub-Synchronous Resonance

An FSC is a major network component which significantly influences SSR except for TI-D (Torsional Interactions against Devices). Following a disturbance, transient currents flowing in a series compensated network are different from an uncompensated network. To explain this further, consider a simple RLC circuit shown in Fig.1.3. The circuit is supplied with a sinusoidal ac source of magnitude '$V_s$', angular frequency '$\omega_s$' and a phase angle of '$\alpha$' as in (1.1).

$$V = V_m \sin(\omega_s t + \alpha) \tag{1.1}$$

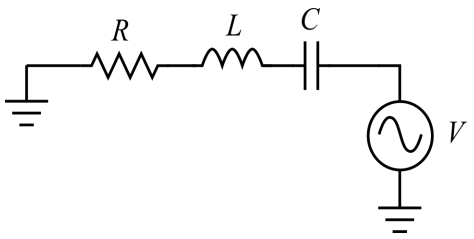


Figure 1.3: RLC crcuit

The current in the circuit without the capacitor 'C' can be expressed in Laplace domain as follows.

$$I_{(s)} = \frac{V_{(s)}}{Z_{(s)}} = \frac{\frac{V_{(s)}}{L}}{s + \frac{R}{L}} \tag{1.2}$$

where '$V_{(s)}$' is the laplace transform of the input voltage expressed as,

$$V_{(s)} = V_m \frac{s\sin(\alpha) + \omega_s \cos(\alpha)}{s^2 + \omega_s^2}$$

The current flowing through the circuit without the series capacitor can be expressed in time-domain as in (1.3).

$$I_{(t)} = A\sin(\omega_s t + \alpha - \phi) - A\exp^{-\frac{1}{\tau}t}\sin(\alpha - \phi) \tag{1.3}$$

The current contains a sinusoidal steady state component and a DC transient component decaying at a time constant of '$\tau$'. There are no other sinusoidal components of any other frequencies. However, when the series capacitor is present in the circuit, the current takes a different form as in (1.4).

$$I_{(s)} = \frac{V_{(s)}}{Z_{(s)}} = \frac{\frac{sV_{(s)}}{L}}{s^2 + s\frac{R}{L} + \frac{1}{LC}} \tag{1.4}$$

The denominator in the above equation takes the form of a second order equation and can be expressed as in (1.5).

$$I_{(s)} = \frac{V_{(s)}}{Z_{(s)}} = \frac{\frac{sV_{(s)}}{L}}{s^2 + 2\zeta\omega_n s + \omega_n^2} \tag{1.5}$$

where,

$$w_n = \text{Un-damped natural frequency} = \sqrt{\frac{1}{LC}}$$

$$\zeta = \text{Damping ratio} = \frac{R}{2}\sqrt{\frac{C}{L}}$$

The current flowing through the circuit with the series capacitor can be expressed in time-domain as in (1.6).

$$I_{(t)} = A_1 \sin(\omega_s t + \psi_1) + B \exp^{-\zeta\omega_d t} \sin(\omega_d t + \psi_2) \tag{1.6}$$

where,

$$w_d = \text{Damped natural frequency} = \omega_n\sqrt{1-\zeta^2} = \frac{1}{2L}\sqrt{\frac{4L - R^2C}{C}}$$

Current in (1.6) has two sinusoidal components unlike in an uncompensated system. One sinusoidal component is at the supply frequency ($w_s = 50/60\ Hz$) and the other sinusoidal component is at frequency '$w_d$', which is the damped natural frequency of the system. This frequency entirely depends on the network elements. Other parameters in (1.6) such as '$A_1, B, \psi_1\psi_2$' are functions of network elements.

According to Park's transformation, currents of frequency '$\omega_s$' will be reflected to the rotor as DC currents in steady state (when the frequency of transformation is '$\omega_s$'), whereas currents of frequency '$\omega_d$' will appear as currents of frequency '$\omega_s + \omega_d$' and '$\omega_s - \omega_d$'. The currents at super-synchronous frequencies typically may not affect the CTGs because they are generally well-damped at frequencies higher than the synchronous frequency ($w_s$), and the shaft's oscillatory modes are usually below the synchronous frequency. Therefore, it is the sub-synchronous current components that raise major concerns.

The resistance of transmission lines is relatively small compared to their inductive impedance. Hence, it is reasonable to assume that the damped natural frequency

is approximately equal to the un-damped natural frequency $\omega_d = \omega_n$. The level of series compensation is always chosen to be less than the inductive impedance of the line. Hence, the natural frequency '$f_n$' expressed in (1.7) is always less than the synchronous frequency $f_s$.

$$f_n = f_s\sqrt{\frac{X_C}{X_L}} \tag{1.7}$$

$$f_n <= f_s$$

In systems with CTGs, following interactions can occur between the network and the CTGs due to sub-synchronous effects.

1. Induction Generator Effect (IGE)
2. Torsional Interactions (TIs)
3. Torque Amplification (TA)

In networks with Type-3 WPP, Wind Sub-Synchronous Controller Interactions (W-SSCIs) may occur due to the sub-synchronous effects.

### 1.2.1 Induction Generator Effect

Sub-synchronous frequency currents of '$\omega_n$' reflected on the rotor side will produce a rotating Magneto Motive Force (MMF) of the same frequency. This MMF rotates slower than the rotor magnetic field rotating at '$w_s$'. Consequently, the machine behaves like an induction machine to sub-synchronous currents and can be represented as shown in Fig. 1.4. This is due to the resistance of the generator rotor as seen from

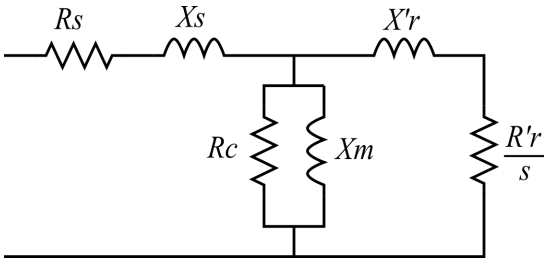


Figure 1.4: Induction machine equivalent circuit

the armature appears negative due to the negative slip ($s$) as calculated in (1.8).

$$s = \frac{\omega_n - \omega_s}{\omega_n} < 0 \tag{1.8}$$

If the combined resistance of the generator and the network at sub-sycnrhonous frequencies becomes zero or negative, there will be sustained or growing sub-synchronous currents. At high levels of series compensation, the effective negative rotor resistance can exceed the network resistance and this phenomena is known as the IGE [1]. Super-synchronous currents does not pose any threat to system stability since the induction motor effect absorbs energy from the disturbance, unlike IGE, which injects more energy into the disturbance.

### 1.2.2 Torsional Interactions

The rotors of CTG systems, such as those in steam turbine generators, comprise of multiple mechanical masses linked by shafts of finite stiffness. Therefore, disturbances to the CTG can induce torsional oscillations between various sections of the turbine generator rotor. Sub-synchronous currents entering the generator will produce oscillatory shaft torques at sub-synchronous frequency '$\omega_s - \omega_n$'. Typically the

natural frequencies of the turbine generator mass system lies in the sub-synchronous frequency range. When the frequency of the induced sub-synchronous torque is close to one of the torsional modes of the turbine-generator shaft system, oscillations in the generator rotor will build up. Voltages induced by these rotor oscillations will lead to significant sub-synchronous currents, which are in phase to sustain the sub-synchronous torque. If the enhanced sub-synchronous torque exceeds the torque generated by the mechanical damping of the rotating system, the system will undergo growing torsional oscillations. This phenomenon known as "Torsional interactions", in particular, "Torsional Interactions against Network (TI-N)", and can have severe consequences, potentially resulting in shaft damage [1, 4].

### 1.2.3 Wind Sub-Synchronous Controller Interactions

The phenomenon, SSCIs emerged after an incident in south Texas in 2009, where interactions between a Type-3 WPP (DFIG) and a transmission line with FSCs was reported [2]. Interactions between DFIGs and series compensated lines occur at the network resonant frequency and can become unstable due to the negative damping presented by the WPP control system. In [20], it is shown that WPP controllers do not participate in the network mode, but the mode is sensitive to controller parameters. Hence this phenomenon is characterised as an electrical resonance that is sensitive to controller gains in [20] and later termed as Wind-SSCIs in [19]. This phenomenon does not involve any mechanical interactions and primarily arises due to the negative resistance presented by the WPP control system towards the grid during sub-synchronous oscillations, leading to self excitation of the machine.

### 1.2.4 Torque Amplification

During large disturbances such as short-circuit faults, transient torques of the CTGs will be amplified above the stress level that would result without the series compensation. The magnitude of shaft torques can escalate further if the sub-synchronous resonant frequencies of the network are close to the shaft torsional frequencies. This phenomenon, recognized as "Torque Amplification," or alternately as "Transient Shaft Torques," can occur in series compensated systems even when TIs are sufficiently damped.

## 1.3 Analytical Techniques

Various analytical methods for SSOs have been developed with the emergence of different types of SSOs. Due to the diverse nature of SSOs, certain tools are only applicable to specific types of SSO identification. Broadly, these analytical techniques can be categorized under two groups: (1) Screening, and (2) Detailed analysis.

### 1.3.1 Screening of SSOs

SSO screening is the first step in the study process and the available tools are rather simple and easy to use. SSO screening can be conducted to assess the risk at an initial planning phase (e.g., before commissioning a power plant) or to analyse existing SSO issues. In large power systems, conducting detailed analysis for large number of operating conditions and contingencies is not practical. For certain detailed analysis such as small-signal stability analysis, it is not feasible to create detailed models of large networks with numerous dynamic devices. In such situa-

tions, screening tools help to identify and narrow down potential risks across various cases, including multiple operating conditions, contingencies, or areas of the power system requiring detailed examination. SSO screening tools are not meant to identify the root cause for SSOs and the contributing devices to SSOs, but aim to narrow down the study for detailed analysis without classifying potential risk conditions as safe . Essentially, screening studies may produce false alarms but should avoid false dismissals [19]. Results from screening techniques should not be used to draw conclusions regarding the definite risk of SSO. Some of the popular screening techniques available are listed below.

1. Frequency Scanning
2. Unit Interaction Factor (UIF)
3. Radiality Factor (RF)

**Frequency Scanning**

Frequency scanning is the process of obtaining the impedance characteristics of the system over a frequency range of interest. Impedance characteristics of a system can be obtained analytically as well as through simulations. Analytical frequency scans, also known as passive frequency scans, are typically more suitable for scanning the network. The equivalent impedance of the network at a specific bus (Point Of Connection-POC) looking into the network is calculated over the frequency range of interest. The impedance of the device under study is disregarded when obtaining the network frequency scans. Network frequency scans will indicate series and parallel resonances in the vicinity of the scanned location. A sample passive frequency scan

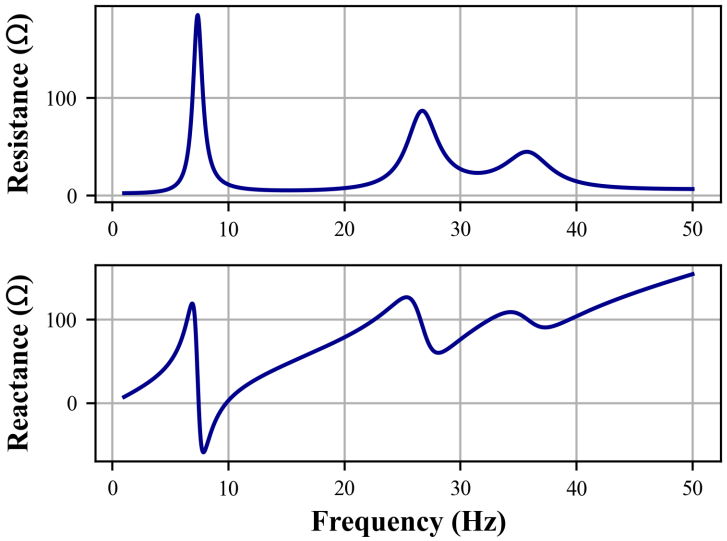


Figure 1.5: Example frequency scan of a series compensated network

of a series compensated transmission system, within the sub-synchronous frequency range, at a bus where a CTG is connected is shown in Fig. 1.5. It indicates a series resonance at approximately 10 Hz and two other distant resonances around 27 Hz and 36 Hz. Thus, there exist a risk of SSR mainly around the 10 Hz series resonance and potentially at the other two distant resonances. The distant resonances are occurring due to FSCs installed farther away to the device.

Impedance characteristics of a dynamic device (CTG or a Power Electronic Device(PED)), is recommended to be obtained through dynamic frequency scans, in order to capture dynamic characteristics accurately. Dynamic frequency scanning allows to extract the linearized impedance characteristics of the device numerically by injecting small amplitude signals to the device. This is a simulation-based approach which obtains the transfer function between the injected current/voltage input and measured voltage/current output of a system (impedance or admittance model). Hence, a wide range of details can be represented in the model. A sample

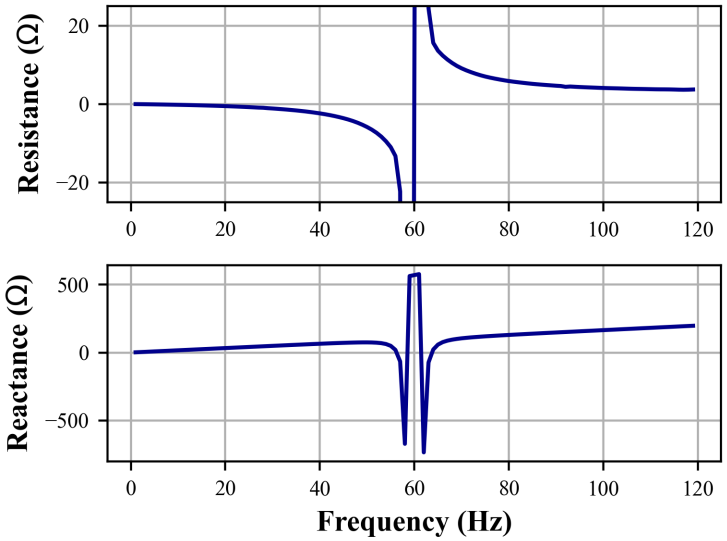


Figure 1.6: Example frequency scan of a synchronous generator

dynamic frequency scan of a synchronous generator is shown in Fig. 1.6. It clearly indicates that the resistance of the generator seen from its terminal is negative in the sub-synchronous frequency range which may cause self excitation problems.

The impedance characteristics of both the network and the device under study can be added together to determine the total impedance within the sub-synchronous frequency range. The combined frequency scans can be used to identify low-damped network resonances that require detailed analysis.

While frequency scanning is not limited for SSR analysis, it has been widely used for studying PED-Grid interactions, PED-PED interactions and harmonics interactions. While the series addition of frequency scan results of the device and the network is adequate to identify risks of SSR, the device and network can also be treated as a source and a load and obtain the closed loop transfer function of the system. The stability of the closed loop system can be evaluated with Nyquist stability criterion or bode plots [19]. The sample frequency scans illustrated above are obtained with

positive sequence components, and the SSR risk analysis can be conducted in the sequence domain. However, frequency scanning and analysis can extend to domains like DQ variables and Dynamic Phasor (DP) variables [19].

### Unit Interaction Factor

Unit Interaction Factor (UIF) is an index used to screen for potential risk of torsional interactions between CTGs and HVDC systems [19, 21]. UIF is determined based on the impedances between the HVDC and the CTG under study and their MVA ratings. These impedances reflect the contribution of the CTG to the short circuit capacity at the HVDC terminal bus, indicating the severity of adverse effect of an HVDC system to TIs of a CTG. If the calculated UIF is greater than a certain threshold (0.1 for LCC HVDC converters and CTGs), the case may be classified having Sub-Synchronous Torsional interaction (SSTI) risk. This method is valid for inductive networks, where the impedance of the network changes linearly in the sub-synchronous frequency range and cannot be used to quantify SSTI risk in networks with series compensated lines [19].

### Radiality Factor

Radiality Factor (RF) is an index derived from network impedance which reflects the radialness of the network between a device (HVDC or any other dynamic device) and a CTG under study [22]. It essentially quantifies the electrical proximity between the CTG and the PED which affects TI-D. This approach is applicable to series compensated networks as it calculates the RF for the whole sub-synchronous frequency range. If, for any generator, the RF exceeds the predefined threshold of 0.2 [22] at any

sub-synchronous frequency, the generator may be considered for detailed analysis.

### 1.3.2 Detailed Analytical Techniques

Typically detailed analytical techniques needs detail representation of power system components than with screening techniques. Two main detail analytical techniques applicable for SSO studies are listed below.

1. Small-Signal Stability Analysis
2. Electro-Magnetic Transient (EMT) Simulations
    - Damping Torque Analysis (DTA)

#### Small-Signal Stability

Small-signal stability analysis provides insights into the frequency domain characteristics of the system. It involves representing the system as a linear set of differential equations and analyzing stability using Lyapunov's first stability criterion [23]. The eigenvalues of the linearized state space model reveal the frequency and damping of oscillatory modes in the system. Furthermore, eigenproperties of the state matrix can be used to calculate participation factors, mode shapes, observability and controllability, which provides insights into the root cause of the oscillation and means to influence and control them. Thus, small-signal stability analysis helps to identify the underlying reasons for SSOs and develop appropriate control techniques to mitigate SSOs [1, 20, 24]. Linearization of the system around a specific operating point limits the analysis to small disturbances and therefore large disturbance phenomena such as TA cannot be analysed with this technique.

### Electro-Magnetic Transient Simulation

Electromagnetic transient simulation is a time-domain technique that involves numerical integration of the differential equations, while taking into account the non-linear effects. It is the closest approximation that exist to the real-world system and has been widely used for the analysis of SSOs. This approach is particularly effective for investigating large disturbance phenomena such as TA. However, identifying the root cause for SSOs and the devices participating can be challenging in time-domain analysis.

### Damping Torque Analysis

Damping Torque Analysis (DTA) is a frequency-domain analytical technique which can be used to assess the torsional mode stability of a CTG [25]-[26]. Also referred to as the complex torque coefficient, DTA evaluates the electrical damping torque coefficient across a range of frequencies. The electrical and the mechanical system of a CTG system can be represented in a block diagram as in Fig. 1.7. When the rotor is subjected to small oscillations, a synchronous machine develops an additional electric torque $\Delta T_E$. The damping torque co-efficient is the electrical torque component which is in phase with the rotor speed deviations. It can be computed by applying small sinusoidal perturbations to the generator speed reference in EMT simulations and measuring the corresponding electrical torque deviation which is in phase with the measured speed. The system is considered stable if the net damping (combined mechanical and electrical damping) at any torsional mode frequency is positive. Typically mechanical damping of turbine generator masses are very low and negligible.

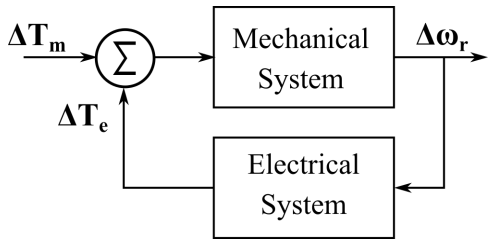


Figure 1.7: Combination of electrical and mechanical system

## 1.4 SSO Mitigation Techniques

Implementing mitigation measures for SSOs is crucial during the planning phase or during operation to prevent physical damage to equipment or potential system collapse. Various mitigation techniques are documented in the literature and are actively deployed in practical power systems [27].

### FSC Bypassing Relays

A traditional and a temporary solution to protect the power system components against SSR caused due to FSCs is to bypass some or all series capacitors using a relay-controlled circuit breaker. By bypassing the FSC, the network resonance is shifted away from the torsional oscillation frequencies of the CTG. However, this approach reduces the power transfer capability of the transmission line, which contradicts the initial purpose of FSC installation.

### Static Filters

Static SSR filters are designed to mitigate SSR by either shifting the electrical resonant frequencies away from the torsional frequencies of the CTG or by adding positive resistance at torsional frequencies. These filters can be installed either at the CTGs or at FSC locations. However, these filters must be precisely tuned to block

currents of specific sub-synchronous frequencies. Filters may become less effective if SSR conditions such as frequencies of oscillations change.

1. **SSR blocking filters** installed at the generator are effective in mitigating TIs and TA. They are typically installed in series with the generator step-up transformer, either on the neutral end or high-voltage side of the transformer winding [27, 28]. These filters consist of high Q-factor parallel resonant circuits tuned to block currents at frequencies corresponding to each of the torsional frequencies. The first installation of such filters was carried out at the Navajo Generating Station in 1976 [29]. High Q factor filters are highly sensitive to component variations which can make it less effective over time.

2. **Bypass damping filters** consist of a resistor in series with a parallel LC combination. It can be installed at FSC locations, connected in parallel with some or all of the FSCs. These filters exhibit very high impedance at the system frequency. However, at sub-synchronous frequencies, they allow sub-synchronous currents to pass through, thereby adding positive resistance to the system at sub-synchronous frequencies. They are highly effective in preventing IGE and SSCI issues [27, 28]. However, these filters may become less effective if the SSR frequencies change due to changes in system conditions.

### Dynamic Filters

A Dynamic Filter is an active device installed in series with a generator. It generates a voltage that opposes the sub-synchronous voltages induced in the armature due to rotor oscillations. The magnitude of the generated voltage must be sufficient to

compensate or exceed the sub-synchronous voltage. These filters can also offer much higher net damping than what the mechanical system alone provides and therefore is effective in TI mitigation [30, 31].

### Supplementary Excitation Damping Controllers

Supplementary Excitation Damping Controllers (SEDC) can be used increase the damping of CTG torsional oscillations. This control system operates in conjunction with the existing excitation controller, modulating the field voltage at torsional frequencies to introduce damping effects. It uses the speed of the torsional mode as the input and with proper phase shifting and amplification, damping is added to torsional oscillations [30].

### Controller adjustments

In certain SSO phenomena, such as W-SSCIs, controller adjustments can be made to mitigate SSOs. In [20], it is shown that the damping of the network resonance in a serves compensated system with Type-3 WPPs is sensitive to the Rotor Side Converter (RSC) inner current controller gains and outer loop reactive power controller gain. The damping of the network resonance can be improved by reducing these gains of the RSC converter controller.

### NGH Scheme

NGH scheme was invented by Dr. N.G. Hingorani and the scheme uses a thyristor controlled resistor connected across the FSC [32] to damp SSR. This scheme continually monitors the voltage across the series capacitor and if sub-synchronous currents

are detected, the control mechanism triggers the thyristors, which discharges the sub-synchronous energy through the resistor. Under normal operating conditions, where no SSR is present, thyristors are not active, and the resistor has no impact on the system.

### Thyristor Controlled Series Compensators

Thyristor Controlled Series Compensator (TCSC) is a Flexible AC Transmission System (FACTS) device which allows rapid and continuous control of series compensation level of transmission lines and hence provides flexible power transfer capability. It can be effectively utilized to damp power system oscillations and mitigate SSR [33]. Many studies have been conducted on damping SSR with TCSCs via active control schemes such as Sub-Synchronous Damping Controllers (SSDCs) [34–37]. Such techniques modulate the firing angle to introduce damping. However, when the TCSC is operating as a capacitor, its inherent behaviour in the sub-synchronous frequency range is useful in mitigating SSR in some cases as shown by [38–40]. However, the adequacy of inherent damping capability to mitigate different types of SSOs and the need for SSDCs needs further investigation.

Apart from above techniques, a discrete control strategy based on phase unbalanced concept is used in [41]. The basic concept is to have three different inductor-capacitor combinations in each phase so that they produce equal reactances at the power frequency and unequal reactances at the other frequencies, preventing balanced sub-synchronous currents entering the generator during transients and producing a pure rotating MMF.

## 1.5 Previous Studies on Application of TCSCs for SSO Damping

Based on the reported literature on damping SSOs with TCSCs, TCSC contributes to solve SSR in different ways and can be generally categorized as follows.

1. Damping of SSOs with TCSCs via supplementary control schemes such as SSDCs.
2. Inherent behaviour of the TCSC in the sub-synchronous frequency range.

The first technique is mainly evaluated in practical projects. Primary control techniques such as constant current, constant power, and constant impedance controllers cannot mitigate SSR as they are not designed to do so, but can contribute towards SSR damping [39]. Supplementary controls such SSDCs modulate the firing angle of the TCSC to introduce damping. It uses remote signals such as generator speed deviation [34–36] or local measurements such as currents [37] to detect SSR and modulate the firing angle to produce an additional electrical damping torque.

While SSDCs secure SSR mitigation as it is only designed for that purpose, the inherent nature of the TCSC itself, without any supplementary control techniques posses some capability in avoiding SSR conditions [38–40, 42, 43]. Simulator tests on the first TCSC installation at Kayenta substation in 1990 [42] shows that the TCSC impedance in open loop configuration exhibits a resistive-inductive nature for sub-synchronous frequencies, providing positive damping to SSR conditions.

A study on the second TCSC installation at BPA's (Bonneville Power Administration) Slaat substation in 1995 [40, 43] has showed that the TCSC operating

in impedance control mode makes the electrical system behave like an uncompensated system in terms of the electrical damping torque observed at the synchronous machine. The frequency response of one of the segments of TCSCs at Slaat [38] shows that the electrical resonant condition is avoided through TCSC by changing its capacitive reactance at sub-synchronous frequencies and introducing an equivalent resistance.

Work in [44] has shown that the TCSC behaves as a positive resistance in series with a small inductance at sub-synchronous frequencies. Work in [45] shows that a virtual resistance appears in the TCSC due to the switching action. It has also shown that apart from the positive resistance at sub-synchronous frequencies, TCSC also exhibits a slight negative resistance at the synchronous frequency. This resistive performance at synchronous and sub-synchronous frequencies is explained in terms of the power conversion ability in [46].

Some of the real world TCSC projects are installed for the sole purpose of avoiding existing SSR in the power system. A TCSC was installed in the Swedish transmission system to replace 30% of the Stode FSC to improve SSR conditions between a FSC and turbine generator masses of a nuclear power plant [47]. The Stode TCSC uses a special thyristor control technique called Synchronous Voltage Reversal (SVR) [48] to fire the thyristors by synchronizing the voltage zero crossing points under impacts of SSR. This technique has also been applied to a TCSC installed in Korean power network [49] and was able to avoid SSR risk. This method exhibits inherent damping to SSR conditions, however its effectiveness in SSR mitigation is limited within lower TCSC boost factors. Furthermore, patents related to SVR control technique could restrict the number of suppliers capable of delivering the required performance.

## 1.6 Existing TCSC Models in Literature

TCSC is a non-linear device which involves both continuous and discrete events. The non-linearity can be handled well with EMT models and compared to other simulation models, they give the closest prediction of the performance to the real device. Quasi-steady state models of TCSCs are not suitable for SSR analysis as it omits important dynamics of TCSC such as the inductor current dynamics, in sub-synchronous frequency range. Modelling techniques reported in literature which are suitable for SSR, can generally be categorized as, (a) discrete time modelling, (b) DP modelling, and (c) numerical modelling with frequency scanning.

Discrete time models of TCSC have been developed based on the theory of Poincare mapping in [50–56]. The small-signal stability is assessed based on the eigenvalues of the Jacobian of the Poincare map. Discrete models developed in [50–52] lacks modularity, where the rest of the power system has to be also discretized. However, [53, 54] has converted the discrete time model to a continuous model based on the assumption that the interfacing quantities of the TCSC with the network is constant over a half cycle period. But, as stated by authors of [54], the validity of modelling approach is questionable if the TCSC accounts for a large portion of the total compensation level. However, the inherent damping associated with open loop operation of the TCSC is accurately represented by these discrete models. Previously discussed models are based on two samples per cycle, limiting the bandwidth to 120 Hz. Model derived in [55] has increased the bandwidth by accommodating six samples per cycle. However, the model is sample variant and not modular. The modularity of six samples per cycle model is achieved in [56] by assuming linear variation of interface variables in contrast to assuming them constant as in [53, 54].

Work in [35] uses frequency scanning to numerically obtain small-signal frequency response of the system through time-domain simulations. Then the frequency response matrix of the TCSC is fitted to a rational transfer function using vector fitting technique which is then converted to state-space form and combined with the state space model of the rest of the system. While this method is accurate for analysing the stability, it lacks information about the physical states and the results depends on the measurement parameters such as filter constants. Furthermore, it may result in unexplainable eigenvalues when trying to fit the frequency response, specially for large power systems.

The concept of time varying Fourier coefficients has been first applied to TCSCs in [57] and a simplified version of it has been used to analyse the SSR behaviour in [58]. DP modelling of TCSC leads to simple yet powerful models, which are modular in nature and computationally efficient. These models are compatible with phasor based representation of other power system components and therefore can easily be implemented in commercial dynamic phasor based small-signal stability assessment tools. The large signal DP model in [57] has been extended to include the dynamics of higher-order harmonic terms of the TCSC in [59]. However, the work does not investigate the small-signal stability of the model.

## 1.7 Motivation

Due to growing number of SSO issues in the power electronic dominated power system, industries have the incentive to make significant investments on TCSCs instead of FSCs. While utilizing SSDCs on TCSCs ensures SSR mitigation, the extent

to which the inherent damping capability of the TCSC can prevent SSO conditions remains uncertain. Further investigation is needed to determine the extent to which the inherent damping capability can be relied upon to mitigate SSOs and whether supplementary damping controllers are necessary. Thus it is worth investigating and understanding the source of inherent damping of the TCSC at sub-synchronous frequencies so that the inherent nature of the TCSC can be utilized to avoid existing SSR problems.

Use of discrete time models for small-signal stability analysis of TCSCs is well established in literature. However, in general, the model derivation in quiet complex and is not compatible with phasor based models of other power system components unless otherwise they are converted to the phasor domain. Therefore, it is intended to investigate the applicability of using DP models of TCSC for small-signal stability analysis. The DP model should be capable of capturing the important dynamics of the TCSC which affects the inherent damping nature at sub-synchronous frequencies.

In networks with multiple FSCs, there can be many sub-synchronous oscillatory modes which can excite IGE or torsional modes of nearby CTGs. Replacing all FSCs with TCSCs may not be a viable solution for utilities due to the cost associated with TCSCs. A better option would be to replace a few and/or a portion of an FSC with TCSCs. Identifying the location/s and the level of compensation from TCSC, to mitigate the potential SSR conditions is a challenging task and it is intended to be addressed by this research. It is also important to identify situations where the inherent damping capability itself is insufficient to damp SSR and the use of active damping techniques in such situations.

## 1.8 Thesis Objectives

The objectives of this thesis are as follows:

1. Develop a continuous-time small-signal model for TCSC that is suitable for SSO studies and accurately represents the inherent damping characteristics of the TCSC at sub-synchronous frequencies.

2. Comprehensively evaluate the inherent SSO damping capability of the TCSC using the developed models.

3. Provide recommendations on the utilization of inherent SSO damping capability of the TCSC to avoid different SSO phenomena and the requirement of SSDCs.

4. Develop a procedure to utilize TCSCs in multiple series compensated networks to mitigate SSR.

Contributions of this work are as follows.

1. A simplified DP model of the TCSC, adopted from an existing higher order model, is proposed for small-signal stability assessment of SSR. This thesis identifies the requirement of various modelling details in an existing higher order DP model of the TCSC for accurate SSR studies. The simplified model accurately captures the inherent characteristics of the TCSC, important for damping SSR.

2. The adequacy of the inherent damping capability of the TCSC to mitigate different SSO phenomena was evaluated through small-signal stability assessment and recommendation are provided to achieve better SSR damping with TCSCs.

3. A methodology is developed to utilize multiple frequency scans to identify FSC(s) which contribute the most to the formation of a critical network resonances in multiple series compensated networks.

4. Two study procedures are proposed to determine appropriate locations for TCSCs to mitigate IGE (or W-SSCIs) and TIs in networks with multiple series compensated lines.

## 1.9 Thesis Outline

This research primarily focuses on investigating the role of TCSC in damping SSR, specifically in scenarios involving interactions with the network. As such, the scope of this study is confined to examining IGE, TIs against the network in CTG systems, and network resonances in wind integrated systems (specifically Type-3 WPP system with W-SSCIs).

Linearized models of the power system to study above mentioned phenomena is described in Chapter 2. The proposed simplified DP based small-signal model of the TCSC is introduced in this chapter. The mechanism within the TCSC which leads to the inherent damping and the representation of it in the model is explained.

Chapter 3 includes the validation of the linearized models described in Chapter 2. The DP based small-signal model of the TCSC is validated using a simple test system of voltage sources. The IEEE 1$^{st}$ Benchmark model for SSR studies is used to validate the SSR phenomena in CTG - series compensated networks, and the applicability of the DP based small-signal model of the TCSC for SSR studies is validated in the same test system. Furthermore, the test system used for W-SSCI studies is

presented and validated in this chapter. The small-signal models are validated against PSCAD/EMTDC software in time-domain considering small disturbances.

Evaluation of the inherent SSR damping capability of the TCSC is presented in Chapter 4 using the IEEE 1$^{st}$ Benchmark model for SSR studies. The effect of TCSC parameters on the inherent damping capability is assessed. The adequacy of the inherent damping capability of the TCSC in mitigating IGE, TIs and W-SSCIs is evaluated through small-signal stability analysis and recommendation are provided.

Chapter 5 proposes a comprehensive procedure to utilize TCSCs in multiple series compensated networks to mitigate IGE and TIs. Furthermore, a method of using frequency scans at multiple locations and under multiple contingencies to identify electrical resonances and the FSCs which contributes the most to them, is proposed. Design of SSDCs through eigenvalue analysis for mitigation of TIs is also presented.

Chapter 6 concludes the study, summarizing the findings, contributions, and offering recommendations for future research directions.

# Chapter 2

# Linearized Power System Models For SSR Analysis

As described in [1], *"Small-signal stability is the ability of the power system to maintain synchronism when subjected to small disturbances"*. The disturbance is considered to be "small" when the equations describing the system response, linearized around a certain operating point, yield reasonably accurate predictions. Thereafter, small-signal stability is assessed by applying Lyapunov's first stability criterion [23] to the linearized state space model of the power system.

System instability can arise due to two main factors: (1) lack of synchronizing torque, or (2) insufficient damping torque. Small-signal stability issues often arise due to the insufficient damping within the system. SSO phenomena such as, IGE, TI, and network resonances can be regarded as small-signal stability concerns since these oscillations sustain or amplify due to inadequate damping in the system. This allows the analysis of SSO phenomena using linearized models.

## 2.1 Linearization of Power System Components

The behaviour of the power system can be characterized by $n$ number of first order non-linear differential equations as in (2.1). The order of the system $n$ is the minimum number of dynamic variables required to describe the behaviour of the system. These system variables are known as states.

$$\dot{\mathbf{x}} = \mathbf{f}(\mathbf{x}, \mathbf{u}) \tag{2.1}$$

Where,

$$\mathbf{x} = [x_1, x_2, ..., x_n]^T \qquad \mathbf{u} = [u_1, u_2, ..., u_r]^T \qquad \mathbf{f} = [f_1, f_2, ..., f_n]^T$$

The column vector $\mathbf{x}$ contains the state variables of the system. The derivative of state variables is denoted by $\dot{\mathbf{x}}$. The vector $\mathbf{u}$ consists of $r$ external inputs to the system. The outputs of the system can be expressed in terms of state variables and inputs as in (2.2), where $\mathbf{y}$ is the output vector.

$$\mathbf{y} = \mathbf{g}(\mathbf{x}, \mathbf{u}) \tag{2.2}$$

Where,

$$\mathbf{y} = [y_1, y_2, ..., y_m]^T \qquad \mathbf{g} = [g_1, g_2, ..., g_m]^T$$

To study the small-signal stability of the above non-linear system, it needs to be linearized around an equilibrium point. The equilibrium point of the system, with $\mathbf{x_0}$ and $\mathbf{u_0}$ representing the initial state and input vector, respectively, for the operating point under study, satisfies (2.1) as,

$$\dot{\mathbf{x_0}} = \mathbf{f}(\mathbf{x_0}, \mathbf{u_0}) = 0 \tag{2.3}$$

Consider a small disturbance is applied to the system and the resulting state also satisfies (2.1) as (2.5).

$$\mathbf{x} = \mathbf{x_0} + \mathbf{\Delta x}, \quad \mathbf{u} = \mathbf{u_0} + \mathbf{\Delta u} \tag{2.4}$$

$$\dot{\mathbf{x}} = \dot{\mathbf{x_0}} + \mathbf{\Delta \dot{x}} = \mathbf{f}(\mathbf{x_0} + \mathbf{\Delta x}, \mathbf{u_0} + \mathbf{\Delta u}) \tag{2.5}$$

Equation (2.5) can be expanded using Taylor's series expansion. By neglecting the second and higher-order terms of $\Delta x$ and $\Delta u$, the derivative of the deviation of a state variable can be expressed as (2.6), where $i = 1, 2...n$.

$$\Delta \dot{x_i} = \frac{\partial f_i}{\partial x_1}\Delta x_1 + ... + \frac{\partial f_i}{\partial x_n}\Delta x_n + \frac{\partial f_i}{\partial u_1}\Delta u_1 + ... + \frac{\partial f_i}{\partial u_r}\Delta u_r \tag{2.6}$$

Similarly, the deviation in the output can be written as in (2.7), where $j = 1, 2...m$ (no of outputs).

$$\Delta y_j = \frac{\partial g_j}{\partial x_1}\Delta x_1 + ... + \frac{\partial g_j}{\partial x_n}\Delta x_n + \frac{\partial g_j}{\partial u_1}\Delta u_1 + ... + \frac{\partial g_j}{\partial u_r}\Delta u_r \tag{2.7}$$

Finally, the linearized model of the system can be represented in the state-space form as in (2.8), while the observed outputs can be represented by (2.9).

$$\mathbf{\Delta \dot{x}} = \mathbf{A\Delta x} + \mathbf{B\Delta u} \tag{2.8}$$

$$\mathbf{\Delta y} = \mathbf{C\Delta x} + \mathbf{D\Delta u} \tag{2.9}$$

In above equations, $\mathbf{A}$ is the state or plant matrix and $\mathbf{B}$ is the control or input matrix of the system. Matrix $\mathbf{C}$ is the output matrix, while $\mathbf{D}$ is the matrix that specifies the proportion of input directly affecting the output. These matrices consist of partial derivatives of functions $f_i$ and $g_j$ with respect to state variables and inputs. They are evaluated at the initial equilibrium point of the system of which the stability is analysed. Thereafter, the small-signal stability can be determined based on the roots

of the **A** matrix which gives the eigenvalues of the system.

The following sections of this chapter will present the linearized models of various power system components used in this study to analyze SSR, along with their derivation where necessary.

## 2.2 Model of the TCSC

A TCSC is a parallel combination of a fixed capacitor and a Thyristor Controlled Reactor (TCR) as shown in Fig. 2.1a. Back-to-back thyristors are switched at the synchronous frequency (50/60 Hz) with a delay angle $\alpha$, synchronized to the zero crossings of either the line current ($I_L$) or capacitor voltage ($V$). Synchronization to zero crossings of the line current is preferred over the other method due to relatively less harmonic distortions present in the line current. The synchronization is commonly achieved through a Phase Locked Loop (PLL). The firing angle $\alpha$ will eventually control the inductance in TCR branch which effectively changes the impedance of the TCSC. TCSC can operate in three modes depending on the firing angle [33] :

1. **Blocked-thyristor mode** : When thyristors are fully blocked or firing angle is $90^0$ (with respect to zero crossings of the line current). In this mode, no current will pass through the thyristor branch and the TCSC appears as a fixed capacitor of $C$.

2. **Bypassed-thyristor mode** : When thyristors are fired instantly at the zero crossings of the line current with $0^0$ firing angle. Thyristors are fully conducting in this mode and the TCSC becomes inductive with the parallel combination of $L$ and $C$.

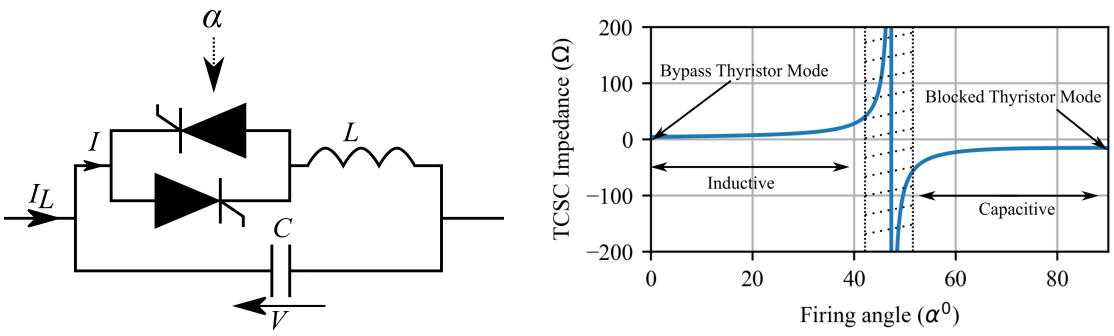


(a) Structure of a TCSC (b) Impedance characteristics of a TCSC

Figure 2.1: TCSC circuit and impedance characteristics

3. **Capacitor/Inductor Vernier mode** : In this mode, the TCSC behaves as a controllable capacitive or inductive reactance by varying firing angles in the range $0^0 - 90^0$, as illustrated by the impedance characteristics curve in Fig. 2.1b. The TCSC impedance in steady state can be expressed as in (2.10). Typically TCSCs are operated in capacitive vernier mode.

$$\begin{aligned} X_{tcsc} = &- X_c + C_1(2(\frac{\pi}{2} - \alpha) + \sin(2(\frac{\pi}{2} - \alpha))) \\ &- C_2(\cos(\frac{\pi}{2} - \alpha))^2(n\tan(n(\frac{\pi}{2} - \alpha)) - \tan(\frac{\pi}{2} - \alpha)) \end{aligned} \tag{2.10}$$

Where,

$$X_c = \frac{1}{2\pi f C} \qquad C_1 = \frac{X_c + X_{lc}}{\pi} \qquad C_2 = \frac{4X_{lc}^2}{\pi X_l}$$

$$n = \sqrt{\frac{X_c}{X_l}} \qquad X_{lc} = \frac{X_c X_l}{X_c - X_l} \qquad X_l = 2\pi f L$$

The region where TCSC reactance change from inductive to capacitive or vice versa is the resonant region and the behaviour of the TCSC is highly non-linear in this region. Even a small change in the firing angle can result in large variations of its impedance. Hence, operation near the parallel resonance should be avoided for stable operation. The firing angle can be maintained fixed (constant firing angle control) or synthesized by upper layer controllers such as line current, impedance or power

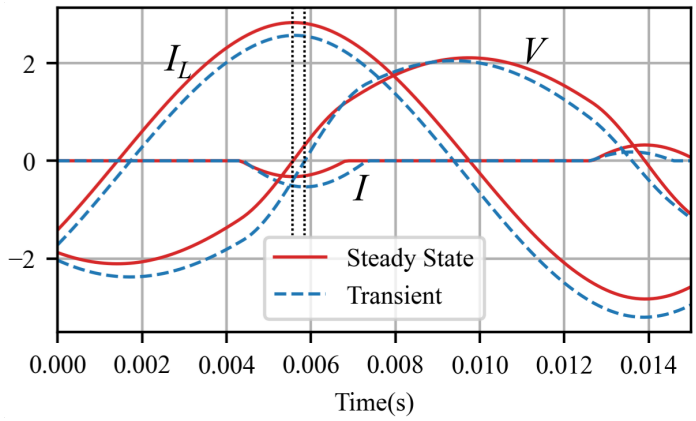


Figure 2.2: Steady state and transient waveforms of the TCSC operating in capacitive region ($I_L$: Line current, $I$: TCR current and $V$: TCSC voltage).

flow controllers which may also include supplementary controls on top, such as Power Oscillation Damping Controllers (PODCs) and SSDCs.

### 2.2.1 Transient Behaviour of the TCSC

The behaviour of a TCSC is non-linear because the thyristor turn-off times depend on the TCR current. Hence, obtaining a linearized analytical model of the TCSC model is challenging and requires certain assumptions. Fig. 2.2 illustrates the EMT waveforms of a TCSC operating in capacitive vernier mode in steady state and during a disturbance. The line current entering TCSC is $I_L$, $I$ is the current through the TCR and $V$ is the voltage across the TCSC. The TCSC is installed in a line supplied with two voltage sources on either side. The transient waveforms in Fig. 2.2 are generated by injecting a sub-synchronous frequency voltage superimposed on one of the voltage sources.

In steady state, the negative peak of the TCR current, zero crossing of TCSC voltage and the positive peak of the line current are in exact coincidence as expected.

During a disturbance, thyristors are fired at the same instant as in steady state, but the conduction time is longer than that in steady state. Thus, the negative peak of the TCR current and the zero crossing of the TCSC voltage do not coincide with the positive peak of the line current. There is a phase shift between the positive peak of the line current and the negative peak of the TCR current (so does the zero crossing of the capacitor voltage). This phenomenon can be thought of as a dynamic resistance which appears in series with the TCSC only during a disturbance adding damping to the circuit. Thus, it is important to model this phase shift to capture the resistive damping presented by the TCSC.

The quasi-steady state model of the TCSC in (2.10) is applicable for electro-mechanical studies but not suitable for SSR analysis as it omits important dynamics of TCSC such as the inductor current dynamics and capacitor voltage dynamics. Furthermore, it does not have any resistive elements modelled that could represent the resistive effects within the sub-synchronous frequency range. DP based representation of the TCSC allows to capture the dynamics of the inductor current and the capacitor voltage.

### 2.2.2 Concept of Dynamic Phasors

The phasor representation of a continuous-time periodic signal (e.g. $A\sin(\omega_s t+\theta)$) is simply the Fourier co-efficients calculated in frequency domain. A continuous-time periodic signal can be expressed in the Fourier series representation as in (2.11), where the complex Fourier co-efficients are calculated over a fixed period $T$ as in (2.12). Note

that the calculated complex Fourier co-efficients are constant (independent of time).

$$x(t) = Re\left\{\sum_{k\geq 0} X_k e^{jk\omega_s t}\right\} \tag{2.11}$$

$$X_k = \frac{c}{T}\int_T x(t)e^{-jk\omega_s t}\,dt =< x >_k \tag{2.12}$$

Where '$k$' is the harmonic number, $\omega_s = 2\pi/T$, $c = 1$ for $k = 0$ and $c = 2$ for $k > 0$. The complex Fourier co-efficients of the derivative of a continuous-time periodic signal can then be calculated as (2.13), where the result is once again a constant.

$$\langle\frac{d}{dt}x\rangle_k = jk\omega_s X_k \tag{2.13}$$

On the contrary, consider the Fourier series representation of the same continuous-time periodic signal within an interval $(t - T, t)$, as shown in (2.14) [57]. Here, the complex Fourier co-efficients are functions of time, as they are evaluated over a period sliding with time as given (2.15).

$$x(\tau) = Re\left\{\sum_{k\geq 0} X_{k(t)} e^{jk\omega_s \tau}\right\}, \tau \in (t - T, t) \tag{2.14}$$

$$X_{k(t)} = \frac{c}{T}\int_{t-T}^{t} x(\tau)e^{-jk\omega_s \tau}\,d\tau =< x >_{k(t)} \tag{2.15}$$

The advantage of time-varying Fourier co-efficients lies within its derivative. The time-varying complex Fourier co-efficients of the derivative of the same continuous-time periodic signal is represented in (2.16), and now includes the dynamic of the phasors $X_{k(t)}$.

$$\langle\frac{d}{dt}x\rangle_{k(t)} = \frac{dX_{k(t)}}{dt} + jk\omega_s X_{k(t)} \tag{2.16}$$

This representation is called the Dynamic Phasor (DP) representation and can be applied to obtain the DP model of the TCSC as in [57].

### 2.2.3 Linearized Model of the TCSC

The natural state variables of the TCSC can be chosen as capacitor voltage $v_{(t)}$ and TCR current $i_{(t)}$ and their behaviour can be characterized by two differential equations (2.17) and (2.18), where $q_{(t)}$ denotes the switching function.

$$C\frac{dv_{(t)}}{dt} = i_{L(t)} - i_{(t)} \tag{2.17}$$

$$L\frac{di_{(t)}}{dt} = q_{(t)}v_{(t)} \tag{2.18}$$

where,

$$q(t) = \begin{cases} 1 & ; \alpha < \omega_0 t < \tau \\ 0 & \text{otherwise} \end{cases}$$

Thyristor turn off time is denoted by $\tau$. The dynamics of the phasors of capacitor voltage $v_{(t)}$ and TCR current $i_{(t)}$ can be obtained by applying the first principles of time varying Fourier co-efficients [57]. Converting the terms in above equations to dynamic phasors while considering the property of derivative given in (2.16), the DP model of the TCSC is obtained as in (2.19) and (2.20).

$$C\frac{dV_k}{dt} = I_{L_k} - I_k - jCk\omega_0 V_k \tag{2.19}$$

$$L\frac{dI_k}{dt} = \langle qv \rangle_k - jLk\omega_0 I_k \tag{2.20}$$

In above equations, terms $V_k$ and $I_k$ denotes the $k^{th}$ harmoinc of the capacitor voltage and TCR current phasor respectively. The term $\langle qv \rangle_k$ is a non-linear term and can be expanded with the property of convolution in phasor domain according to (2.21). Since $q$ and $v$ are real quantities, the relationship in (2.22) is valid, where '*' denotes

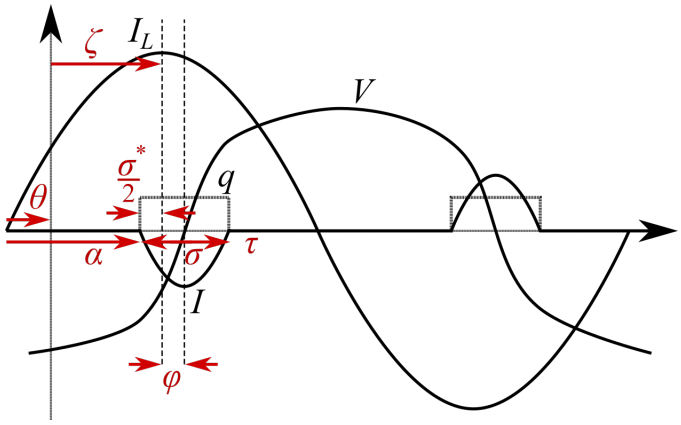


Figure 2.3: Transient waveforms of TCSC operating in capacitive region

the complex conjugate.

$$\langle qv\rangle_k = \sum_{i=-\infty}^{\infty} \langle q\rangle_{k-i}\langle v\rangle_i \tag{2.21}$$

$$\langle v\rangle_{-n} = \langle v\rangle_n^*, \langle q\rangle_{-n} = \langle q\rangle_n^* \tag{2.22}$$

The accuracy of the model depends on how well the non-linearity in the switching term $\langle q\rangle_k$ is estimated. To arrive at an expression for $\langle q\rangle_k$, consider the representation of TCSC waveforms during a transient as in Figure 2.3. The non-linearity in switching during a transient is represented as a phase shift $\phi$ between the opposite polarities of the line current and TCR current which accounts for the dynamic resistance. Phase shift $\phi$ only exist during transient conditions and is zero at steady state. Term $\langle q\rangle_k$ is the average of the switching function $q$ for half a cycle period and it depends on the turn-on and turn-off instants of thyristors.

The turn-on instants of thyristors depends on the controller and/or the synchronization scheme and therefore can be expressed as, '$\zeta - \frac{\sigma^*}{2}$' where $\zeta$ is the phase angle of the peak of the line current. The term $\sigma$ is the actual conduction angle, whereas $\sigma^*$ is the required conduction angle, determined based on the required TCSC impedance

or controller actions. At steady state, $\sigma$ is equal to $\sigma^*$ whereas during transients, the required conduction angle and the actual conduction angle is described by (2.23).

$$\sigma = \sigma^* + 2\phi \tag{2.23}$$

The turn-off instants of the thyristors can be expressed as '$\zeta + 2\phi + \frac{\sigma^*}{2}$' and it further depends on the zero crossing of TCR current which is included in angle '$\phi$' as expressed in (2.24).

$$\phi = \angle - I_1^* I_{L_1} \tag{2.24}$$

Taking these instants into consideration, an expression for $\langle q \rangle_k$ is arrived as in (2.25) and (2.26).

$$\langle q \rangle_k = \frac{2}{k\pi} \sin(\frac{k\sigma}{2})\, e^{-jk(\zeta+\phi)} \tag{2.25}$$

$$\langle q \rangle_0 = \frac{\sigma}{\pi} \tag{2.26}$$

To determine the order of harmonics to be considered in the model, refer to Fig. 2.4 which shows the harmonic content in the capacitor voltage of a TCSC. It is evident that the $3^{rd}$ and $5^{th}$ harmonic content in the TCSC voltage is significant when the thyristor conduction angle is high, while the remaining higher-order harmonics are relatively low.

As such, work in [59] has included effects of $3^{rd}$ and $5^{th}$ harmonic phasors of the TCSC voltage and TCR current as represented from (2.27) - (2.32).

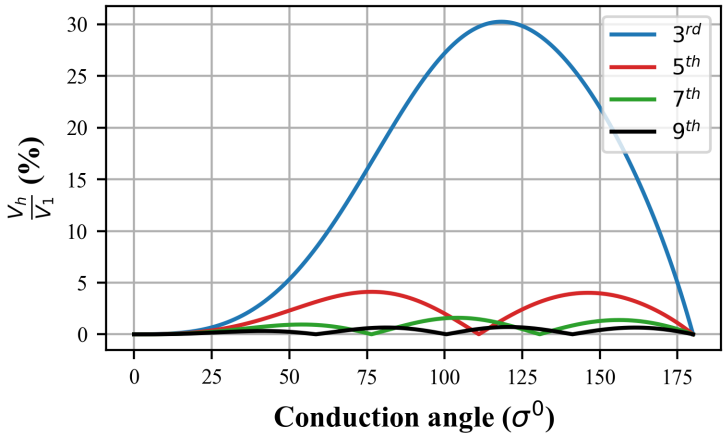


Figure 2.4: Harmonic content in the TCSC voltage

$$C\frac{dV_1}{dt} = I_{L_1} - I_1 - jC\omega_0 V_1 \tag{2.27}$$

$$L\frac{dI_1}{dt} = \langle qv\rangle_1 - jL\omega_0 I_1 \tag{2.28}$$

$$C\frac{dV_3}{dt} = -I_3 - j3C\omega_0 V_3 \tag{2.29}$$

$$L\frac{dI_3}{dt} = \langle qv\rangle_3 - j3L\omega_0 I_3 \tag{2.30}$$

$$C\frac{dV_5}{dt} = -I_5 - j5C\omega_0 V_5 \tag{2.31}$$

$$L\frac{dI_5}{dt} = \langle qv\rangle_5 - j5L\omega_0 I_5 \tag{2.32}$$

Where,

$$\langle qv\rangle_1 = \langle q\rangle_6\langle V\rangle_5^* + \langle q\rangle_4\langle V\rangle_3^* + \langle q\rangle_2\langle V\rangle_1^* + \langle q\rangle_0\langle V\rangle_1 + \langle q\rangle_2^*\langle V\rangle_3 + \langle q\rangle_4^*\langle V\rangle_5$$

$$\langle qv\rangle_3 = \langle q\rangle_8\langle V\rangle_5^* + \langle q\rangle_6\langle V\rangle_3^* + \langle q\rangle_4\langle V\rangle_1^* + \langle q\rangle_2\langle V\rangle_1 + \langle q\rangle_0\langle V\rangle_3 + \langle q\rangle_2^*\langle V\rangle_5$$

$$\langle qv\rangle_5 = \langle q\rangle_{10}\langle V\rangle_5^* + \langle q\rangle_8\langle V\rangle_3^* + \langle q\rangle_6\langle V\rangle_1^* + \langle q\rangle_4\langle V\rangle_1 + \langle q\rangle_2\langle V\rangle_3 + \langle q\rangle_0\langle V\rangle_5$$

$$V_1 = V_{1R} + jV_{1I} \qquad V_3 = V_{3R} + jV_{3I} \qquad V_5 = V_{5R} + jV_{5I}$$

$$I_1 = I_{1R} + jI_{1I} \qquad I_3 = I_{3R} + jI_{3I} \qquad I_5 = I_{5R} + jI_{5I}$$

$$I_{l_1} = I_{l_{1R}} + jI_{l_{1I}} \qquad \langle q \rangle_k = \langle q \rangle_{kR} + j\langle q \rangle_{kI}$$

As transmission lines are highly inductive, the line currents are assumed to be essentially sinusoidal (free from harmonic distortions). Time-domain simulations confirm that this is a valid assumption. Therefore, $I_{L_{3,5}}$ in (2.27) - (2.32) are ignored.

The above model in (2.27)-(2.32) when separated into real and imaginary components, form a 12th order state space system. Incorporating additional controls further increases the order of the system, which adds to the complexity of matrix computation, particularly when handling large networks. Furthermore, obtaining the initial values to initialize the higher-order linearized model of the TCSC is not straightforward as they are not readily available or obtained by any commercial power flow solving software. The only quantities available are the fundamental components of the line currents ($I_{L1}$) and TCSC voltage ($V_1$). Therefore, the order of the model was reduced by ignoring the dynamics of the higher-order terms $V_3, V_5, I_3$ and $I_5$ and treating them as algebraic variables, incorporating their steady state effects on the fundamental components. The simplification was carried out based on the following findings from the small-signal stability assessment and supporting results are presented in Chapter 3.

- The dynamics of $3^{rd}$ and $5^{th}$ order harmonics of the TCSC voltage and TCR current corresponds to very fast dynamics.

- Linearization of $3^{rd}$ and $5^{th}$ harmonic variables makes the small-signal model unstable at certain operating points (when operating close to the non-linear

region of the TCSC), even when the EMT model operation is stable.

- Participation of higher-order terms in sub-synchronous frequency oscillatory modes are very low.

- Ignoring the dynamics of the $3^{rd}$ and $5^{th}$ harmonics of the TCSC voltage and TCR current do not have significant impacts on the frequency response of the TCSC model in sub-synchronous frequency range.

Therefore, based on equations (2.30) and (2.32), $I_3$ and $I_5$ can be written while ignoring their dynamics as:

$$I_3 = \frac{\langle qv \rangle_3}{j3L\omega_0}$$
$$I_5 = \frac{\langle qv \rangle_5}{j5L\omega_0}$$

Terms $V_3$ and $V_5$ can be expressed in terms of fundamental components by solving the following equations:

$$\frac{\langle qv \rangle_3}{j3L\omega_0} + j3C\omega V_3 = 0$$
$$\frac{\langle qv \rangle_5}{j5L\omega_0} + j5C\omega V_5 = 0$$

Thus, the simplified DP model of the TCSC consist of only the dynamics of the fundamental components of the TCSC voltage and TCR current as given by (2.27) and (2.28) and when separated into real and imaginary components, the model is represented by (2.33 - 2.36) .

$$\frac{dV_{1R}}{dt} = \frac{I_{L_{1R}}}{C} - \frac{I_{1R}}{C} + \omega_0 V_{1I} \tag{2.33}$$

$$\frac{dV_{1I}}{dt} = \frac{I_{L_{1I}}}{C} - \frac{I_{1I}}{C} - \omega_0 V_{1R} \tag{2.34}$$

$$\frac{dI_{1R}}{dt} = \frac{\langle qv \rangle_{1R}}{L} + \omega_0 I_{1I} \tag{2.35}$$

$$\frac{dI_{1I}}{dt} = \frac{\langle qv \rangle_{1I}}{L} - \omega_0 I_{1R} \tag{2.36}$$

With the values of $I_{L1}$ and $V_1$ available from the power flow program, initial value of the TCR current can be calculated as,

$$I_1 = I_{L_1} - jC\omega_0 V_1$$

The simplified DP small-signal model can be combined with the rest of the network which is primarily fundamental frequency based. This simplification will reduce the size of the state matrix to the order of 4, reducing the computational burden when it comes to handling large networks while retaining important dynamics of the TCSC for SSR analysis. The linearized model of the TCSC can be expressed as in (2.37).

$$\Delta \dot{\mathbf{x}}_{\mathbf{tcsc}} = \mathbf{A_{tcsc}} \Delta \mathbf{x_{tcsc}} + \mathbf{B_{tcsc}} \Delta \mathbf{u_{tcsc}} + \mathbf{H_{tcsc}} \Delta \mathbf{w_{tcsc}} \tag{2.37}$$

Where,

$$\Delta \mathbf{x_{tcsc}} = [\Delta V_{1R}, \Delta V_{1I}, \Delta I_{1R}, \Delta I_{1I}]^T, \quad \Delta \mathbf{u_{tcsc}} = [\Delta \alpha], \quad \Delta \mathbf{w_{tcsc}} = [\Delta I_{L_{1R}}, \Delta I_{L_{1I}}, \Delta \delta_m]^T$$

The input to the TCSC is the firing angle order $\alpha$ and $\delta_m$ is the angle of the line current generated by the PLL. To interface with the network, the TCSC voltages can be considered as the output to the network as in (2.38) .

$$\Delta \mathbf{y_{tcsc}} = \mathbf{C_{tcsc}} \Delta \mathbf{x_{tcsc}} \tag{2.38}$$

Where,

$$\Delta \mathbf{y_{tcsc}} = [\Delta V_{1R}, \Delta V_{1I}]^T$$

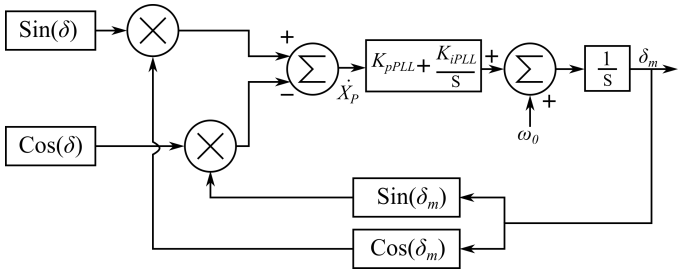


Figure 2.5: Block diagram of the PLL

The matrices $\mathbf{A_{tcsc}}$ , $\mathbf{B_{tcsc}}$, $\mathbf{H_{tcsc}}$ and $\mathbf{C_{tcsc}}$ are given in Appendix A.

## 2.3 Phase Locked Loop Model

The synchronization scheme plays an important role in TCSC dynamics. Firing instants of the thyristors are determined by the phase angle of the line current entering the TCSC. A simplified version of the PLL is used based on the assumption that the three phases are balanced and is shown in Fig. 2.5 [7]. The PLL model introduces two new state variables $X_P$ and $\delta_m$. The actual phase angle $\delta$ is the angle of phasor $I_{L_1}$. Differential equations for the PLL can be written as in (2.39) and (2.40).

$$\dot{X}_P = \sin(\delta)\cos(\delta_m) - \cos(\delta)\sin(\delta_m) \tag{2.39}$$

$$\dot{\delta}_m = K_{p_{PLL}}\dot{X}_P + K_{i_{PLL}}X_P \tag{2.40}$$

Where,

$$\tan\delta = \frac{I_{L_{1I}}}{I_{L_{1R}}}$$

The linearized model of the PLL is,

$$\mathbf{\Delta \dot{x}_{PLL}} = \mathbf{A_{PLL}\Delta x_{PLL}} + \mathbf{H_{PLL}\Delta w_{PLL}} \tag{2.41}$$

Where,

$$\mathbf{\Delta x_{PLL}} = [\Delta X_P, \Delta\delta_m]^T \qquad \mathbf{\Delta w_{PLL}} = [\Delta I_{L_{1R}}, \Delta I_{L_{1I}}]^T$$

$$\mathbf{A_{PLL}} = \begin{bmatrix} 0 & -1 \\ K_{i_{PLL}} & -K_{p_{PLL}} \end{bmatrix}, \quad \mathbf{H_{PLL}} = \begin{bmatrix} -\frac{I^0_{L_{1I}}}{|I^0_{L1}|^2} & \frac{I^0_{L_{1R}}}{|I^0_{L1}|^2} \\ K_{p_{PLL}}\frac{I^0_{L_{1I}}}{|I^0_{L1}|^2} & K_{p_{PLL}}\frac{I^0_{L_{1R}}}{|I^0_{L1}|^2} \end{bmatrix}$$

The output of the PLL '$\delta_m$' is expresses as in (2.42) for the combination with the TCSC.

$$\mathbf{\Delta y_{PLL}} = \mathbf{C_{PLL}}\mathbf{\Delta x_{PLL}} \tag{2.42}$$

Where,

$$\mathbf{C_{PLL}} = \begin{bmatrix} 0 & 1 \end{bmatrix}$$

The required conduction angle $\sigma^*$ for the TCSC will include the dynamics of the PLL as in (2.43).

$$\sigma^* = 2\left(\frac{\pi}{2} - (\alpha - \delta_m + \delta)\right) \tag{2.43}$$

## 2.4 TCSC Current Controller

The firing angle for the TCSC can be maintained constant or generated by upper layer controls such as a current controller. A simple PI controller illustrated in Fig. 2.6 is used as the primary current controller for the TCSC. The output of the PI controller is the impedance of the TCSC and the corresponding firing angle is generated based on the non-linear impedance characteristics of the TCSC given in (2.10). According to the TCSC impedance characteristics, the firing angle can be expressed as a function of the TCSC impedance as,

$$\alpha = f(X_{tcsc})$$

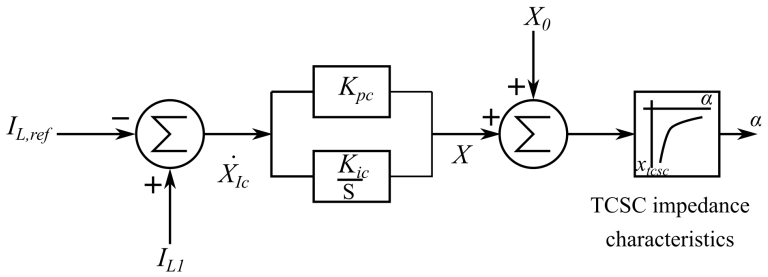


Figure 2.6: Current controller for TCSC

The differential equation of the current controller is given in (2.44) and the output to the TCSC is obtained as in (2.45).

$$\dot{X}_{Ic} = I_{L,ref} - |I_{L1}| \tag{2.44}$$

$$\alpha = f(X_{tcsc})|_{X_{tcsc}=X+X_0} \tag{2.45}$$

$$Z = K_{pc}\dot{X}_{Ic} + K_{ic}X_{Ic} \tag{2.46}$$

In time-domain simulations $\alpha$ can be generated from a pre-defined set of non-linear transfer characteristics (look-up table) obtained according to (2.10). However, to get the linearized characteristics of $\alpha$ Vs. $X_{tcsc}$ relationship, the derivative of the function of $\alpha = f(X_{tcsc})$ must be obtained as in (2.47),

$$\frac{d\alpha}{dX} = \frac{1}{K(\alpha)} \tag{2.47}$$

where,

$$\begin{aligned} K(\alpha) = & -2C1(1+\cos(2(\frac{\pi}{2}-\alpha))) \\ & - C2\left(\left(\cos\left(\frac{\pi}{2}-\alpha\right)\right)^2\left(-\frac{n^2}{\left(\cos\left(n\left(\frac{\pi}{2}-\alpha\right)\right)\right)^2}+\frac{1}{\left(\cos\left(\frac{\pi}{2}-\alpha\right)\right)^2}\right)\right. \\ & \left.+\sin\left(2\left(\frac{\pi}{2}-\alpha\right)\right)\left(n\tan\left(n\left(\frac{\pi}{2}-\alpha\right)\right)-\tan\left(\frac{\pi}{2}-\alpha\right)\right)\right) \end{aligned}$$

Therefore the linearized impedance characteristics around an operating point can be written as,

$$\Delta\alpha = m\Delta X$$

where $m$ can be expressed as in (2.48) in the capacitive region of operation.

$$m = -\frac{1}{K(\alpha_0)} \tag{2.48}$$

The linearized model of the current controller can be expressed as,

$$\mathbf{\Delta \dot{x}_{Ic}} = \mathbf{A_{Ic}} \mathbf{\Delta x_{Ic}} + \mathbf{B_{Ic}} \mathbf{\Delta u_{Ic}} + \mathbf{H_{Ic}} \mathbf{\Delta w_{Ic}} \tag{2.49}$$

Where,

$$\mathbf{\Delta u_{Ic}} = [\Delta I_{L,ref}], \qquad \mathbf{\Delta w_{Ic}} = [\Delta I_{L_{1R}}, \Delta I_{L_{1I}}]$$

$$\mathbf{A_{Ic}} = 0, \qquad \mathbf{B_{Ic}} = 1, \qquad \mathbf{H_{Ic}} = \begin{bmatrix} \frac{I^0_{L_{1R}}}{|I_{L_1}|} \\ \frac{I^0_{L_{1I}}}{|I_{L_1}|} \end{bmatrix}$$

The output to the TCSC can be expressed as,

$$\mathbf{\Delta y_{Ic}} = \mathbf{C_{Ic}} \mathbf{\Delta x_{Ic}} + \mathbf{D_{Ic}} \mathbf{\Delta u_{Ic}} + \mathbf{F_{Ic}} \mathbf{\Delta w_{Ic}} \tag{2.50}$$

Where,

$$\mathbf{\Delta y_{Ic}} = [\Delta \alpha]$$

$$\mathbf{C_{Ic}} = mK_{ic}, \qquad \mathbf{D_{Ic}} = mK_{pc}, \qquad \mathbf{F_{Ic}} = \begin{bmatrix} mK_{pc}\frac{I^0_{L_{1R}}}{|I_{L_1}|} \\ mK_{pc}\frac{I^0_{L_{1I}}}{|I_{L_1}|} \end{bmatrix}$$

## 2.5 Network Model

The ac network comprises passive elements such as transmission line impedances, series and shunt capacitances, transformers, static loads etc. Most of these passive components can be constructed with simple RL series circuits and RC parallel circuits in Fig.2.7. The dynamics of the instantaneous inductor current in RL series circuits and capacitor voltage in parallel RC circuit can be expressed as in (2.51) and (2.52).


(a) Series RL circuit

(b) Parallel RC circuit

Figure 2.7: RL and RC circuit

$$L\frac{di_{(t)}}{dt} = v_{(t)} - Ri_{(t)} \tag{2.51}$$

$$C\frac{dv_{(t)}}{dt} = i_{(t)} - \frac{1}{R}v_{(t)} \tag{2.52}$$

The phasor representation of the above equations are,

$$jk\omega_0 LI_k = V_k - RI_k$$

$$jk\omega_0 CV_k = I_k - \frac{1}{R}V_k$$

In conventional small-signal stability analysis, the ac network is modelled as constant admittances as above considering the fundamental phasors (RL and RC circuits do not generate harmoincs, therefore $k$=1). This kind of representation excludes the dynamics of the inductor current and capacitor voltage fundamental component phasors, making it inadequate for analyzing fast transients like SSO and therefore, DP models of the network that include these dynamics must be used [7]. Conventional models are suitable for analysing low frequency electro-mechanical oscillations.

With the property of derivative of time-varying Fourier co-efficients explained in section 2.2.2, the fundamental component DP models of the series RL and parallel RC circuits can be obtained as in (2.53) and (2.54).

$$L\frac{dI_1}{dt} + j\omega_0 L I_1 = V_1 - RI_1 \tag{2.53}$$

$$C\frac{dV_1}{dt} + j\omega_0 C V_1 = I_1 - \frac{1}{R}V_1 \tag{2.54}$$

Seperating the above equations to real and imaginary components of the phasors ($V_1 = V_{1R} + jV_{1I}$ and $I_1 = I_{1R} + jI_{II}$) and when $L$ and $C$ are in pu, the linearized DP small-signal model of series RL circuit given by (2.55) and parallel RC circuit is given by (2.56).

$$\begin{bmatrix} \Delta\dot{I}_{1R} \\ \Delta\dot{I}_{1I} \end{bmatrix} = \begin{bmatrix} -\frac{R\omega_0}{L} & \omega_s \\ -\omega_s & -\frac{R\omega_0}{L} \end{bmatrix} \begin{bmatrix} \Delta\dot{I}_{1R} \\ \Delta\dot{I}_{1I} \end{bmatrix} + \begin{bmatrix} \frac{\omega_0}{L} & 0 \\ 0 & \frac{\omega_0}{L} \end{bmatrix} \begin{bmatrix} \Delta\dot{V}_{1R} \\ \Delta\dot{V}_{1I} \end{bmatrix} \tag{2.55}$$

$$\begin{bmatrix} \Delta\dot{V}_{1R} \\ \Delta\dot{V}_{1I} \end{bmatrix} = \begin{bmatrix} -\frac{\omega_0}{RC} & \omega_s \\ -\omega_s & -\frac{\omega_0}{RC} \end{bmatrix} \begin{bmatrix} \Delta\dot{V}_{1R} \\ \Delta\dot{V}_{1I} \end{bmatrix} + \begin{bmatrix} \frac{\omega_0}{C} & 0 \\ 0 & \frac{\omega_0}{C} \end{bmatrix} \begin{bmatrix} \Delta\dot{I}_{1R} \\ \Delta\dot{I}_{1I} \end{bmatrix} \tag{2.56}$$

Above linearized models of RL and RC circuits can be combined using Kirchoff's laws to form the linearized model of the entire passive AC network. The TCSC voltage is also combined with RL and RC circuit with Kirchoff's laws.

The linearized model of the network can be written as,

$$\mathbf{\Delta\dot{x}_n} = \mathbf{A_n}\mathbf{\Delta x_n} + \mathbf{B_n}\mathbf{\Delta u_n} + \mathbf{E_n}\mathbf{\Delta v_n} + \mathbf{E_{n_{tcsc}}}\mathbf{\Delta v_{tcsc}} \tag{2.57}$$

Where $\mathbf{x_n}$ are the state variables of the network containing inductor currents and capacitor voltages, $\mathbf{u_n}$ are the inputs to the network, $\mathbf{v_n}$ are the unknown nodal voltages and $\mathbf{v_{tcsc}}$ are the TCSC voltages in the network. The additional term $\mathbf{E_{n_{tcsc}}}\mathbf{\Delta v_{tcsc}}$ in (2.57) is to include TCSC voltages in the network. Nodal current injections to the network can be expressed in terms of network state variables as in (2.58). This

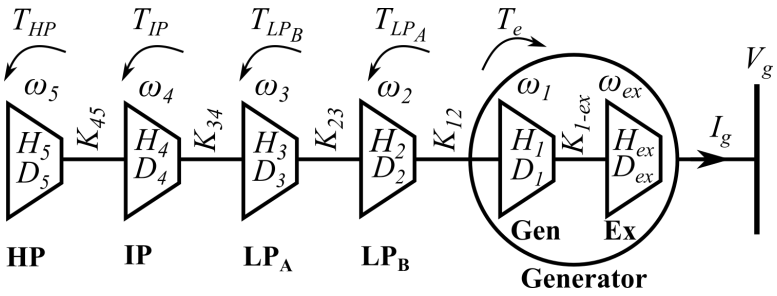

Figure 2.8: Generator with Multi-Mass

equation is useful when interfacing devices to the network.

$$\mathbf{\Delta y_n} = \mathbf{C_n \Delta x_n} \tag{2.58}$$

Line currents in branches where TCSCs are installed are interfacing variables to the TCSC. Hence, the TCSC line currents can be expressed in terms of network state variables as in (2.59).

$$\mathbf{\Delta y_{n_{tcsc}}} = \mathbf{C_{n_{tcsc}} \Delta x_n} \tag{2.59}$$

## 2.6 Generator model

### 2.6.1 Multi-Mass Model

In conventional small-signal stability analysis, which primarily focuses on electromechanical oscillations, the CTG are represented as a single mass model. This representation reveals oscillations of the entire turbine-generator rotor with respect to other generators. For SSO studies, the turbine generator system must be modelled as individual masses to represent torsional oscillations between different masses along the turbine-shaft. The dynamic model of a typical four mass turbine of a CTG, as shown in Fig. 2.8, which consist of two low pressure tubines, one intermediate and one high pressure turbine is given in [1] and is shown from (2.60) to (2.67).

$$2H_2\frac{d(\Delta\omega_2)}{dt} = T_{LP_A} + K_{23}(\delta_3 - \delta_2) - K_{12}(\delta_2 - \delta_1) - D_2(\delta\omega_2) \tag{2.60}$$

$$2H_3\frac{d(\Delta\omega_3)}{dt} = T_{LP_B} + K_{34}(\delta_4 - \delta_3) - K_{23}(\delta_3 - \delta_2) - D_3(\delta\omega_3) \tag{2.61}$$

$$2H_4\frac{d(\Delta\omega_4)}{dt} = T_{IP} + K_{45}(\delta_5 - \delta_4) - K_{34}(\delta_4 - \delta_3) - D_4(\delta\omega_4) \tag{2.62}$$

$$2H_5\frac{d(\Delta\omega_5)}{dt} = T_{HP} - K_{45}(\delta_5 - \delta_4) - D_5(\delta\omega_5) \tag{2.63}$$

$$\frac{d\delta_2}{dt} = (\Delta\omega_2)\omega_0 \tag{2.64}$$

$$\frac{d\delta_3}{dt} = (\Delta\omega_3)\omega_0 \tag{2.65}$$

$$\frac{d\delta_4}{dt} = (\Delta\omega_4)\omega_0 \tag{2.66}$$

$$\frac{d\delta_5}{dt} = (\Delta\omega_5)\omega_0 \tag{2.67}$$

The terms $K_*$ are the stiffness co-efficients of the shaft sections in pu torque/ elec. rad, $H_*$ is the per unit inertia constants in seconds, $D_*$ is the damping co-efficient in pu torque/pu speed deviation and $T_*$ is the torque share of each turbine mass. Note that the equations corresponding to the generator and exciter are not included above. The electrical torque $T_e$ can be formulated in terms of synchronous machine state variables.

### 2.6.2 Machine Model

The dynamic model of the synchronous generator used in conventional small-signal stability studies does not include the dynamics of stator fluxes [1]. For SSO studies, to be consistent with the DP network representation, it is necessary to include the dynamics of the stator d-axis and q-axis fluxes [7]. Therefore, the CTG is modelled as an $8^{\text{th}}$ order model as represented below.

$$\frac{d\psi_d}{dt} = \omega_0(\psi_q\omega_1 + R_a i_d + e_d) \tag{2.68}$$

$$\frac{d\psi_q}{dt} = \omega_0(-\psi_d\omega_1 - R_a i_q + e_q) \tag{2.69}$$

$$\frac{d\psi_{fd}}{dt} = \omega_0\left(\frac{R_{fd}}{L_{ad}}E_{fd} - \frac{R_{fd}}{L_{fd}}\left(\psi_{fd} - L_{ad}^{"}(-i_d + \frac{\psi_{fd}}{L_{fd}} + \frac{\psi_{1d}}{L_{1d}})\right)\right) \tag{2.70}$$

$$\frac{d\psi_{1d}}{dt} = \omega_0\left(-\frac{R_{1d}}{L_{1d}}\left(\psi_{1d} - L_{ad}^{"}(-i_d + \frac{d\psi_{fd}}{L_{fd}} + \frac{\psi_{1d}}{L_{1d}})\right)\right) \tag{2.71}$$

$$\frac{d\psi_{1q}}{dt} = \omega_0\left(-\frac{R_{1q}}{L_{1q}}\left(\psi_{1q} - L_{aq}^{"}(-i_q + \frac{d\psi_{1q}}{L_{1q}} + \frac{\psi_{2q}}{L_{2q}})\right)\right) \tag{2.72}$$

$$\frac{d\psi_{2q}}{dt} = \omega_0\left(-\frac{R_{2q}}{L_{2q}}\left(\psi_{2q} - L_{aq}^{"}(-i_q + \frac{d\psi_{1q}}{L_{1q}} + \frac{\psi_{2q}}{L_{2q}})\right)\right) \tag{2.73}$$

$$2H_1\frac{d(\omega_1)}{dt} = T_m - T_e - D_1(\omega_1) \tag{2.74}$$

$$\frac{d\delta_1}{dt} = (\Delta\omega_1)\omega_0 \tag{2.75}$$

where,

$$i_d = -\frac{L_d^{"}}{L_l}\left(\frac{1}{L_{ad}} + \frac{1}{L_{fd}} + \frac{1}{L_{1d}}\right)\psi_d + \left(\frac{1}{L_{fd}L_l}\right)\psi_{fd} + \left(\frac{1}{L_{1d}L_l}\right)\psi_{1d}$$

$$i_q = -\frac{L_q^{"}}{L_l}\left(\frac{1}{L_{aq}} + \frac{1}{L_{1q}} + \frac{1}{L_{2q}}\right)\psi_q + \left(\frac{1}{L_{1q}L_l}\right)\psi_{1q} + \left(\frac{1}{L_{2q}L_l}\right)\psi_{2q}$$

And

$$T_e = \psi_d i_q - \psi_q i_d$$

Terms $e_d$ and $e_q$ in above equations are the d and q axis components of the generator terminal voltage $V_g$ which is an unknown and is solved when combining with the network. The synchronous machine model together with the 4 turbine multi-mass model forms a $16^{th}$ order model of which the state space model can be expressed after linearization as in (2.76). Note that when the multi-mass model is combined with the synchronous machine equations, the input torque $T_m$ to the machine in (2.74) will be

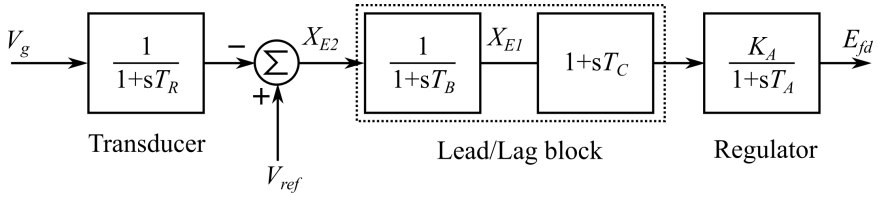


Figure 2.9: AC4A Exciter block diagram

$K_{12}(\delta_2 - \delta_1)$, as the input torque is already distributed among the turbine masses.

$$\mathbf{\Delta \dot{x}_g} = \mathbf{A_g \Delta x_g} + \mathbf{B_g \Delta u_g} + \mathbf{E_g \Delta v_g} \tag{2.76}$$

Where,

$$\mathbf{\Delta x_g} = [\Delta\psi_d, \Delta\psi_q, \Delta\psi_{fd}, \Delta\psi_{1d}, \Delta\psi_{1q}, \Delta\psi_{2q},$$
$$\Delta\omega_1, \Delta\delta_1, \Delta\omega_2, \Delta\delta_2, \Delta\omega_3, \Delta\delta_3,$$
$$\Delta\omega_4, \Delta\delta_4, \Delta\omega_5, \Delta\delta_5]^T$$
$$\mathbf{\Delta u_g} = [\Delta e_{fd}, \Delta T_{LP_A}, \Delta T_{LP_B}, \Delta T_{IP}, \Delta T_{HP}]^T$$
$$\mathbf{\Delta v_g} = [\Delta V_{gR}, \Delta V_{gI}]^T$$

Current injections from the generator can be expressed as in (2.77) to be interfaced with the network.

$$\mathbf{\Delta i_g} = \mathbf{C_g \Delta x_g} \tag{2.77}$$

The matrices $\mathbf{A_g}, \mathbf{B_g}, \mathbf{E_g}$ and $\mathbf{C_g}$ are given in the Appendix B.

### 2.6.3 Exciter Model

An AC4A exciter model illustrated in Fig.2.9 is used with the generator model where required. Dynamics of the exciter can be represented with three state equation as in (2.78-2.80)

$$\dot{E}_{fd} = -\frac{1}{T_A}E_{fd} + \frac{K_A}{T_A}\left(1 - \frac{T_C}{T_B}\right)X_{E1} + \frac{K_A T_C}{T_B T_A}X_{E2} \tag{2.78}$$

$$\dot{X}_{E2} = -\frac{1}{T_A}X_{E2} - \frac{1}{T_r}V_g + \frac{1}{T_r}V_{ref} \tag{2.79}$$

$$\dot{X}_{E1} = -\frac{1}{T_B}X_{E1} + \frac{1}{T_B}X_{E2} \tag{2.80}$$

The field voltage $E_{fd}$ in the generator model (2.70) which was previously an input, is now provided by the exciter. Furthermore, if the exciter's inertia is significant, it may be necessary to model the mechanical dynamics of the exciter mass. In such instances, the multi-mass model will include two additional state equations, as in (2.81) and (2.82).

$$2H_{ex}\frac{d(\Delta\omega_{ex})}{dt} = K_{ex}(\delta_{ex} - \delta_1) - D_{ex}(\delta\omega_{ex}) \tag{2.81}$$

$$\frac{d\delta_{ex}}{dt} = (\Delta\omega_{ex})\omega_0 \tag{2.82}$$

The linearized state space model of the exciter can be expressed as,

$$\mathbf{\Delta\dot{x}_{ex}} = \mathbf{A_{ex}\Delta x_{ex}} + \mathbf{B_{ex}\Delta u_{ex}} + \mathbf{E_{ex}\Delta v_{ex}} \tag{2.83}$$

Where,

$$\mathbf{\Delta x_{ex}} = [\Delta E_{fd}, \Delta X_{E2}, \Delta X_{E1}]^T$$

$$\mathbf{\Delta u_{ex}} = [\Delta V_{ref}]T$$

$$\mathbf{\Delta v_{ex}} = [\Delta V_{gR}, \Delta V_{gI}]^T$$

$$\mathbf{A_{ex}}(1,1) = \frac{-1}{T_A} \qquad \mathbf{A_{ex}}(1,2) = \frac{K_A T_C}{T_A T_B} \qquad \mathbf{A_{ex}}(1,3) = \frac{K_A}{T_A}\left(1 - \frac{T_C}{T_B}\right)$$

$$\mathbf{A_{ex}}(2,2) = \frac{-1}{T_A} \qquad \mathbf{A_{ex}}(3,2) = \frac{1}{T_B} \qquad \mathbf{A_{ex}}(3,3) = \frac{-1}{T_B}$$

$$\mathbf{B_{ex}}(2,1) = \frac{-1}{T_r}$$

$$\mathbf{E_{ex}}(2,1) = \frac{V_{gR}^0}{|V_g^0|} \qquad \mathbf{E_{ex}}(2,2) = \frac{V_{gI}^0}{|V_g^0|}$$

## 2.7 Wind Power Plant Model

This analysis uses a Type-3 WPP model presented in [20] to study the applicability of TCSC in mitigating W-SSCI. This model encompasses a DFIG, a three-mass drive train for torsional dynamics representation, rotor side and grid side converters, and a converter transformer. Similar to the representation of the CTG, the dynamics of a WPP can be represented through a set of differential equations and current injections as in (2.84) and (2.85), which can then be integrated with the rest of the network.

$$\mathbf{\Delta \dot{x}_w} = \mathbf{A_w \Delta x_w} + \mathbf{B_w \Delta u_w} + \mathbf{E_w \Delta v_w} \tag{2.84}$$

$$\mathbf{\Delta i_w} = \mathbf{C_w \Delta x_w} \tag{2.85}$$

The linearized model for a Type-3 wind power plant (WPP), along with details about the matrices $\mathbf{A_w}, \mathbf{B_w}, \mathbf{E_w}$ and $\mathbf{C_w}$ can be found in [20].

## 2.8 Combination of Linearized models of the power System

The combination of linearized models is carried out in two steps:

1. Combination of the TCSC model with the passive ac network
2. Integrating the device to the network

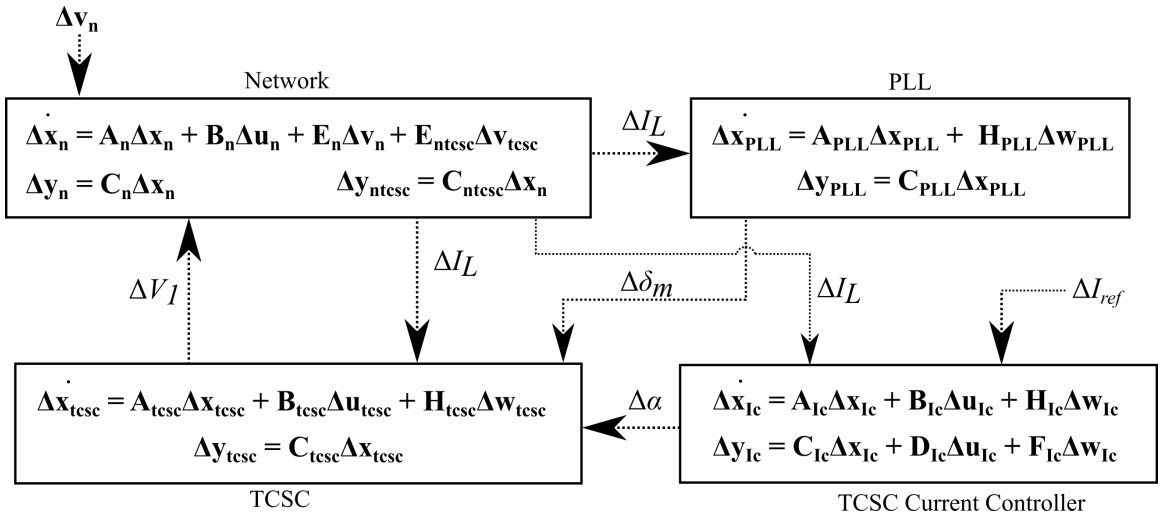


Figure 2.10: Combination of TCSC, PLL and network small-signal models

The linearized models of the TCSC, current controller and PLL is combined with the linearized network equations as shown in Fig. 2.10. The linearized model of the entire network with the TCSC can then be represented as in (2.86).

$$\mathbf{\Delta \dot{x}_N} = \mathbf{A_N \Delta x_N} + \mathbf{B_N \Delta u_N} + \mathbf{E_N \Delta v_N} \tag{2.86}$$

Where,

$$\mathbf{\Delta x_N} = \begin{bmatrix} \mathbf{\Delta x_n} \\ \mathbf{\Delta x_{tcsc}} \\ \mathbf{\Delta x_{PLL}} \\ \mathbf{\Delta x_{Ic}} \end{bmatrix} \qquad \mathbf{\Delta u_N} = \begin{bmatrix} \mathbf{\Delta u_n} \\ \mathbf{\Delta u_{tcsc}} \\ \mathbf{\Delta u_{Ic}} \end{bmatrix}$$

$$\mathbf{\Delta v_N} = [\mathbf{\Delta v_n}]$$

Figure 2.11 illustrates the integration of small-signal models for the generator and the network with TCSC. Similar to EMT type programs, a large fictitious resistor '$R_{sh}$' is connected at the interface bus to avoid any numerical instabilities that can arise when interfacing two independent state variables[20]. However, if there is already

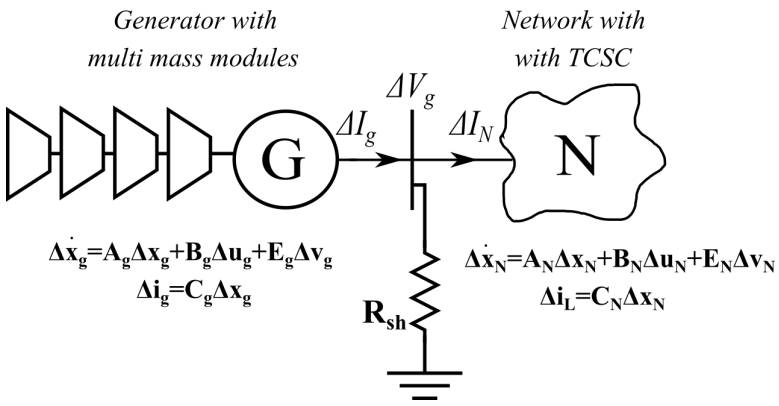


Figure 2.11: Interfacing generator and network

a resultant shunt capacitance at the terminal (e.g. transmission line), there is no need for a fictitious resistor. The unknown voltages in the network and device state equations can be solved using Kirchoff's law applied at the interface node. The interface bus voltage '$V_g$' can be calculated as in (2.87) and expressed in terms of generator and network state variables.

$$\Delta V_g = R_{sh}(\Delta I_g - \Delta I_N) \tag{2.87}$$

Finally the linearized models of the network with TCSCs and the device can be combined to create the overall linearized state space model of the system as given in (2.88).

$$\boldsymbol{\Delta\dot{x}} = \mathbf{A}\boldsymbol{\Delta x} + \mathbf{B}\boldsymbol{\Delta u} \tag{2.88}$$

Where,

$$\boldsymbol{\Delta x} = \begin{bmatrix} \boldsymbol{\Delta x_g} \\ \boldsymbol{\Delta x_N} \end{bmatrix} \qquad \boldsymbol{\Delta u} = \begin{bmatrix} \boldsymbol{\Delta u_g} \\ \boldsymbol{\Delta u_N} \end{bmatrix}$$

Integration of the Type-3 WPP model with the network, follows the same procedure explained above.

## 2.9 Conclusions

This chapter presented the linearized model development of power system components which are used to analyse SSO phenomena, with a detailed discussion on derivation of an existing higher-order DP TCSC model. After a thorough investigation, the existing higher-order DP model of the TCSC was adopted for small signal stability analysis, by simplifying it to its fundamental frequency components. The dynamics of the higher order harmonics were ignored and treated as algebraic quantities. Additionally, the chapter explains the mechanism behind the TCSC's inherent resistive damping and its representation in the DP model. The transient phase shift is associated only with the fundamental frequency components, and is retained in the simplified model. The simplified model of the TCSC can be easily combined with linearized dynamic phasor models of other power system components which are primarily fundamental frequency based.

# Chapter 3

# Validation of Linearized Models

This chapter presents validation of the linearized models developed in Chapter 2 against EMT simulations, which is the closest approximation to the real world behaviour of power system components. It is important to clarify that linearized models are not intended for time-domain simulations. However, to draw conclusions from small-signal stability analysis, accuracy of linearized models around the operating point at which it was linearized must be assessed first. Confidence on the accuracy of a linearized model can be gained by comparing the time responses of the linearized model against EMT simulations, following small disturbances around the point at which the models were linearized.

Comparing the time responses of a linearized model and EMT simulations, particularly when the system is transitioning back to its original equilibrium point after removing the disturbance, is reasonable. This is because the linearized model's behavior is most accurate near the operating point for which it was linearized. If the system transitions to another operating point following a step disturbance, the behavior predicted by the linearized model may not be as accurate.

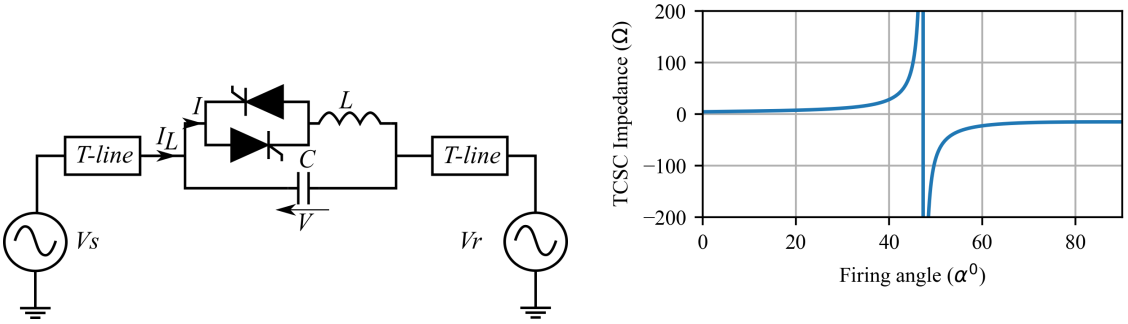


(a) (b)

Figure 3.1: (a)Test circuit with a series compensated line, and (b)Impedance characteristics of the TCSC

The validation process for the linearized models is systematically presented in steps. This chapter also includes small-signal stability results to support the simplification carried out to the higher-order DP model of the TCSC.

## 3.1 TCSC Model

To validate the simplified DP small-signal model of the TCSC, a test circuit is formed with a series compensated transmission line connecting two voltage sources as shown in Fig. 3.1a. Series compensation is fully achieved with a TCSC (i.e. no FSC) and is operated with fixed firing angle control. Circuit parameters are given in Table 3.1. The impedance characteristics of the TCSC used is shown in Fig. 3.1b and the TCSC is operated in its capacitive region. The resonant condition occurs at $\alpha = 47^0$, and the lower limit of the firing angle within the capacitive region was set at $\alpha = 53^0$, just when the EMT simulation becomes unstable.

The $12^{th}$ order DP model of the TCSC was linearized at different operating points along its impedance characteristics curve from $\alpha = 90^0$ to $\alpha = 53^0$ and combined with

Table 3.1: Test System Parameters

| Parameter | Value | Parameter | Value |
|---|---|---|---|
| $V_s$ | $1\angle 0$ pu | $V_r$ | $1\angle -15^0$ pu |
| $X_L$ | 0.0136 pu | $X_C$ | 0.0603 pu |
| $K_{pPLL}$ | 50 rad/s | $K_{iPLL}$ | 900 rad/s$^2$ |
| $T-line$ | $0.2808\angle 86.5^0$ pu | | |

Impedances and voltages are expressed in the base of
1000 MVA and 500 kV at 60 Hz nominal frequency

Table 3.2: Eigenvalues, Frequency, and Damping of Modes in test system

| Mode | Eigenvalue | Frequency (Hz) | Damping (%) |
|---|---|---|---|
| 1 | $-3124.95 \pm 1820.70i$ | 289.77 | 86.40 |
| 2 | $-9.85 \pm 1929.05i$ | 307.02 | 0.51 |
| 3 | $-21.73 \pm 1841.24i$ | 293.04 | 1.18 |
| 4 | $-22.78 \pm 1125.11i$ | 179.07 | 2.02 |
| 5 | $-11.25 \pm 1136.47i$ | 180.88 | 0.99 |
| 6 | $-28.63 \pm 553.73i$ | 88.13 | 5.16 |
| 7 | $-28.84 \pm 198.49i$ | 31.59 | 14.38 |
| 8 | $-25.18 \pm 16.68i$ | 2.65 | 83.37 |

the linearized model of the circuit. Eigen values of the combined system obtained at $\alpha = 80^0$ is shown in Table 3.2 as an example. The contributions of state variables to modes can be obtained with participation factor analysis. Main contributors to the high frequency modes 1 through 5 are the TCSC states. Mode 6 and 7 are the super-synchronous and sub-synchronous mode, respectively, while the low-frequency mode 8 is attributed to the PLL.

Mode 1 is adequately damped at all operating points and poses no significant concerns. It is associated with the fundamental component current of the TCR. Figure 3.2 shows the frequency and damping of the remaining high frequency modes when lowering the firing angle from $\alpha = 90^0$ to $\alpha = 53^0$. It can be seen that mode 2 and 5 becomes unstable when the firing angle is reduced, i.e. when the TCSC is operating close to its resonant region (highly non-linear region).

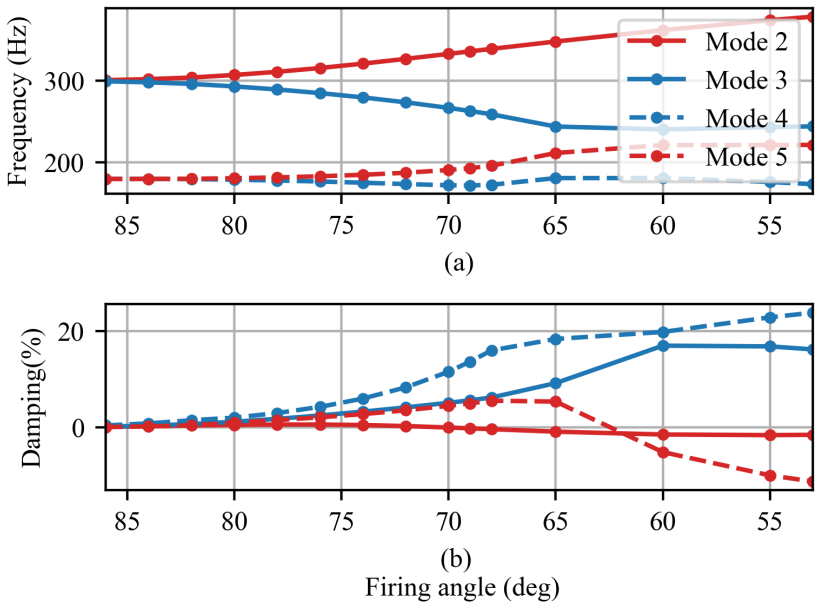


Figure 3.2: Frequency and damping of high frequency modes of the TCSC at multiple operating points

Results from participation factor analysis at different operating points are illustrated in Fig. 3.3. As seen from Fig. 3.3a, aside from the participation of the TCR fundamental current, the 3rd and 5th order harmonics of the TCSC voltage and TCR current also contribute to the high frequency modes. Specificcaly, mode 2 and 3 are mainly affected by the 5th harmonic, whereas mode 4 and 5 are affected by the third harmonic.

Upon lowering the firing angle, as observed in Fig. 3.3b, mode 2 becomes unstable with the highest participation from the 5th order harmonics. Additionally, mode 5 becomes unstable with significant participation from both 3rd and 5th harmonics. At the lower limit of the firing angle ($\alpha = 53°$), the participation of higher-order harmonics reaches nearly 100% in the two unstable modes.

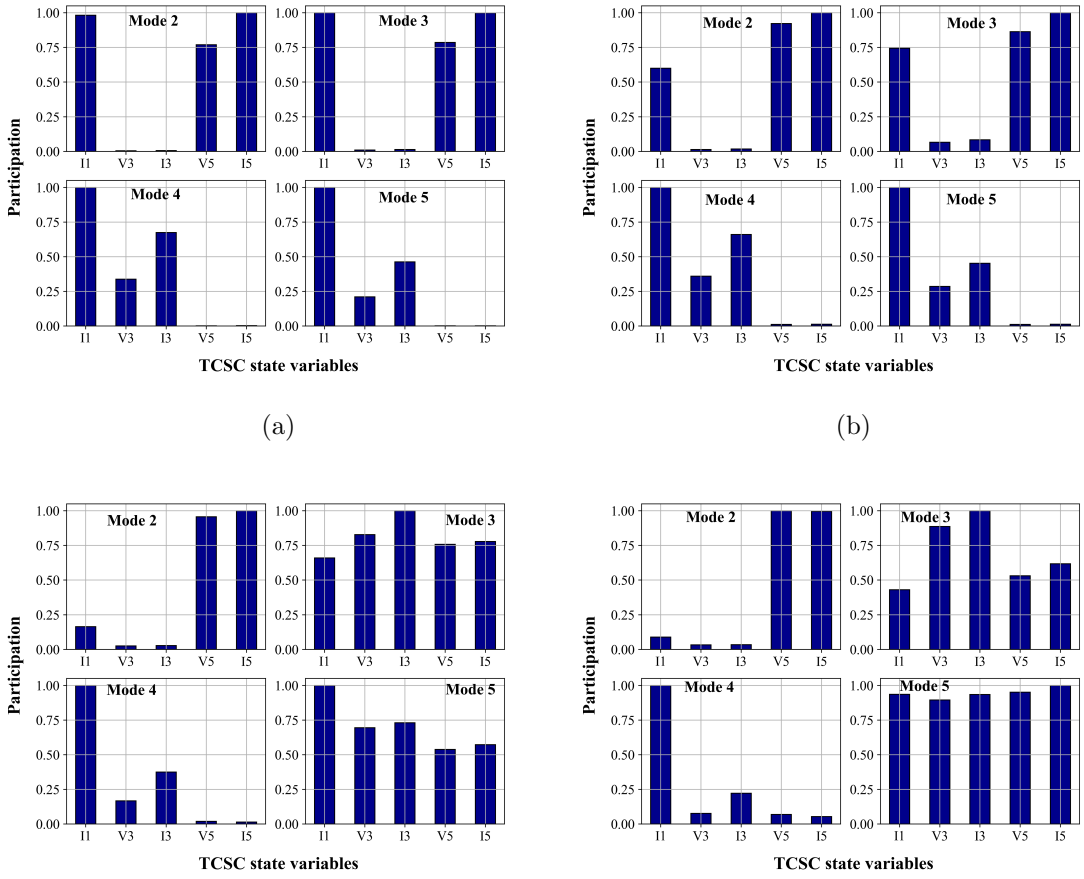


Figure 3.3: Participation of state variables to high frequency modes at $\alpha$ = (a) $76^0$,(b) $70^0$,(c) $60^0$ and (d) $53^0$

The participation of state variables in the network mode, at different firing angles until the model becomes unstable, is illustrated in Fig. 3.4. It can be seen that the highest participants are the network current ($I_{L1}$) and ($V_1$), with increased participation from the TCR current at lower firing angles. An important observation is that the participation from $3^{\text{rd}}$ and $5^{\text{th}}$ harmonic variables is almost negligible.

Hence, ignoring the dynamics of higher-order terms is not expected to have significant impacts on the sub-synchronous modes, and the reduced model remains stable

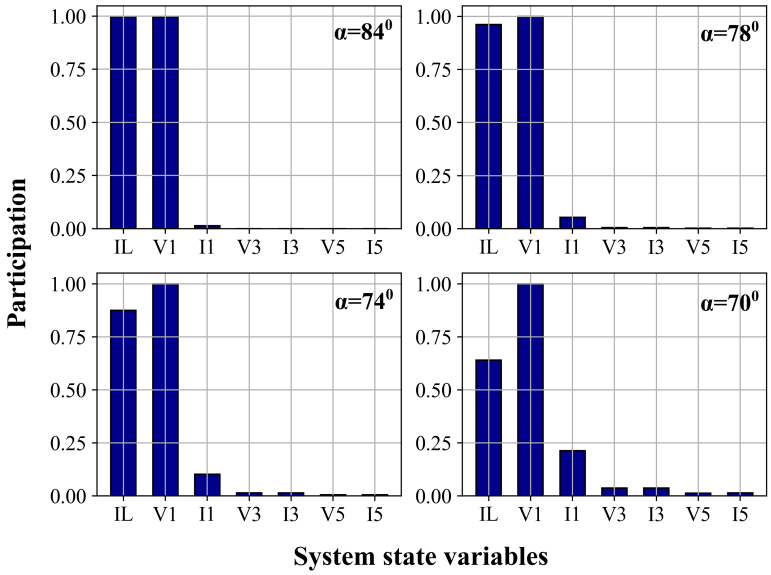


Figure 3.4: Participation factors of the network mode at different firing angles

at operating points near the resonant region.

To investigate the effect of ignoring the dynamics of the higher-order terms on the impedance characteristics of the TCSC within the sub-synchronous frequency range, frequency responses between the TCSC voltage and input line current were derived from both the linearized higher-order and reduced models. Figures 3.5 - 3.7 shows the comparisons of frequency response of the TCSC at three firing angles, Fig. 3.7 being the one at the lower firing angle limit. In general, the frequency response of the reduced model shows a considerable good match with the higher-order model. However, slight discrepancies are noticed at frequencies close to the synchronous frequency at the lower firing angle limit.

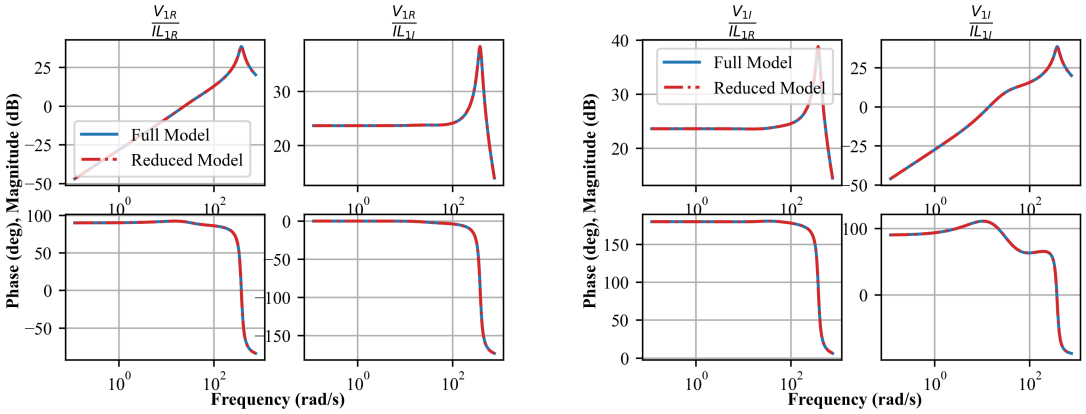


(a) (b)

Figure 3.5: Bode plots of the TCSC at $\alpha = 80^0$

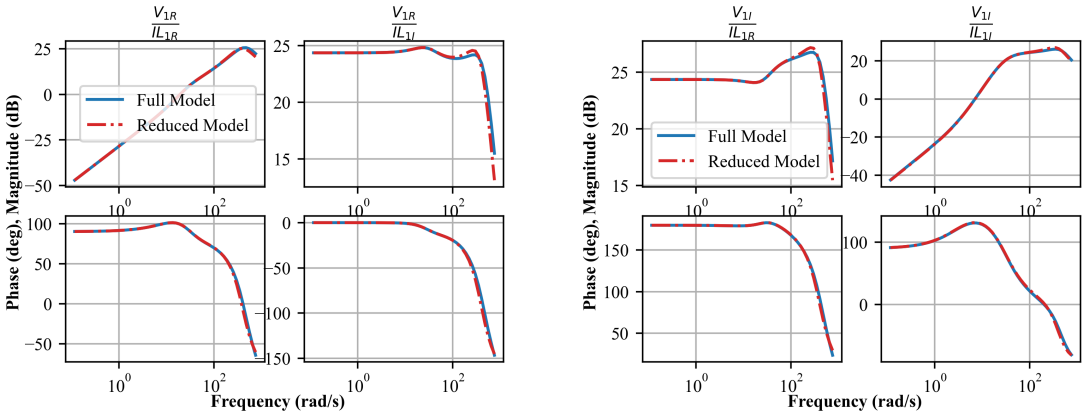


(a) (b)

Figure 3.6: Bode plots of the TCSC at $\alpha = 70^0$

To validate the reduced linearized DP model of the TCSC against EMT simulations, a small disturbance of 5% increment to the receiving end voltage ($V_r$) was applied for 100ms at 2s. The model is validated at four different operating points ($\alpha = 83^0, 73^0, 63^0$, and $53^0$) in the capacitive region. The goal was to validate the model as close as possible to the resonant condition which occurs at $\alpha = 47^0$. Fig. 3.8 shows the comparison of line current responses of the small-signal model against

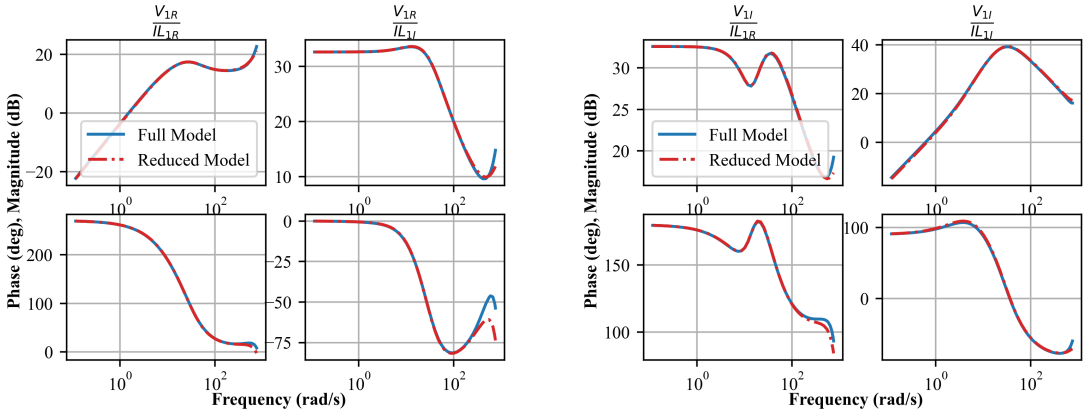


(a) (b)

Figure 3.7: Bode plots of the TCSC at $\alpha = 53^0$

EMT simulations at the four operating points. It is observed that the simplified DP small-signal model tracks the envelop of the PSCAD waveforms quiet accurately.

The frequency responses of the TCSC are obtained at $\alpha = 53^0, 63^0, 73^0$, and $83^0$, through EMT simulations using the d-q based frequency scanning technique [60]. The frequency characteristics are extracted by injecting a wide-band current signal 'Schroeder multi-sine' [61] with frequencies upto 60 Hz, superimposed on an external current source driving the TCSC. Comparisons between the frequency responses of the TCSC from EMT simulations and the simplified DP model in the sub-synchronous frequency range is shown in Figs. 3.9- 3.12. The frequency characteristics of the simplified DP small-signal model of the TCSC closely match those obtained through EMT simulations in the sub-synchronous frequency range. However, when the TCSC operates very close to its non-linear range (at the lower firing angle limit), slight discrepancies in the frequency characteristics are observed

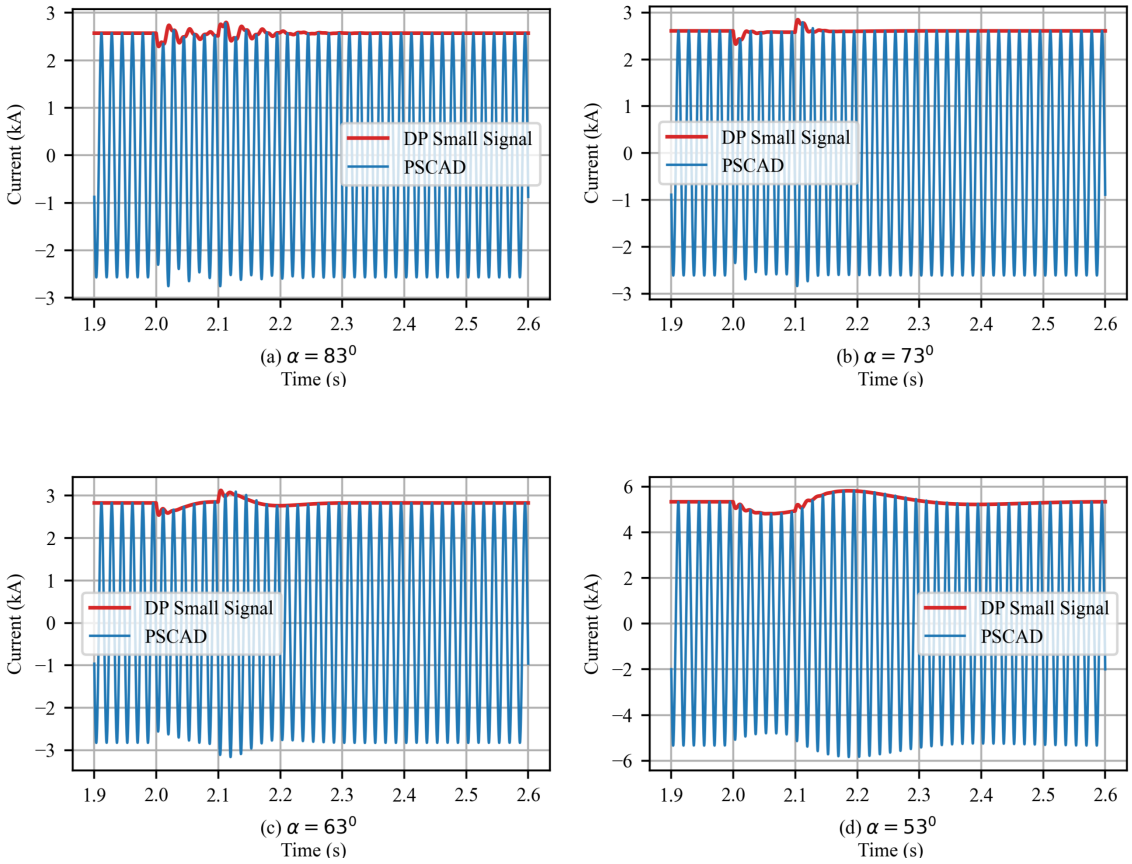


Figure 3.8: Comparison of line current responses of the small-signal model with EMT simulation

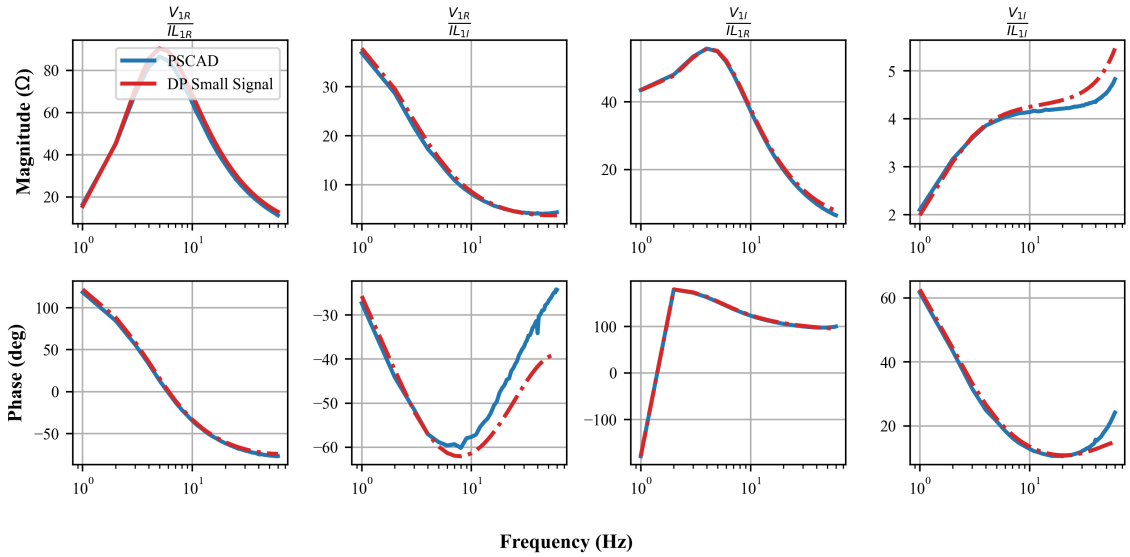


Figure 3.9: Frequency response of the TCSC obtained from the DP small-signal model and PSCAD at $\alpha = 53^0$

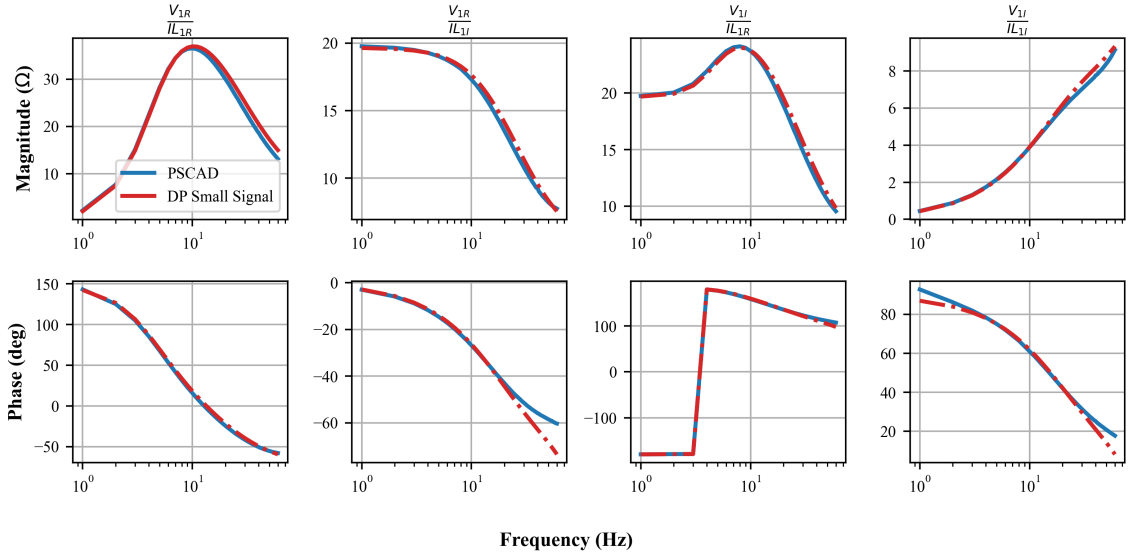


Figure 3.10: Frequency response of the TCSC obtained from the TCSC from DP small-signal model and PSCAD at $\alpha = 63^0$

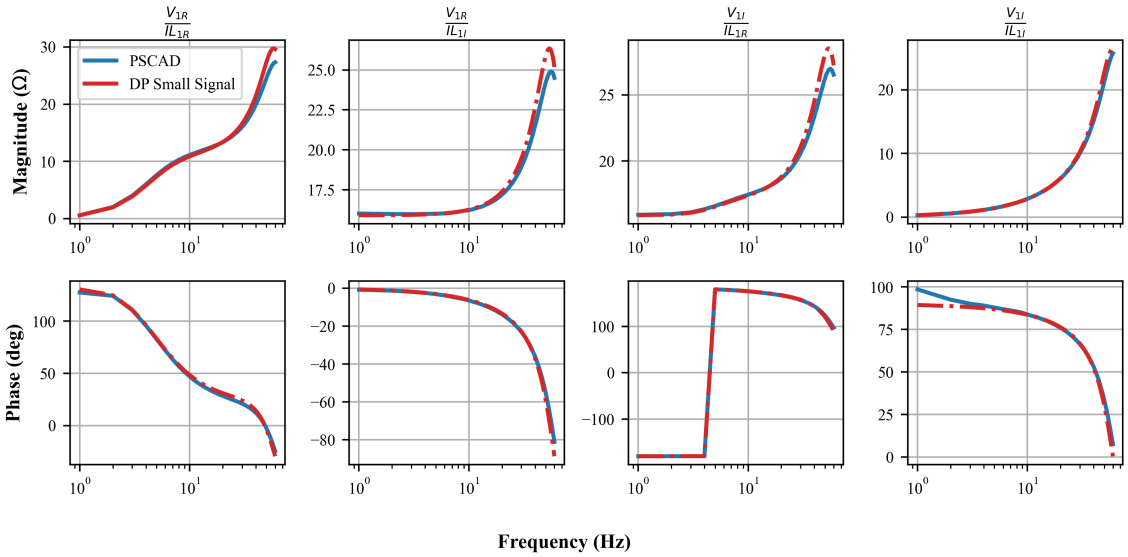


Figure 3.11: Frequency response of the TCSC obtained from DP small-signal model and PSCAD at $\alpha = 73^0$

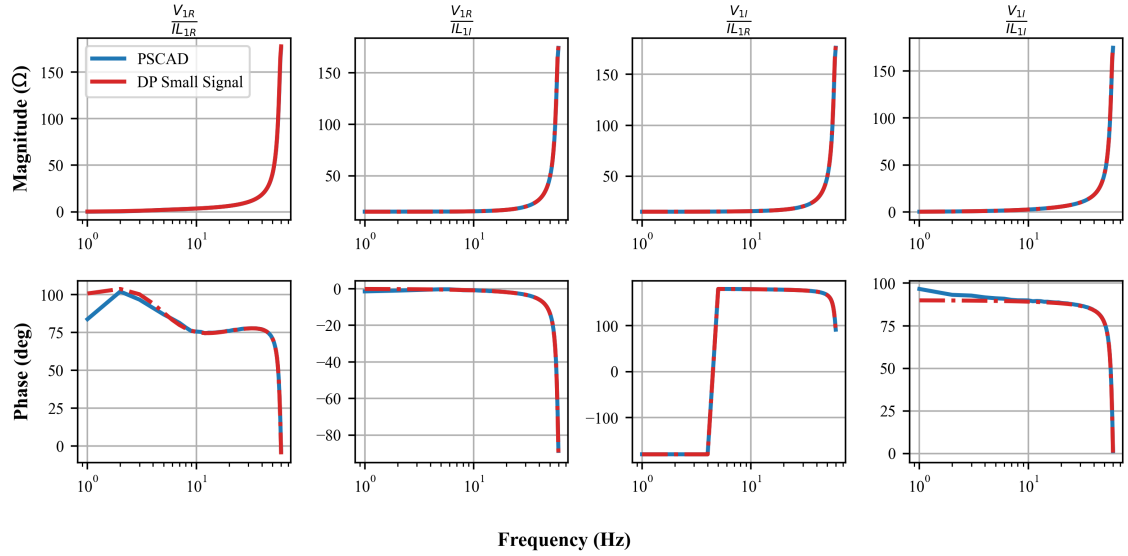


Figure 3.12: Frequency response of the TCSC obtained from DP small-signal model and PSCAD at $\alpha = 83^0$

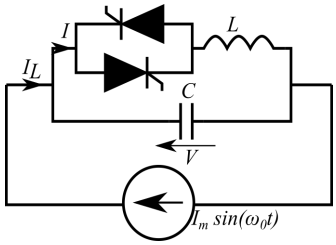


(a) TCSC with a constant current source

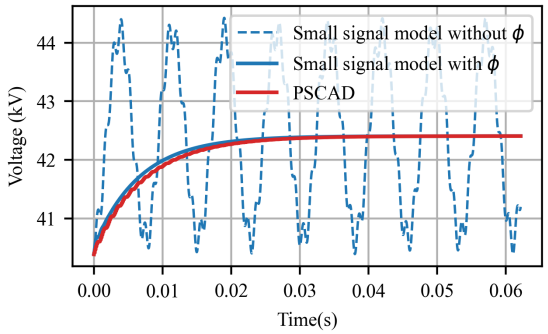


(b) Effect of modelling phase shift $'\phi'$

Figure 3.13: Effect of modelling transient phase shift

### 3.1.1 Effect of Modelling Transient Phase Shift

TCSC is a parallel combination of a fixed capacitor and a variable reactor, ideally with no resistive elements. Thus, at steady state in open loop configuration, there should be no damping offered by the parallel $L-C$ combination to any oscillation. In fact, it is a marginally stable system, and an oscillatory behaviour is expected. With relevance to that, the following test is conducted to identify the effect of modelling the phase shift '$\phi$' in the DP model of the TCSC. Consider the same TCSC in the previous test system supplied with a constant current source as in Fig. 3.13a. A small disturbance of 5% increment to the input current was applied and the fundamental component of TCSC voltage from EMT is compared against the small-signal model with and without modelling the angle '$\phi$'. The responses are shown in Figure 3.13b.

When angle '$\phi$' is ignored, an oscillatory behaviour is observed as expected since there is no resistive component modelled. The importance of modelling the phase shift further supports the argument that the source of inherent resistive damping is represented in the dynamic phasor model through the phase shift between opposite polarity peaks of the line current and TCR current, which adds damping to the circuit.

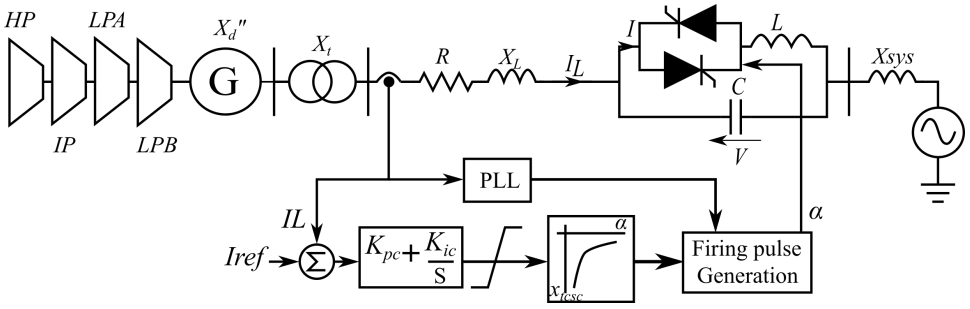


Figure 3.14: IEEE 1st benchmark for SSR studies

## 3.2 IEEE First Benchmark Model

The IEEE 1st benchmark for SSR studies [62] was adapted as illustrated in Fig .3.14 to evaluate the impact of TCSC on damping TIs and IGE. The generator operates at 1 pu terminal voltage, 0.9 pu active power, and a power factor of 0.9 at the terminal. The generator is modelled with four turbine masses with the exciter mass ignored due to its low inertia. Mechanical damping of the turbine masses is disregarded to obtain the worst-case scenario, meaning any damping of mechanical oscillations purely originates from electrical damping. The linearized model of the system is validated against EMT simulations at different steps.

Fig. 3.15 shows the comparison of time-domain responses of the linearized model against EMT simulations when a series compensation level of 66% is achieved fully with a FSC. A small disturbance of 5% increment to the generator excitation voltage was applied for a brief period of 100ms. The traces of generator speed deviation and the generator terminal RMS current are shown. The results shows damped electromechanical oscillation but a growing oscillation of 16 Hz which corresponds to one of the torsional frequencies of the CTG. A series compensation of 66% results in a network resonant frequency of 20 Hz according to (1.7). This clearly demonstrates

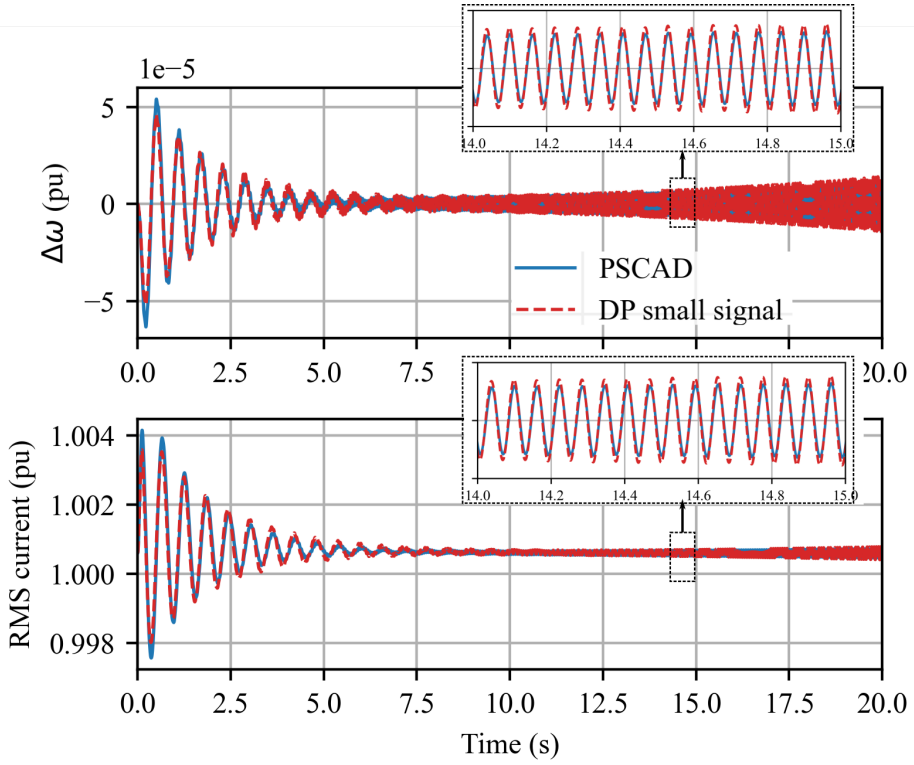


Figure 3.15: Responses of the IEEE 1st benchmark model for SSR studies with a FSC providing a series compensation level of 66%

Table 3.3: TCSC Parameters

| **Parameter** | **Value** |
|---|---|
| $L$ | 42.7 mH |
| $C$ | 26.37 $\mu$F |
| $\alpha$ | 68.8 degrees |
| $K_{pPLL}$ | 25 |
| $K_{iPLL}$ | 900 |

the phenomena of TIs caused due to the presence of a network resonance close to one of the torsional frequencies of turbine masses. As observed in Fig. 3.15, the responses of the linearized model matches well with EMT simulations.

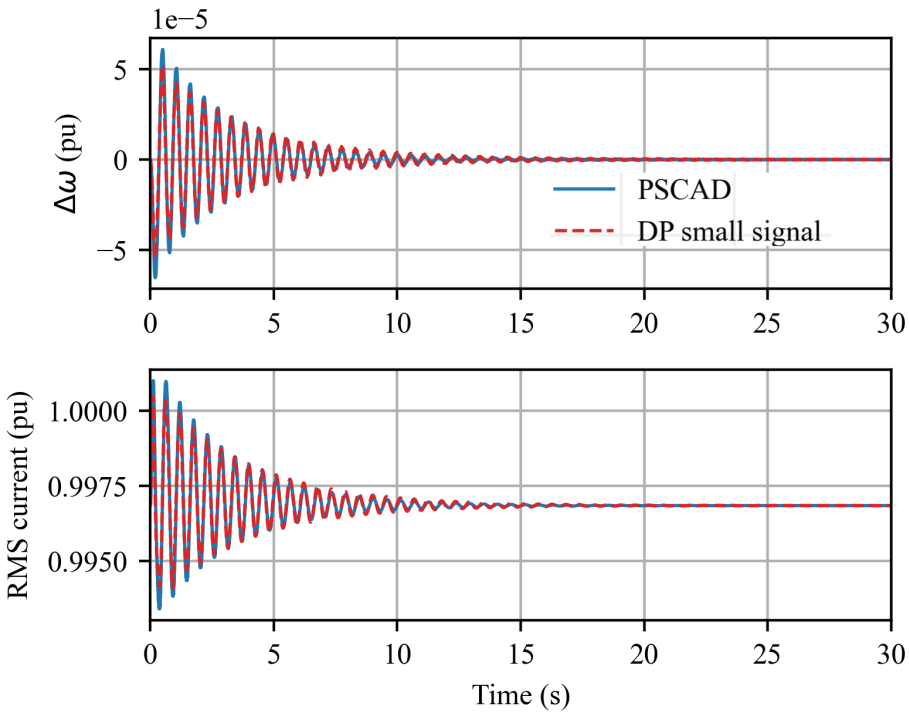


Figure 3.16: Responses of the IEEE 1st benchmark model for SSR studies with a TCSC providing a series compensation level of 66% at constant firing angle control

Next, the FSC is fully replaced with a TCSC and operated in constant firing angle control to produce the same level of compensation (66%). The TCSC parameters are given in Table 3.3. The traces are shown in Fig. 3.16 for the same small disturbance. It can be seen that the the responses of the linearized model align closely with the EMT simulations, accurately capturing the low-frequency electromechanical dynamics. However, the SSO are well damped in this scenario.

The level of series compensation is slightly lowered to 62% by increasing the firing angle of the TCSC from $68.8^0$ to $71.3^0$ and the traces are shown in Fig. 3.17. At this operating point, growing SSO with a frequency of 16 Hz is observed in generator speed deviations due to TIs. Note that undamped SSOs are not observed in the generator

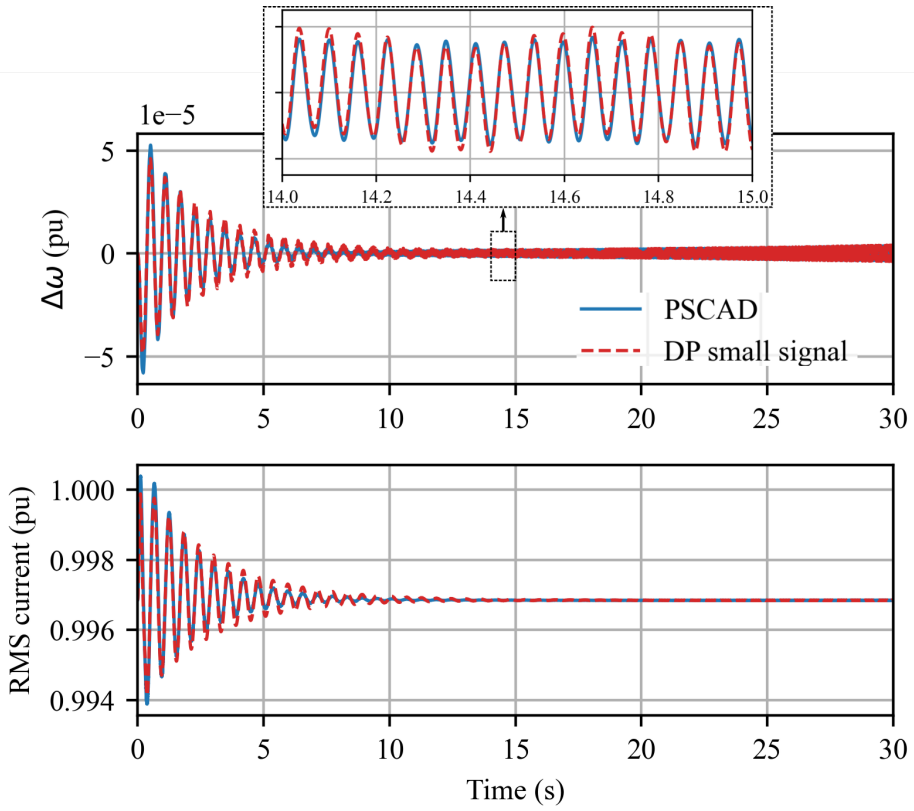


Figure 3.17: Responses of the IEEE 1st benchmark model for SSR studies with a TCSC providing a series compensation level of 62% at constant firing angle control

output current at this operating point. The linearized model effectively captures the growing oscillation in the sub-synchronous frequency range.

The TCSC is then equipped with a closed loop current control scheme to maintain a series compensation level of 66%. The controller proportional and integral gains were set at 5 and 150 respectively. The traces are shown in Fig. 3.18 following a small disturbance to the generator excitation voltage.

Figure 3.19 shows the system's response to a small disturbance, where the reference current of the TCSC current controller is increased by 5% for a duration of 100ms. Firgure also shows the deviation in firing angle of the TCSC which is now a state

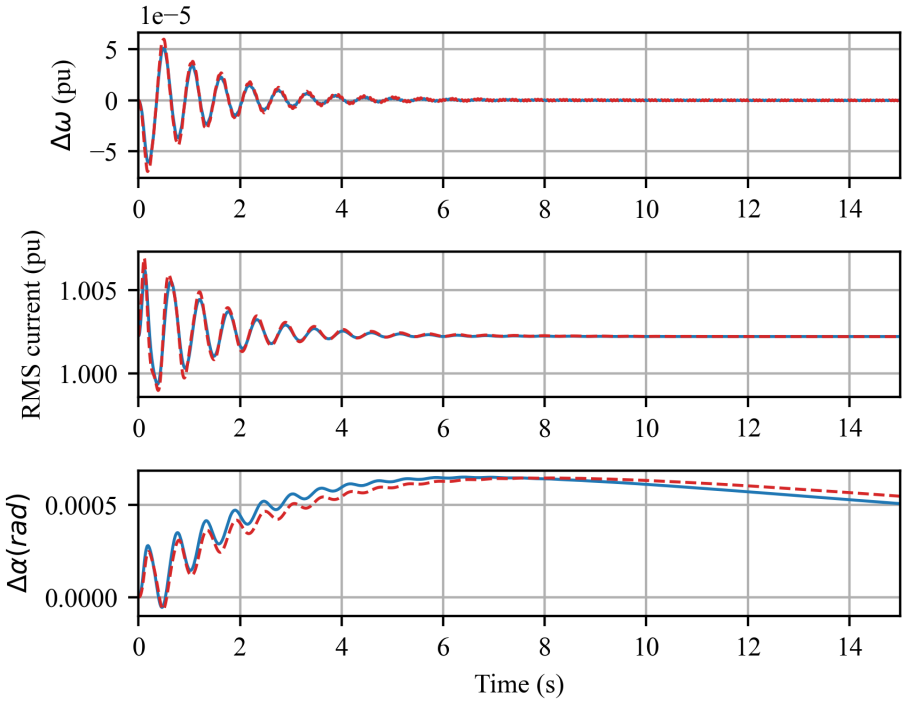


Figure 3.18: Responses of the IEEE 1st benchmark model for SSR studies with a TCSC providing a series compensation level of 66% at constant current control, following a small disturbance to the excitation voltage

variable. Unlike in Fig. 3.18, some low damped oscillations in the sub-synchronous frequency range is excited and observed in the generator speed deviation. TCSC reduces its firing angle to increase the current flow during the disturbance, increasing its capacitive impedance and hence the compensation level. Figures 3.18 and 3.19 shows a good match between the linearized model and EMT simulations

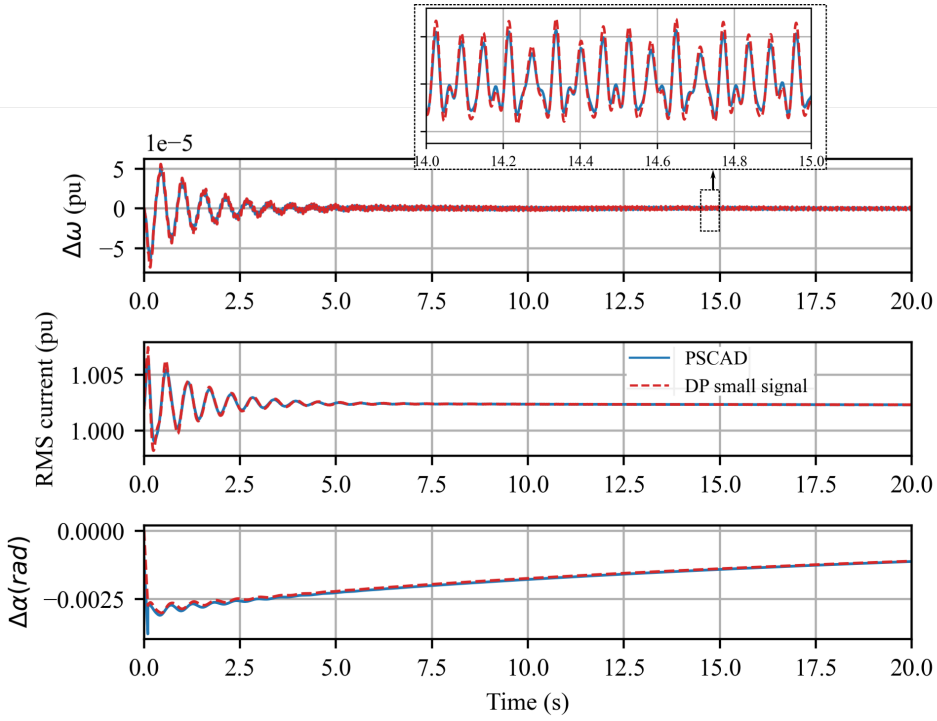


Figure 3.19: Responses of the IEEE 1st benchmark model for SSR studies with a TCSC providing a series compensation level of 66% at constant current control, following a small disturbance to the TCSC current reference

## 3.3 Wind Power Plant Test System

To investigate the capability of TCSC in damping W-SSCI, a simple test system of a Type-3 WPP connected to a strong system via a series compensated transmission line given in [20], which demonstrates the W-SSCI phenomena, was adopted. As most WPP are located in remote locations, power from WPP are brought in through series compensate lines. The test system consist of a 200MW WPP, representing one hundred of 2MW wind turbines aggregated, connected to a high voltage transmission system though a medium voltage collector system. The transmission line is 50% series compensated and is fully achieved with a TCSC operating in constant firing angle control. The test system is shown in Fig. 3.20. The DFIG is operated to inject 0.2pu

reactive power to the system while the GSC operates at unity power factor and the initial initial wind speed is 12m/s. The WPP parameters is given in Appendix C.

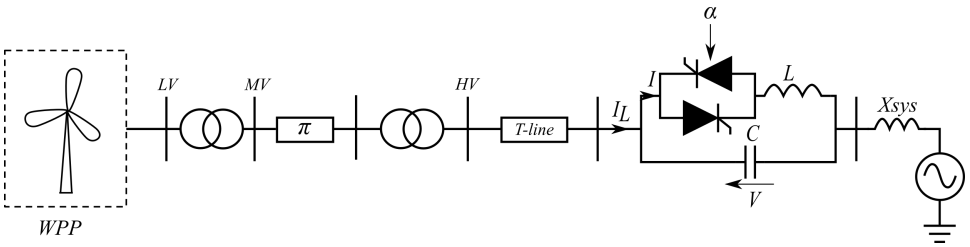


Figure 3.20: Test system of a Type-3 WPP connected to a strong system via a series compensated transmission line

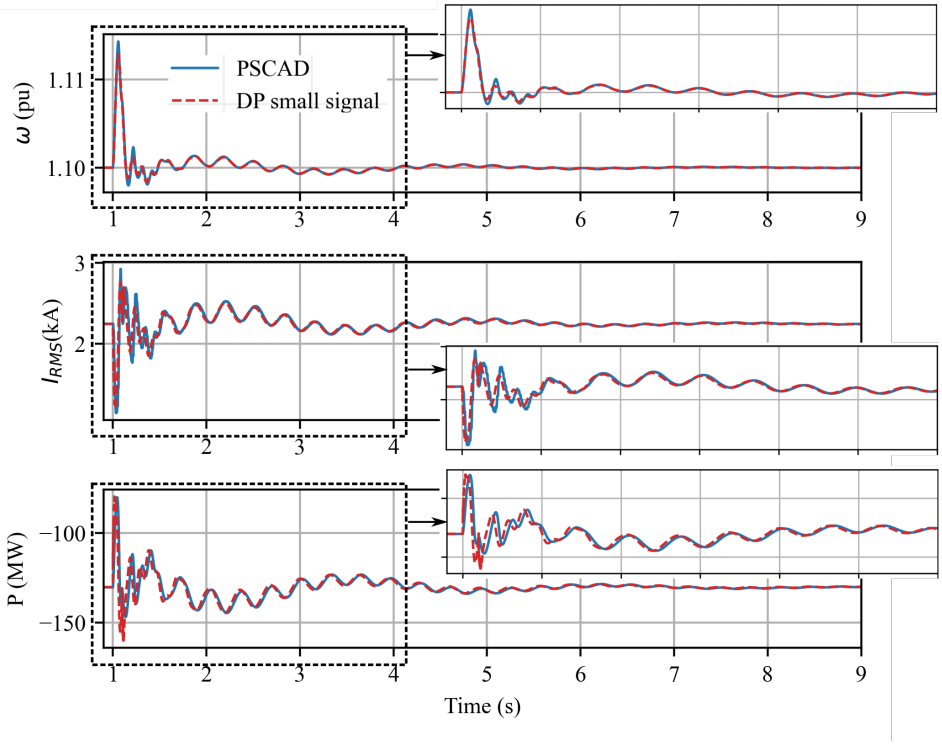


Figure 3.21: Responses of the Type-3 WPP test system, series compensated with a TCSC, following a small disturbance to the wind speed

Figure 3.21 shows a comparison of time-domain responses obtained from the linearized model of the above system, against EMT simulations. A small disturbance of

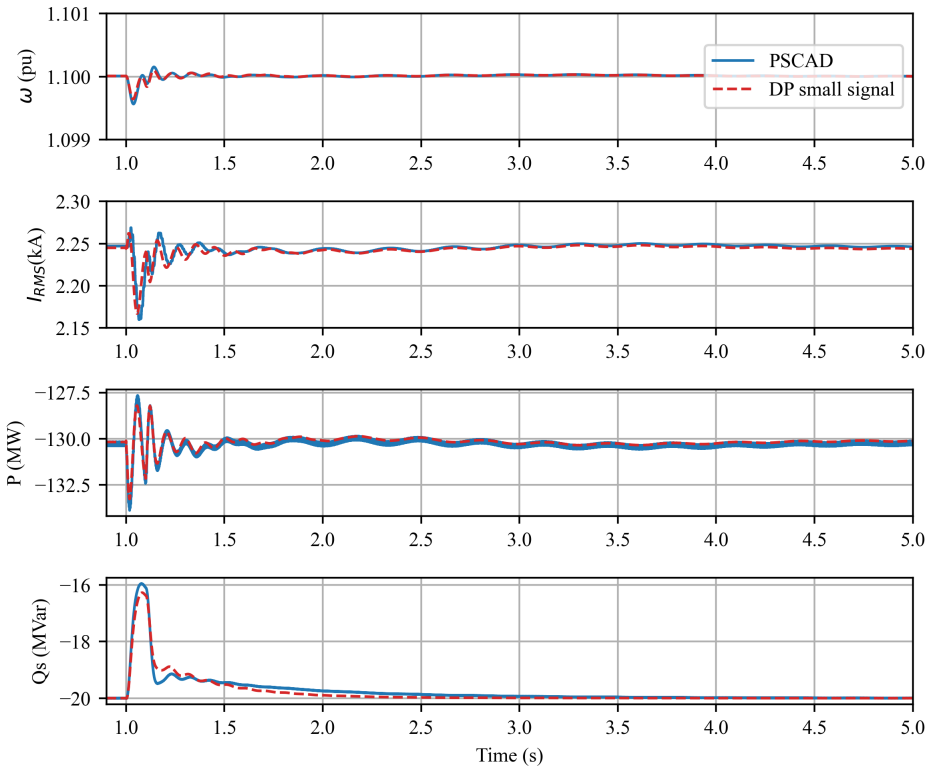


Figure 3.22: Responses of the Type-3 WPP test system, series compensated with a TCSC, following a small disturbance to the RSC stator reactive power reference

1% increment to the wind speed for 100ms is applied. The rotor speed, RMS current and the active power of the WPP is shown.

The reactive power output from the DFIG is controlled through the RSC. A small disturbance of 5% decrement to the reactive power reference of the RSC is applied for 100ms and the responses are shown in Fig. 3.22. The comparisons in time-domain demonstrated a good match between the linearized model and EMT simulations.

## 3.4 Conclusions

The validation of linearized models of power system components for analyzing SSR phenomena is presented in this chapter. When the higher-order DP model of the TCSC is linearized for small signal stability analysis, the model exhibited instability when operating close to its resonant region, due to the dynamics of the higher-order harmonics, even when the EMT simulations were stable. This instability arises because the higher-order dynamics of the rest of the system are not included in the linearized model, even though they are modelled in the linearized model of the device. This is further evident as the EMT simulations are stable. The higher-order model becomes unusable at lower firing angles due to the misrepresentation of dynamics in the higher-order terms when it is combined with a system modelled using only its fundamental components. Furthermore, it was found through small signal stability assessment that higher-order harmonic terms do not have significant contributions to sub-synchronous modes or inherent damping characteristics of the TCSC in sub-synchronous frequencies. Hence, a simplified linearized DP model of the TCSC is proposed for SSR studies.

The frequency responses of the simplified DP linearized model closely matched those of the EMT model in the sub-synchronous frequency range, justifying the simplification. Furthermore, the time responses of the simplified-linearized model of the TCSC aligned well with EMT simulations. It is shown that the non-linearity in thyristor switching behaviour (which is modelled as a transient phase shift between the opposite polarity peaks of the line current and thyristor current in the DP model) appears as a dynamic resistance and contributes to the inherent damping nature of the TCSC. It was found that modelling of this transient phase shift associated with

fundamental components is crucial to capture accurate damping characteristics of the model.

The linearized model of the IEEE 1$^{st}$ benchmark model clearly showed TI phenomena caused due to the FSC. Replacing the FSC with a TCSC resolved TI even in the absence of additional damping controllers. The linearized model showed a good agreement with the EMT simulations. An unstable TI scenario was also observed with the TCSC when the TCSC was operated at a higher firing angle (reduced compensation), and the time responses of this scenario matched with EMT simulations, indicating accurate representation of inherent characteristics important for SSR, in the simplified DP model of the TCSC. Finally, a Type-3 WPP connected to the system through a transmission line compensated with a TCSC was validated against EMT simulations.

# Chapter 4

# Evaluation of Inherent Damping Introduced by Thyristor Controlled Series Compensators

In Chapter 3, it was clear from the model validation results, that replacing the FSC with a TCSC operating in open loop (i.e. fixed firing angle control) eliminated TIs in the IEEE 1$^{st}$ benchmark system. Moreover, the TCSC exhibits a resistive characteristic that could potentially enhance damping in the sub-synchronous frequency range. This chapter presents an evaluation of this inherent SSR damping capability of the TCSC using the linearized models developed in Chapter 2. The capability of the TCSC in improving or avoiding SSR problems is evaluated under three SSR phenomena.

1. Induction Generator Effect (IGE)

2. Torsional Interactions (TIs)

3. Wind Sub-Synchronous Controller Interactions (W-SSCIs)

The IEEE 1st benchmark system in Fig. 3.14 is used to analyse the IGE and TIs whereas the WPP test system in Fig. 3.20 is used to analyse W-SSCIs through small-signal stability assessment.

## 4.1 Parameter Selection of the TCSC

Performance of the TCSC in a network is mainly governed by three parameters which can also be considered when sizing a TCSC. They are listed below and are described by (4.1), (4.2), and (4.3) respectively.

- The level of controllable series compensation ($X_{TCSC}$)
- Boost Factor ($K_b$)
- Characteristic Factor ($\lambda$)

$$X_{FSC} + X_{TCSC} = X_{TOT} \tag{4.1}$$

$$K_b = \frac{X_{TCSC}}{X_C} \tag{4.2}$$

$$\lambda = \frac{\omega_N}{\omega_s} = \sqrt{\frac{X_C}{X_L}} \tag{4.3}$$

Once the total series compensation of a transmission line, denoted as $X_{TOT}$ is known, the amount of FSC out of it is the $X_{FSC}$ and the portion of controllable series compensation is the $X_{TCSC}$. The amount of controllable series compensation or TCSC to be installed depends on various factors such as, the purpose of installation (e.g., SSR mitigation , enhanced power flow control or system stability requirements) and cost considerations.

The reactance of the inductance $L$ and fixed capacitor $C$ of the TCSC at the synchronous frequency are $X_L$ and $X_C$ respectively. The parallel resonant frequency of the TCSC is given by $\omega_N$ in (4.3) which is $\sqrt{\frac{1}{LC}}$ and $\omega_s$ is the synchronous frequency.

Once the percentage of TCSC is decided, values of $L$ and $C$ can be determined using (4.2) and (4.3), with proper choice of $K_b$ and $\lambda$. The boost factor $K_b$ indicates the extent to which the capacitive reactance of the TCSC is enhanced compared to its fixed capacitive reactance. It is typically chosen to be less than 3 to avoid operation near the resonant region in the impedance characteristic vs. firing angle curve [63]. The characteristic factor $\lambda$ is a measure of the parallel resonant frequency of the TCSC with respect to the synchronous frequency. Typical values of $\lambda$ are in the range from 2 to 4 to avoid multiple resonant points along the impedance characteristic vs. firing angle curve of the TCSC.

An example calculation of the design of the TCSC for the IEEE 1$^{\text{st}}$ benchmark system corresponding to a series compensation level of 45%, achieved fully with a TCSC is shown below. The design is carried out assuming a boost factor $K_b$ of 1.3 and a characteristic factor $\lambda$ of 2.5. A boost factor of 1.3 falls within the typical range of 1 to 3, and a value close to 1 is selected to enable high operational boost factors up to 3.

$$X_{FSC} = 0$$

$$X_{TCSC} = X_{TOT} = 82.123\Omega$$

$$K_b = 1.3 = \frac{82.123}{X_C}$$

$$C = 41.2\mu F$$

$$\lambda = 2.5 = \sqrt{\frac{63.17}{X_L}}$$

$$L = 26.8mH$$

The impact of these parameters on the inherent damping capability of the TCSC are explored through small-signal stability analysis, validated with EMT simulation in a subsequent section of this chapter. The rating or the capacity of the TCSC is a major factor which governs the cost of the TCSC. In situations where the primary objective of TCSC installation is for SSR mitigation, these assessments will prove valuable during the design and planning phases to determine the right amount of TCSC and its parameters.

## 4.2 Inherent Damping of the TCSC to Mitigate Induction Generator Effect

The adopted IEEE 1$^{st}$ benchmark system in Fig. 3.14 is used to demonstrate the effect of inherent damping capability of the TCSC on IGE. IGE is clearly observable when there is no electrical damping from the network elements. Thus, the resistance $R$ in the transmission line is assumed to be zero for the analysis. Furthermore, the exciter dynamics are ignored and the multi-mass model is disabled to avoid any

interactions with turbine masses. The effect of adding the TCSC is evaluated in contrast to having an FSC of the same capacitive reactance at different compensation levels. The TCSC is operated in open loop configuration with a fixed firing angle to demonstrate its inherent damping nature.

First, the TCSC is designed according to (4.1), (4.2), and (4.3) by assuming a nominal series compensation level of $X_{TOT} = 45\%$, where the entire compensation is achieved with a TCSC ($X_{TOT} = X_{TCSC}$). The TCSC inductance and the fixed capacitance is chosen such that it provides the nominal series compensation level at a design boost factor of 1.3 with a characteristic factor of 2.5. The level of series compensation is varied from 34.5% to 110 % first with an FSC and then with a TCSC by changing its firing angle (which effectively changes its operational boost factor). The minimum compensation level of 34.5% is achieved when the firing angle of the TCSC is at $90^0$ (blocked thyristor mode), i.e. the operational boost factor is '1' and the TCSC behaves as an FSC. A compensation level as high as 110% was considered to analyze the full range of operation of the TCSC in the capacitive vernier mode and it accounts for a part of the generator transformer impedance as well. Small-signal stability of the system is evaluated at each compensation level for both scenarios (with an FSC and a TCSC).

Variation in the frequency and damping of the network mode with the level of compensation is shown in Fig. 4.1. Note that the network mode frequencies are expressed in rotor reference frame (complement to 60 Hz). The network mode is negatively damped at all times with an FSC in the network, and the damping further reduces with increasing levels of series compensation. This is a result of the negative resistance originating from the synchronous generator rotor to sub-synchronous currents,

leading to the IGE.

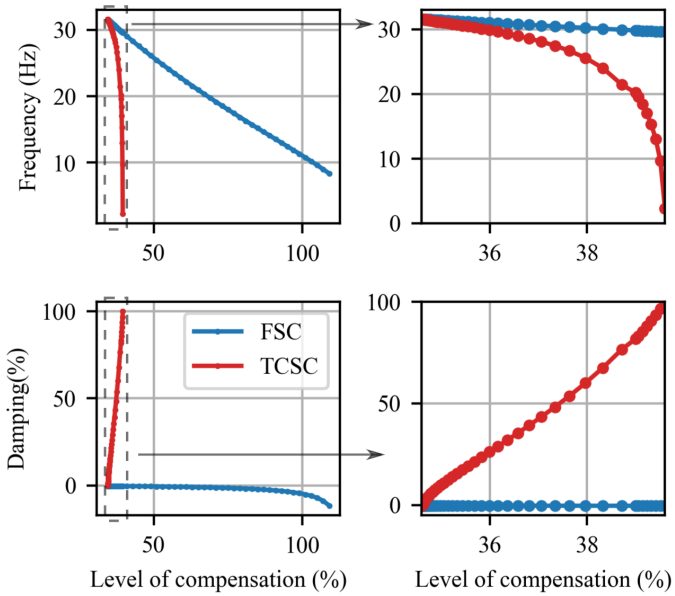


Figure 4.1: Frequency and damping of the network mode Vs. level of compensation: IGE

Using a TCSC instead of an FSC showed a good improvement in the network mode damping. When the operational boost factor of the TCSC is 1 (Firing angle = $90^0$), the behaviour is very close to that of the FSC. As the operational boost factor is increased, the compensation level increases and the network mode appears in a very narrow range of compensation levels from 34.6% to 39.6%, beyond which it disappears due to the inductive nature of the TCSC at sub-synchronous frequencies. Elimination of the network resonance at high operational boost factors, removes the root cause of the IGE. Plots to the right in Fig. 4.1 are the zoomed regions in which the network mode exist when a TCSC is used. Within the range of 34.6% to 39.6%, it is seen that the network resonant frequency changes drastically compared to that of an FSC. More importantly, the network mode is well damped compared to that of the FSC and the damping improves rapidly to 100% at 39.5% compensation. This is

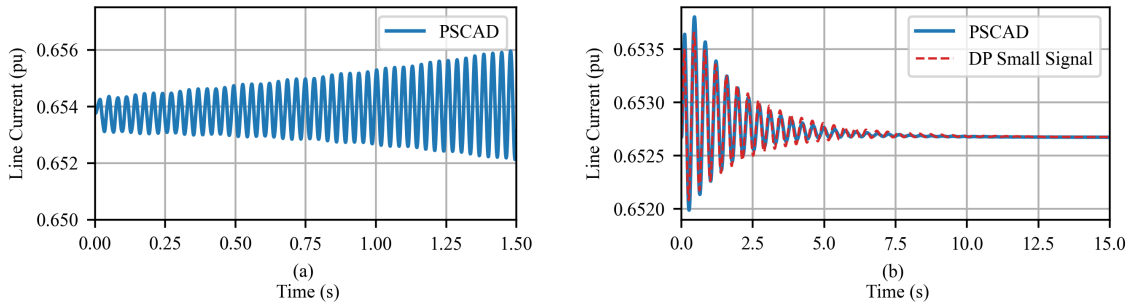


Figure 4.2: Comparison of line current responses under IGE at 35% series compensation (a) With an FSC, (b) With a TCSC

purely due to the resistance exhibited by the TCSC at sub-synchronous frequencies. Thus, it can be claimed that the inherent inductive-resistive nature of the TCSC at sub-synchronous frequencies eliminates the IGE without the need for additional damping controllers.

Figure 4.2 shows time-domain responses of the line current obtained from the linearized model and EMT simulations following a small disturbance of 5% increment to the generator excitation voltage for 100ms. Note that the unstable network mode of frequency 31.4 Hz is observed with an FSC in the circuit. This mode is well damped in Fig. 4.2 (b), when there is a TCSC, confirming the results of small-signal stability analysis.

## 4.3 Inherent Damping of the TCSC to Mitigate Torsional Interactions

To investigate the effect of TCSC on TIs, the line resistance is accounted, and the multi-mass models is enabled. Mechanical damping of all masses are ignored to

obtain the worst case scenario and the exciter dynamics are ignored. The effect of adding the TCSC on torsional modes of the CTG, is evaluated in contrast to having an FSC of the same capacitive reactance at different compensation levels. The TCSC is operated in open loop configuration with a fixed firing angle. The TCSC is designed similar to the case of IGE, but at a nominal compensation level of 31% with the same design boost factor of 1.3 and characteristic factor of 2.5.

The small-signal stability analysis of the IEEE $1^{st}$ benchmark system at the nominal series compensation level with an FSC reveals the modes listed in Table 4.1. Note that the 32.3 Hz torsional mode is highly unstable compared to other torsional modes due to its close proximity to the network mode at frequency 32.9 Hz, indicating TIs.

Table 4.1: Frequency(rotor frame), damping, and type of Modes in IEEE $1^{st}$ benchmark system with 31% FSC

| **Mode** | **Frequency (Hz)** | **Damping (%)** | **Type of Mode** |
|---|---|---|---|
| 1 | 47.455 | 0 | Torsional |
| 2 | 32.978 | 2.0458 | Network |
| 3 | 32.334 | -0.35689 | Torsional |
| 4 | 25.477 | -0.0062 | Torsional |
| 5 | 16.09 | -0.0056 | Torsional |
| 6 | 1.343 | 3.67 | Electro-mechanical |

Similar to the case of IGE, the series compensation level is varied from 24% to 110% first with an FSC and then with a TCSC and the small-signal stability of the system is evaluated at each compensation level.

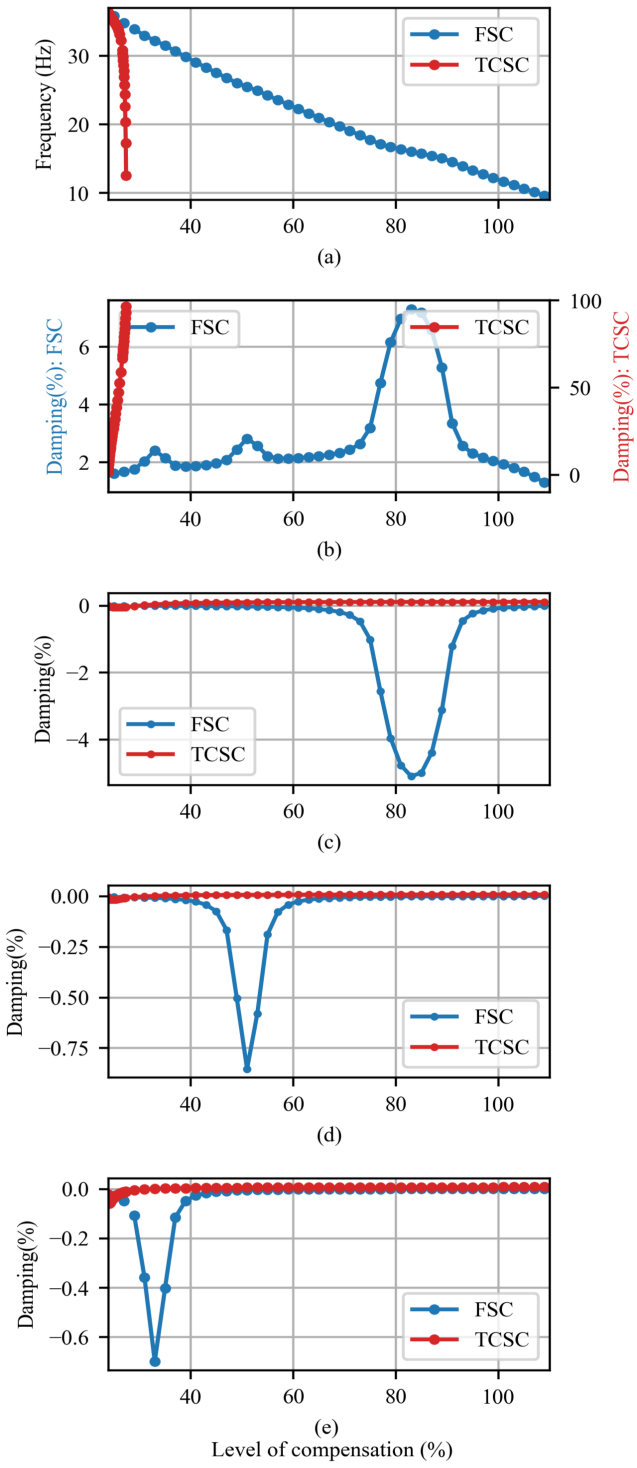


Figure 4.3: Effect of TCSC on torsional modes compared with an FSC. (a) Netwok mode frequency (b) Network mode damping (c) TM1 damping: 16.25 Hz, (d) TM2 damping: 25.43 Hz, (e) TM3 damping: 32.19 Hz

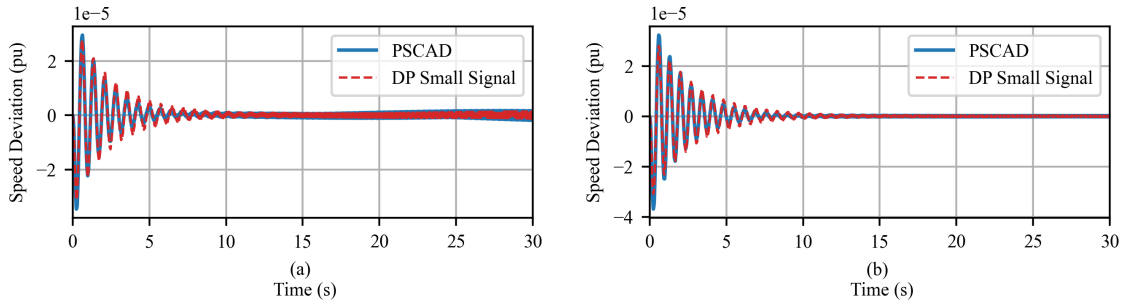


Figure 4.4: Comparison of generator speed deviation at (a)25% series compensation (Unstable), (b) 31% series compensation (Stable)with a TCSC

Figures 4.3 (a) and (b) show how the frequency and damping of the network mode changes with the level of compensation with an FSC and a TCSC. Similar to the previous case, the network mode appears in a very narrow range with a TCSC. Note that in Figs. 4.3 (c), (d), and (e), the highest negative damping of torsional modes with an FSC is achieved when the network resonant frequency is close to the torsional mode frequencies. Conversely, the damping of the network mode improves at torsional mode frequencies. Fourth torsional mode (TM4 frequency : 47.45 Hz) is neither observable nor controllable at the generator and therefore is not included in the figures. This is because 47 Hz mode only exist among the last three turbine masses along the shaft and the generator do not participate in this mode.

When the same compensation levels are achieved with a TCSC, all three torsional modes are damped above the level of 31% compensation (above the nominal series compensation level to which the TCSC was initially designed to), eliminating the risk of TI. To further validate the observations from the small-signal analysis, time-domain responses of generator speed deviations at 25% and 31% compensation are illustrated in Fig. 4.4 (a) and (b) respectively. The linearized model captures the undamped oscillations in the system quiet accurately. It should be further noted that,

the narrow range of network resonant frequencies with significantly high damping is observable with a TCSC regardless of the selected nominal compensation level. The network mode appears only when the firing angle is close to $90^0$ or the operational boost factor is close to 1.

## 4.4 Impact of TCSC Design Parameters on the Inherent Damping Capability

In the previous two cases, the TCSC was designed to provide the total series compensation level at a boost factor of 1.3 and with a characteristic factor of 2.5. It is worth to investigate how the choice of design parameters affect IGE and TIs, when operating at the nominal series compensation level it is designed to. The analysis primarily focus on the impact of boost factor and the level of TCSC. The range of characteristic factor is narrow, and high characteristic factors reduce the region for capacitive vernier operation.

Consider the previous design of TCSC for IGE study in Section 4.2. Choosing a design boost factor of 1.3, the TCSC is designed at different levels from 0% to 100%, while maintaining the total series compensation at the nominal value of 45% with an FSC. Values for $L$ and $C$ of the TCSC are chosen are chosen according to (4.1), (4.2), and (4.3), at every TCSC level with a constant $\lambda$ of 2.5. Locus of the network mode in terms of frequency and damping is illustrated in Fig. 4.5a. The network resonance exist in the full range due to the presence of the FSC. However, the network mode is well damped at all levels of TCSC, eliminating any risk of IGE. In fact, even with just 5% of TCSC, there is sufficient damping to suppress the negatively damped

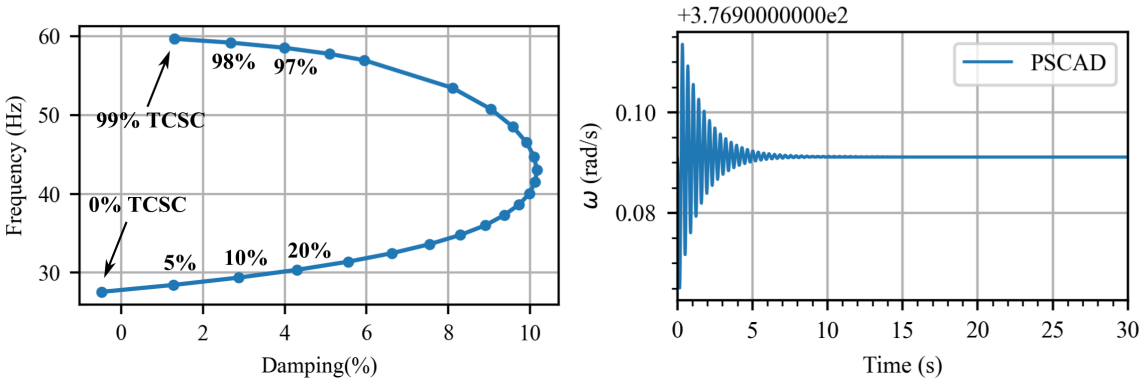


(a) (b)

Figure 4.5: Effect of TCSC level on IGE , (a) locus of the network mode, and (b) Generator speed when TCSC level = 5% :IGE

network mode observed at 100% FSC (0% TCSC). Fig. 4.19 shows the generator speed deviation from EMT simulations following a small disturbance when the TCSC corresponds to 5% of the total compensation level, which confirms the observations from small-signal stability study.

Choosing a TCSC level as low as 20% of the total series compensation level, the impact of the design boost factor on the network mode is shown in Fig. 4.6a. Within the allowed range of boost factor from 1-3, the design boost factor was changed from 1.05 to a maximum of 1.5, allowing room for TCSC operation up to $K_b$=3. It is seen that the network mode is well damped even at low boost factor. However, the damping is low at $K_b$=1.5. Hence, the full range of operation of the TCSC designed at $K_b$=1.05 and $K_b$=1.5, in the capacitive vernier region, is shown in Fig. 4.6b. It further confirms that even if the TCSC is designed at a low level, with a low or high design boost factor, the network mode is well damped in the TCSC's capacitive region of operation.

Note that when the TCSC is used along with an FSC, the network resonance exist.

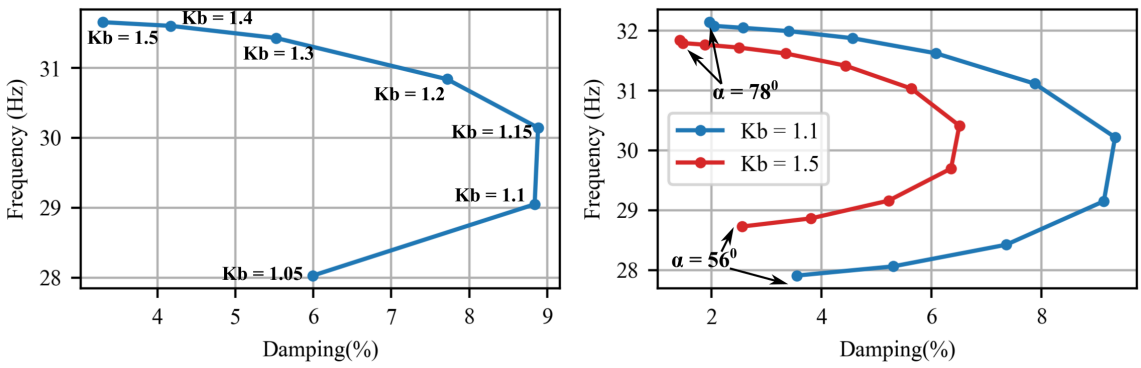


(a) (b)

Figure 4.6: Effect of Boost factor on IGE (a) locus of the network mode with increasing design boost factors, and (b) loci of the network modes in the full range of operation of the TCSC

However, the damping of the network mode is enhanced by any level of TCSC. This is due the resistance presented by the TCSC at sub-synchronous frequencies surpassing the negative resistance from the generator. Hence, the inherent damping of the TCSC is sufficient to avoid IGE, with proper TCSC design parameters. In cases where the negative resistance from the generator is very large, the TCSC can be designed with proper choice of its parameters, to offer increased damping by following a similar procedure involving small-signal stability analysis.

The impact of TCSC design parameters on TIs is investigated next. When the nominal series compensation level of 31% is fully achieved with a TCSC, the sensitivity of torsional mode damping to the boost factor is shown in Fig. 4.7. TCSC is designed at each boost factor with a constant $\lambda$ of 2.5. It is seen that better damping of torsional modes can be achieved beyond a design boost factor of 1.3, when 100% of the series compensation is achieved with a TCSC.

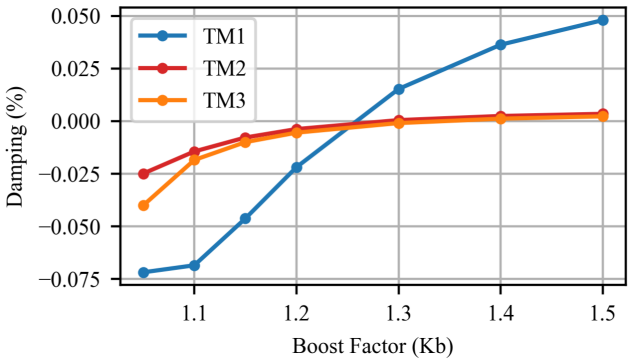


Figure 4.7: Effect of Boost factor on torsional mode damping

Thereafter, choosing a nominal boost factor of 1.3, the TCSC level is changed from 0% to 100% while maintaining the total series compensation at the nominal value of 31% with an FSC. TCSC is designed at every compensation level with a constant $\lambda$ of 2.5. Variation in torsional mode damping is shown in Fig. 4.8. High levels of TCSC improve the damping of torsional modes. Note that even 100% TCSC is barely enough to damp TM3, which is the most unstable throughout the range. It should be noted that this analysis is conducted at a worst case scenario with zero mechanical damping is which may not be the case in reality.

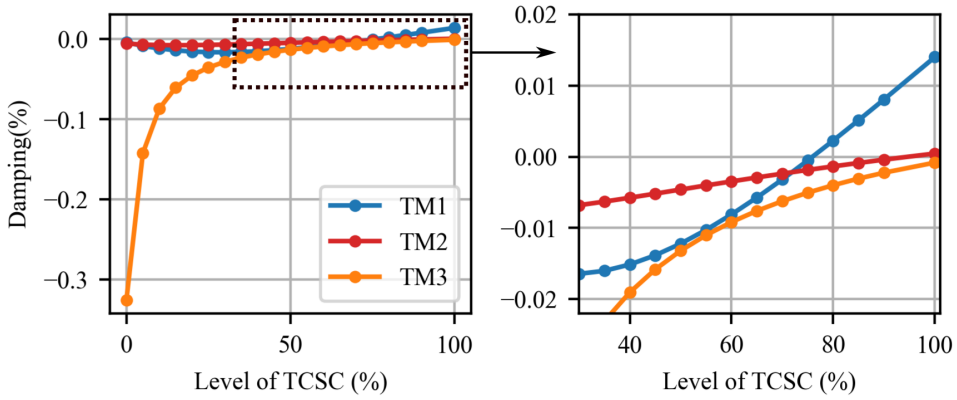


Figure 4.8: Effect of TCSC level on torsional mode damping

As seen from Fig. 4.8, TIs cannot be mitigated through inherent damping capa-

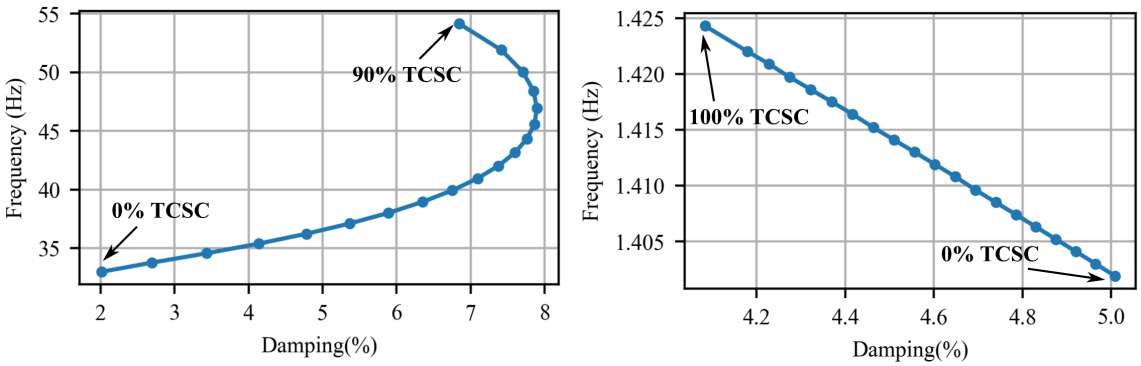


(a) (b)

Figure 4.9: Effect of TCSC level on (a)Network mode, (b) Electromechanical mode

bility of the TCSC alone if low levels of TCSC is used. However, if 100% of TCSC is used, and if the TCSC is designed at a proper boost factor, operation beyond its designed boost factor can avoid TIs through its inherent capability as shown in Fig. 4.3. This is mainly because, on top of the resistance provided by the TCSC, the network resonant mode is shifted away from torsional frequencies and eventually diminishes. Therefore, the TCSC needs to be designed to meet the required minimum series compensation level of the line, at the proper design boost factor. This helps to prevent operation below its designed boost factor. Otherwise, a minimum operational boost factor must be determined based on a similar small-signal stability analysis to prevent operation at low boost factors which may cause TIs.

Due to the presence of the network resonance at every TCSC level, torsional modes tend to become unstable. As seen from Fig. 4.9a, network mode frequency goes from 32.9 Hz to 54 Hz when the TCSC level is changed from 0% to 90% and therefore the closest to torsional mode TM3 to the network resonance is the most unstable. Note that the TM1 is damped above the level of 75%. When the network resonant frequency is shifted away from torsional frequencies due to the addition of the TCSC,

torsional mode damping improves. Hence appropriate levels if TCSC can be utilized to shift the network resonant frequency away from torsional frequencies to avoid TIs.

The sensitivity of the electromechanical mode to the level of TCSC is shown in Fig. 4.9b. It is seen that high levels of TCSC, degrades the damping of the electromechanical mode. Furthermore, high operational boost factors also degrades the damping of electromechanical mode. Therefore, when selecting a TCSC level or minimum boost factor (possibly a high boost factor) to avoid TIs through the TCSC's inherent damping, careful consideration must be paid to the stability of the electromechanical mode when the TCSC is operating in constant firing angle control.

Figure 4.10 shows responses obtained from EMT simulations under few scenarios evaluated above. With reference to the effect of boost factors, at $K_b$=1.2, growing torsional oscillations are observed in the generator speed in Fig.4.10a, aligning with the findings from small-signal stability analysis. As shown in Fig.4.8, the damping of torsional modes is negative at TCSC levels of 30% and 70%, which is reflected in the generator speed illustrated in Fig.4.10b-4.10c. However, the negative damping is reduced at the 70% TCSC level.

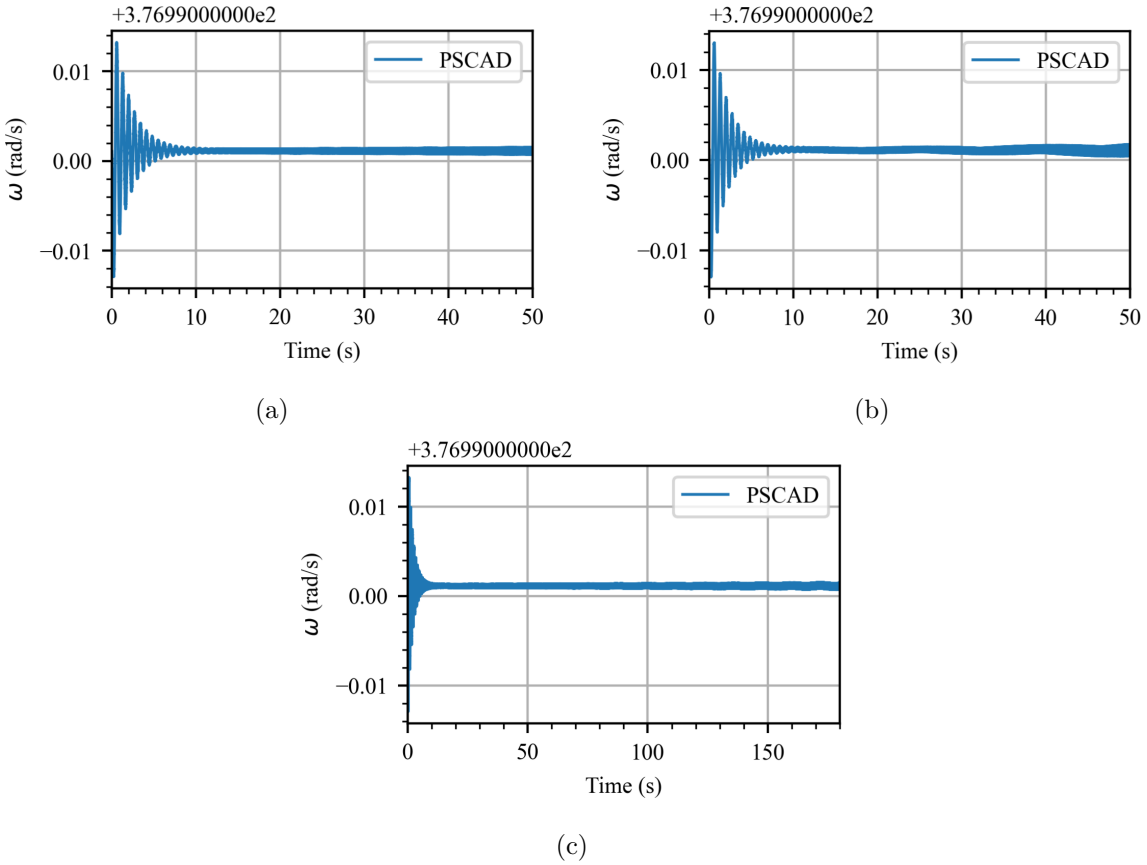


Figure 4.10: Generator speed under different TCSC design parameters. (a) TCSC designed at $K_b$ =1.2, TCSC level =100% :TIs, (b )TCSC designed at $K_b$ =1.3, TCSC level =30% :TIs, (c) TCSC designed at $K_b$ =1.3 and, TCSC level =70% :TIs

## 4.5 Effect of the TCSC Current Control

In the previous analysis, the TCSC was operated with a fixed firing angle to demonstrate its inherent damping capability in the absence of any controls. However, in practical applications, the TCSC is typically operated with a primary controller, such as power or current controllers. Therefore, the damping from these controls also contributes to the 'Inherent damping' category, as these controls are not specifically

designed to provide damping.

The effect of adding the current controller (controller parameters: $K_p$ =5, $K_i$ = 150) to the TCSC designed in Section 4.3 is illustrated in Figure 4.11. It can be seen that the effect from the current control on the damping of torsional modes is very low, as it is not designed for that purpose. As for the electro-Mechanical (EM) mode, damping has decreased when the FSC is replaced with the TCSC and operated at fixed firing angle. When the TCSC is operated in current control mode, the damping of the electromechanical mode improves even further compared to that achieved with an FSC. As shown previously, high levels of TCSC and operation at high boost factors can reduce the damping of the electromechanical mode. The current controller is advantageous in improving the damping of EM mode to achieve high levels of TCSC and boost factors in order to avoid TIs. Figure 4.12 shows time responses from EMT simulation and linearized model with and without the TCSC current controller and the responses are in good agreement.

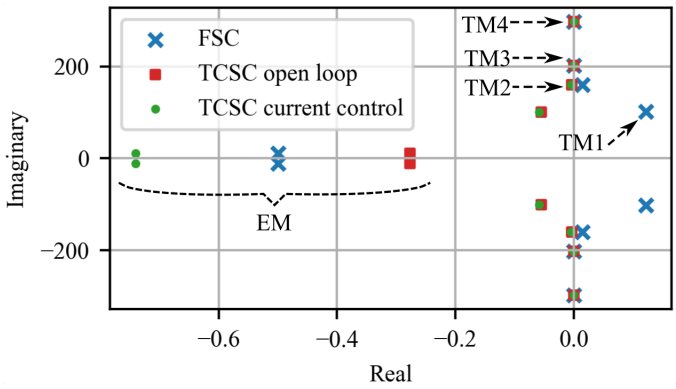


Figure 4.11: Effect of adding current controller on torsional (TM) and electro-mechanical (EM) modes

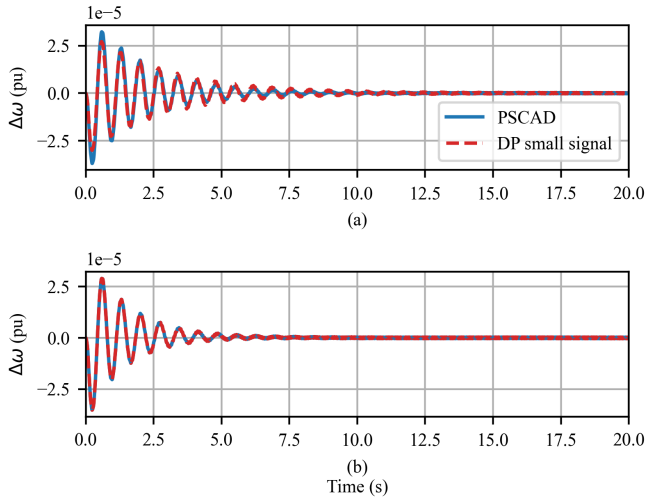


Figure 4.12: Generator speed deviation with and without the TCSC current controller

The sensitivity of the damping of the torsional and electromechanical mode to the current controller gains is shown in Fig. 4.13. The impact of varying proportional gain from 1 to 50, with a fixed integral gain at 150, is shown in the left graphs. The effect of varying integral gain from 50 to 500, with a fixed proportional gain at 5, is illustrated in the right graphs. It is noticed that the damping of the electromechanical (EM) mode is not particularly sensitive to the current controller's proportional gain but is responsive to the integral gains. Higher integral gains enhance the damping of the EM mode. Conversely, the damping of the torsional mode is somewhat more sensitive to the current controller's proportional gain than to the integral gain. Increased proportional gains improve the damping of torsional modes. However, the purpose of current controllers is not to damp torsional modes.

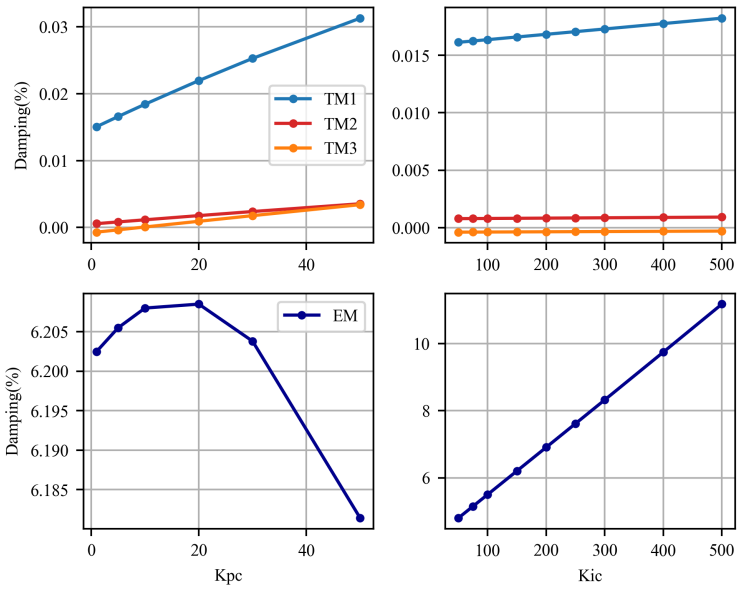


Figure 4.13: Effect of current controller proportional and integral gains on torsional and electromechanical mode damping

TCSC operation in fixed firing angle when the TCSC level corresponds to 30% was not possible due to the torsional mode instability. However, adding a current controller with a high proportional gain of 50, enables operation without TIs as shown in Fig. 4.14. Furthermore, damping of the EM mode has also improved than in Fig.4.10b.

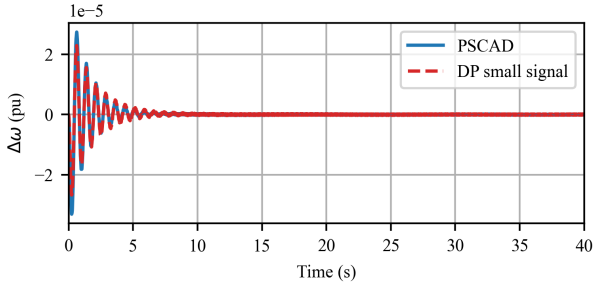


Figure 4.14: Generator speed deviation when the TCSC designed at $K_b$ =1.3, TCSC level =30% is equipped with a current controller of high proportional gain :TIs

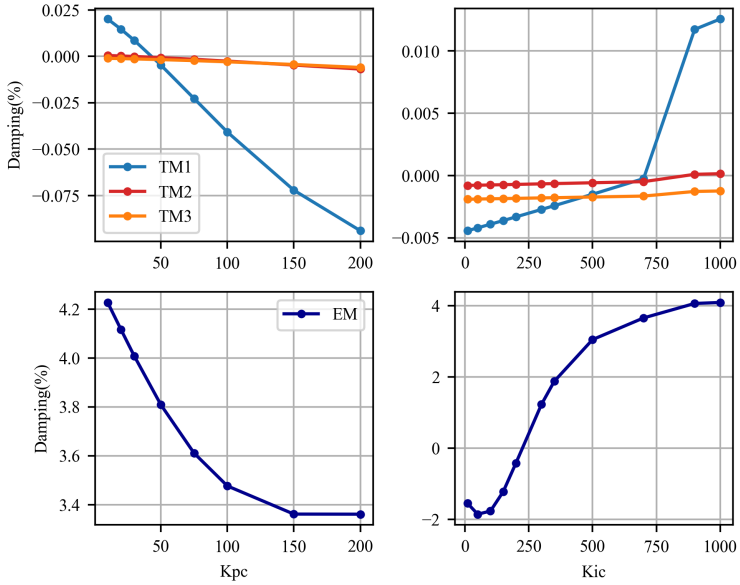


Figure 4.15: Effect of PLL proportional and integral gains on torsional and electromechanical mode damping

## 4.6 Effect of the Phase Locked Loop

The impact of proportional and integral gains of the PLL of the TCSC on torsional and electromechanical mode damping was investigated. The TCSC designed in section 4.3 is used for the analysis. The proportional gain of the PLL is varied from 10 to 200 while the integral gain is fixed at 900, and the plots are shown to the left of Fig. 4.16. It is evident that the torsional modes become unstable at high proportional gains and damping of the electromechanical mode reduces. EMT simulation results at $K_{pPLL} = 10$ and $K_{pPLL} = 200$ is presented in Fig. 4.16 which validate the conclusions drawn from the small-signal stability analysis.

The integral gain of the PLL is varied from 10 to 1000 with proportional gain being fixed at 25 and the plots are shown to the right of Fig. 4.16. Accordingly, high integral gains of the PLL have a slight positive impact on torsional mode damping.

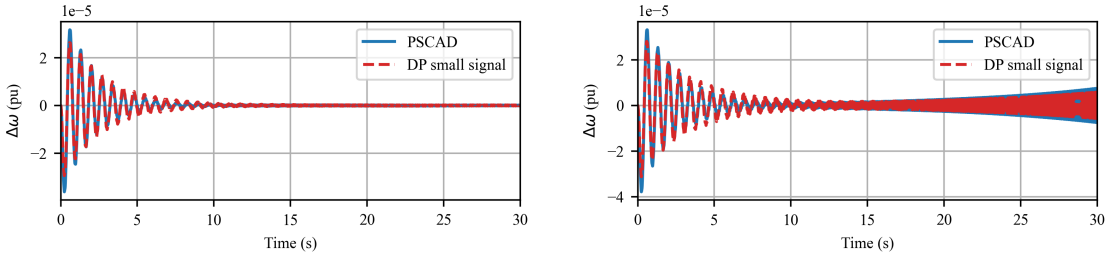


(a) (b)

Figure 4.16: Generator speed deviation when TCSC PLL proportional gain is at (a) 10 and, (b) 200

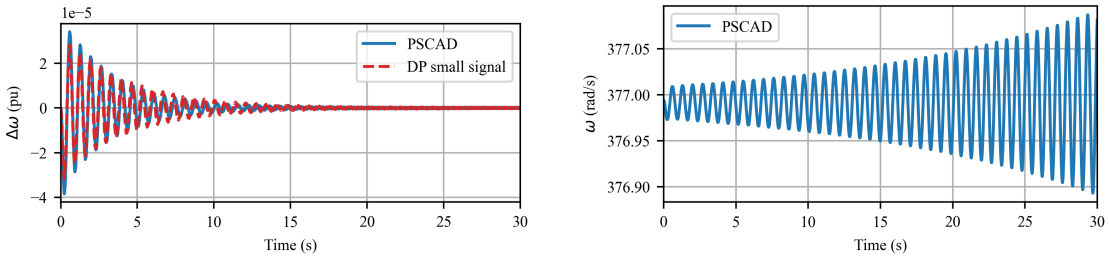


(a) (b)

Figure 4.17: Generator speed deviation when TCSC PLL integral gain is at (a) 350 and, (b) 100

Low integral gains can destabilize the electromechanical oscillations as seen from EMT simulation results in Fig. 4.17b. Therefore, low PLL proportional gains and high integral gains are appropriate for the TCSC.

## 4.7 Use of TCSCs for Mitigation of Wind Sub-Synchronous Controller Interactions

Sub-synchronous oscillations between a DFIG and series compensated lines occur at the network resonant frequency. When high-amplitude oscillations occur between a WPP and a series capacitor, the wind turbine converter and the generator are often the most susceptible components at risk of damage. As demonstrated in [20], several WPP and network parameters influence these sub-synchronous interactions.

- High RSC inner current controller loop proportional gains ($K_{pdr}$ and $K_{pqr}$) can reduce the damping of the network resonance and hence make the system unstable.
- High RSC outer loop stator reactive power controller proportional gain ($K_{pQg}$) can reduce the damping of the network resonance.
- High compensation levels reduce the network resonance frequency and damping.

In the test system in Fig.3.20, when the line is series compensated at 50% with an FSC, there exist a network resonance at 26.1 Hz (in rotor reference reference frame). This network resonance remains stable with low RSC inner current controller gains. However, with RSC current controller gains as high as 0.115, the network resonance becomes unstable, leading to W-SSCIs. Due to the adverse effects of the RSC current controller gains, the resistance presented by the WPP through its controls will become negative at certain gains. The frequency response of the Type-3 WPP as observed from its POC obtained at low and high RSC current controller gains is shown in Fig. 4.18 (frequencies are in stator reference frame). Frequency response of the WPP

is obtained through signal injection technique at its POC. It is noticed that the resistance at the network resonant frequency is positive at low gains, whereas it becomes negative at high gains. If the negative resistance from the WPP surpasses the resistance of the network at the network resonance frequency, sub-synchronous currents will grow. This phenomena is termed as W-SSCIs, which is an electrical resonance sensitive to controller gains. This phenomena is purely electrical and does not involve mechanical interactions.

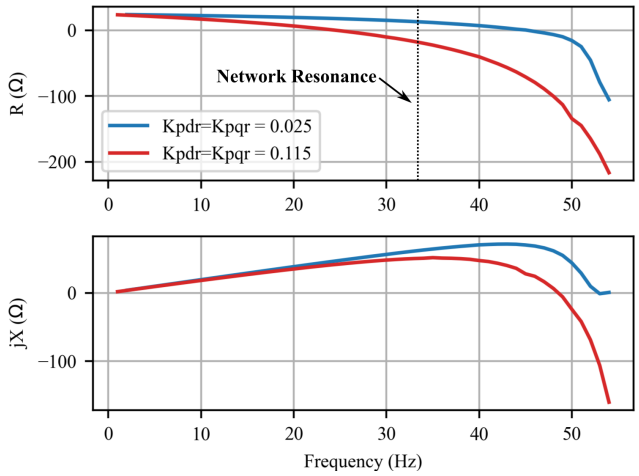


Figure 4.18: Frequency characteristics of the Type-3 WPP at low and high RSC inner current controller gains

As elaborated in the previous sections, the TCSC provides inherent damping by presenting a resistance and behaving as an inductor at sub-synchronous frequencies. Hence the TCSC can be utilized to avoid W-SSCIs which arise from the network resonance. Consider the test system in Fig.3.20, with RSC current controller gains increased to 0.115 creating an unstable electrical resonance. A TCSC is introduced to the test system at different levels designed at a boost factor of 1.3 and a characteristic factor of 2.5 and the TCSC is operated with a fixed firing angle. The sensitivity of the network mode to increasing levels of TCSC is shown in Fig. 4.19a. At 100%

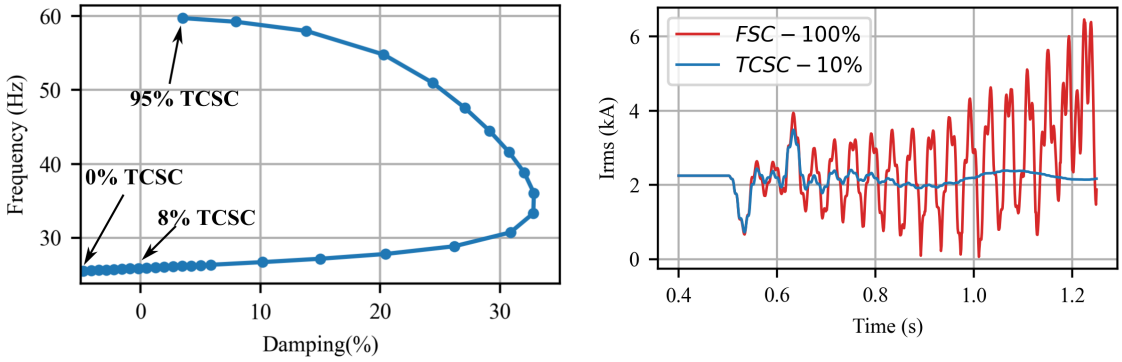


Figure 4.19: Sensitivity of the network mode to TCSC levels (a) Locus of network mode for varying levels of TCSC and, (b) EMT simulation results with a FSC and 10% TCSC : W-SSCI

FSC, the network mode is unstable, but with increasing levels of TCSC, the network resonance frequency increases and the damping improves until a TCSC level of 55%. It is evident that the inherent damping from the TCSC can avoid W-SSCIs at levels as low as 8%. The network mode is eliminated at 100% TCSC as also demonstrated in IGE case. Fig. 4.19b shows a comparison of EMT results of the generator rotor speed with 100% FSC and 10% TCSC.

Due to the presence of the network resonance when a combination of FSC and TCSC is used, just like with an FSC, the network resonance is still sensitive to RSC current controller gains ($K_{pdr}$ and $K_{pqr}$) and stator reactive power controller gain ($K_{pQg}$) as shown in Fig. 4.20. However, due to the inherent damping provided by the TCSC, high inner current controller gains and reactive power controller gains can be realized even with low TCSC levels.

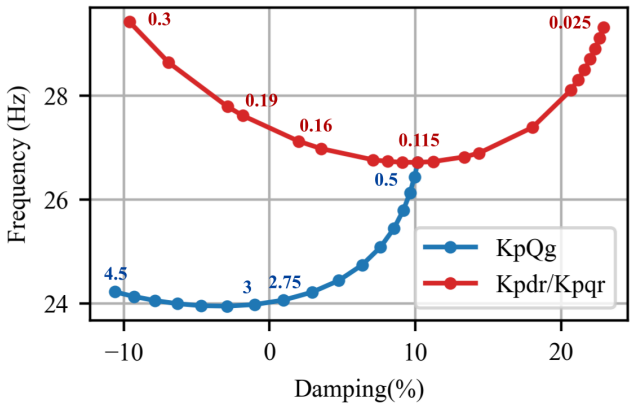


Figure 4.20: Sensitivity of the network mode to RSC current controller gains ($K_{pdr}$ and $K_{pqr}$) and stator reactive power controller gain ($K_{pQg}$) with 10% TCSC

A network parameter that can lead to W-SSCI is the total compensation level of the transmission line as shown in [20]. A high series compensation level of the transmission line can induce W-SSCIs. As shown previously, replacing the FSC completely with a TCSC will eliminate the network resonance and therefore is expected to avoid W-SSCIs even at high nominal compensation levels. However, it was observed that achieving high nominal compensation levels purely with a TCSC operating in constant firing angle control is likely to destabilize the electromechanical mode, despite the elimination of the network resonance. In Fig. 4.21a, loci of the electromechanical mode when the nominal series compensation is increased is shown by the red trace. It is seen that beyond 62%, the electromechanical mode becomes unstable. It can bee seen from the participation factors in Fig. 4.21b, that the highest participant apart from generator states, is the TCSC-TCR current. Thus, at a total compensation of 70%, decreasing the TCSC level and compensating the rest with an FSC was found to enhance the damping of the electromechanical mode, as observed from the blue trace in Fig. 4.21a. It's important to highlight that even with 70% compensation and low

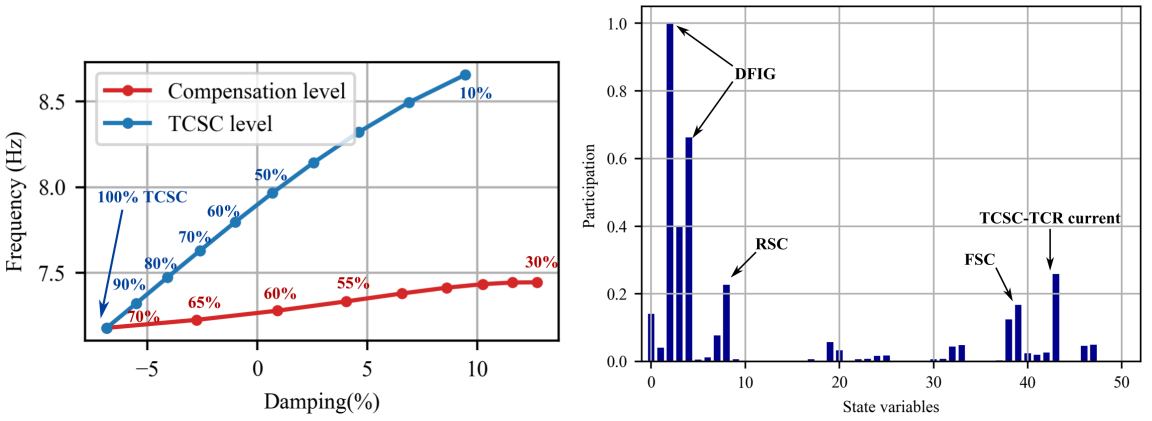


(a) (b)

Figure 4.21: Sensitivity of the the electromechanical mode to (a) Nominal series compensation level and TCSC proportion and, (b)Participation factors for the unstable electromechanical mode

TCSC levels, the network mode is adequately damped. This enables high nominal compensation levels to be achieved with a combination of FSC and TCSC without the risk of W-SSCIs.

## 4.8 Conclusions

The inherent damping capability of the TCSC at sub-synchronous frequencies is evaluated through small-signal stability assessment using a simplified DP model of the TCSC. When the series compensation is fully achieved with a TCSC, the network mode exists only when the TCSC is operated very close to the operational boost factor of 1 (one) and the results were verified using EMT simulations. The network mode appears in a very narrow range of compensation levels (or operating points) and the damping of the network mode is much higher than that of an FSC in this region. The risk of IGE and TIs is avoided due to the absence of a network resonant mode and inherent resistive nature of the TCSC at sub-synchronous frequencies. However, if

the TCSC is operated below its nominal operating point it is designed to (low boost factors), there may still be risks of TIs.

If the TCSC is used along with an FSC, the network resonance exists in the network. However, the inherent resistive nature of the TCSC can still avoid IGE when properly designed, even at very low levels of TCSC. However, mitigation of TIs with the inherent damping capability of the TCSC cannot be guaranteed when a mix of FSC and TCSC is used (at low TCSC proportions), specially when the CTG have negligible mechanical damping. This is due to the presence of a detuned network resonance and such operating conditions may need SSDCs to guarantee mitigation of TIs.

The electromechanical mode damping is degraded due to the TCSC operating in fixed firing angle control. Use of primary controllers such as current controllers improve the damping of the electromechanical mode. While the purpose of primary controllers is not to provide damping to SSR conditions, torsional mode damping is sensitive to TCSC current controller gains.

Similar to the case of IGE, W-SSCIs is also a phenomena where WPP controllers have the potential to make network resonance unstable. It is shown that the inherent damping capability of the TCSC is sufficient to avoid W-SSCI phenomena without additional damping controllers, even at low proportions of TCSC. Use of the TCSC also allows more room for previously restricted (when an FSC is used) parameters such as RSC controller gains to be controlled to get the desired performance.

Time-domain responses of the linearized models are in good agreement with EMT simulation results, thus the simplified DP small-signal model of the TCSC is recommended for SSR analysis. The model can be used to evaluate whether the inherent

damping of TCSC is sufficient to avoid SSR conditions at the planning stage, given a safety margin, following similar analysis presented in this chapter.

Although some of the above findings have been known before through observations from experimental or time-domain simulations, this work provides a comprehensive investigation using a dynamic phasor-based small signal stability analysis, which was not available in literature.

# Chapter 5

# TCSCs for Mitigation of SSR in Heavily Series Compensated Networks

In earlier chapters, the SSR phenomenon was demonstrated in a radial system, where a CTG or a WPP was connected to the grid via a single series compensated line. Identifying the problem and analyzing it was therefore straightforward. However, in practical systems, with the increasing demand for power and the need to integrate more power into the grid, multiple lines are often series compensated at various levels. In such networks, SSOs between devices and the network can occur at multiple sub-synchronous frequencies, making the analysis complex. Additionally, contingencies can result in devices being electrically close and potentially radial to series compensated transmission lines. This Chapter proposes a procedure to address SSR issues in such networks through the use of TCSCs.

## 5.1 Background

In the Finnish transmission system, between 1997 and 2016, the transmission capacity of the cross-border interconnection with Sweden and the North-South corridor in Finland was enhanced by installing 11 FSC on existing 400 kV transmission lines [64, 65]. The degree of series compensation is in between 70% to 75% [66]. At present, each transmission line passing through the Central Finland and Northern Finland cross-sections is equipped with series compensation [67]. In Finland, the risk of W-SSCIs is becoming more prominent [68], due to the growing number of planned wind generation sites located near the series-compensated network in Central and Northern Finland.

The ERCOT system has six 345kV double-circuit transmission lines with series compensation, totalling 12 circuits [69]. These enhancements were made to connect the CREZ (Competitive Renewable Energy Zones) to load centers in the Texas Interconnection. Study report [69] identified specific locations in the CREZ system where Type-3 WPPs are at a higher risk of experiencing SSOs considering system contingencies up to N-4. The report indicates that without mitigation measures, there is a significant potential for Sub-Synchronous Interactions (SSIs), particularly affecting Type-3 WPPs even in the absence of line outages. In 2010, ERCOT encountered an incident of W-SSCIs involving a Type-3 WPP connected radially to a series-compensated line following an N-1 contingency. The incident has led to tripping of the wind turbines but not before the equipment were damaged. There are six thermal plants near CREZ series compensation which may be susceptible to SSR. Line outages could result in generators being more directly coupled to the series capacitors, increasing the potential for SSR. However, detailed studies assessing the SSR risk with

thermal generators are not publicly available due to confidential information.

In networks with multiple series compensated lines, there are many SSO challenges related to the devices connected, whether it is a WPP or a CTG. Contingencies such as line outages can result in the devices being in close electrical proximity to the series compensation. In such situations, there can be many SSR modes which can cause IGE, destabilize torsional modes of multiple CTG nearby or cause W-SSCI issues. As demonstrated in previous chapters, the TCSC can be used to avoid IGE, TIs and W-SSCIs. However, in networks with multiple series compensated lines, replacing all FSCs with TCSCs may not be a viable solution for utilities due to the cost associated with TCSCs. A more practical approach would be to replace a few or a portion of an FSC with a TCSC.

Identifying the location(s) and the level of compensation from TCSC, to mitigate SSOs is a challenging task and there are no significant contributions reported in literature in this area. Hence the content of this chapter will include a procedure developed to address this problem in a systematic way. The goal is to utilize the inherent damping capability of the TCSC to avoid potential SSR conditions in such networks and to determine the necessity of additional damping controls and design when necessary. The content in this chapter will primarily focus on IGE and TIs. However, a similar procedure is applicable for wind related W-SSCI phenomena as well.

## 5.2 Use of Frequency Scans to Identify Critical FSC

The procedure to address the above mentioned problem starts with screening of the network to detect network resonances. As the primary cause of the SSR phenomena addressed in this study are network resonances excited by FSCs, identifying the network component that contributes the most to a specific network resonance at the screening stage can help reduce the need for extensive and time-consuming detailed studies. Frequency scanning is a simple preliminary screening technique used for SSR studies, which can indicate network resonant frequencies. This study demonstrates how frequency scans can be used beyond mere identification of network resonances, to identify the critical FSC responsible for electrical resonances. The goal is to extract as much information as possible from frequency scanning so that time consuming detailed studies could be avoided in the screening stage of a study.

Use of frequency scans to identify critical FSC in the network is demonstrated through an example test system with multiple series compensated lines. The test system is formed with three generators and three series compensated lines as shown in Fig. 5.1. Generator and network data data are included in the Appendix D. The two parallel transmission lines are compensated at 80% and 20% respectively to demonstrate two distinct resonant points and the remaining line from bus 7 to 8 is compensated at 70% . This network is primarily formed to demonstrate the methodology.

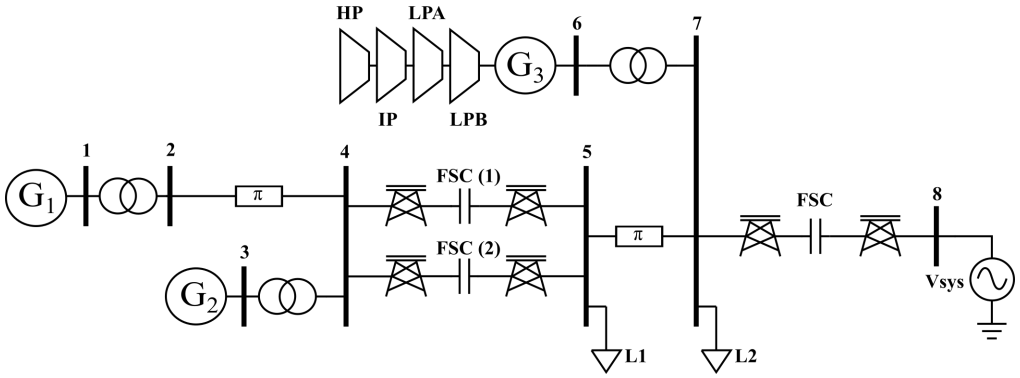


Figure 5.1: Series compensated test system 1

It is shown that frequency scanning at multiple locations and at multiple contingencies (series capacitors bypassed/in-service) can be effectively used to identify all electrical resonant points and the critical FSCs which contributes the most to the excitation of a certain electrical resonance. DP based small-signal stability was assessed in the above network to support the findings of frequency scans. Table 5.1 shows the network and torsional modes identified in the above network. Frequencies are expressed in the synchronous reference frame to enable easy comparison with the results of frequency scans.

Table 5.1: Network and torsional modes of the series compensated test system

| Mode Number | Network Modes | | Torsional Modes | |
|---|---|---|---|---|
| | Frequency (Hz) | Damping (%) | Frequency (Hz) | Damping (%) |
| 1 | 8.39 | 13.5 | 2.54 | 0 |
| 2 | 26.75 | 16.5 | 17.77 | -0.046 |
| 3 | 36.61 | 17 | 25.74 | -0.0106 |
| 4 | | | 33.834 | -0.3134 |

Figure 5.2 shows the results of the participation factor analysis. Generator participation to the 3$^{rd}$ network mode (36.61 Hz) is minimal and almost negligible as per Fig. 5.2a. According to Fig. 5.2b, the highest contributing components to that mode are the series capacitors and inductances in the two parallel lines between bus 4 and

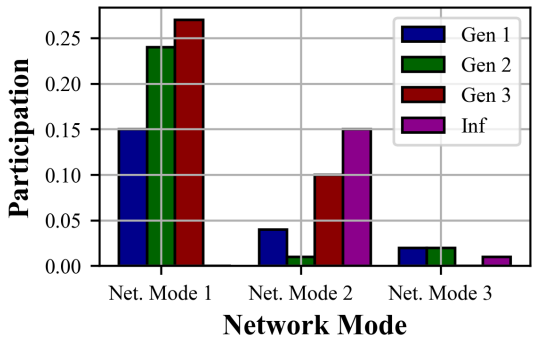


(a) Generator participation to network modes

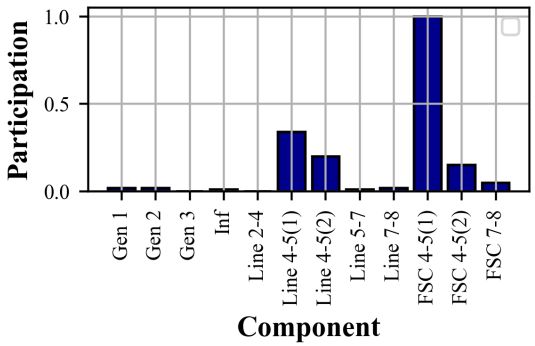


(b) Participation to intra-parallel network mode

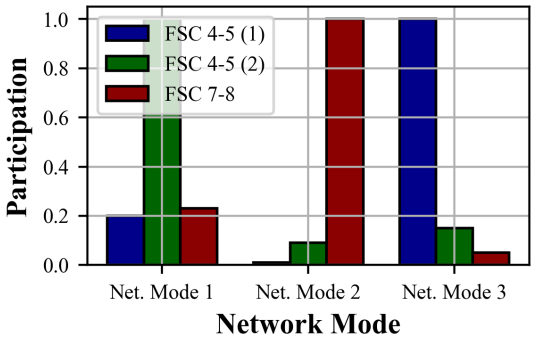


(c) FSC participation to network modes

Figure 5.2: Participation Factors

5. Thus, network mode 3 can be identified as an intra parallel line network mode.

According to the participation of FSC to network modes illustrated in Fig. 5.2c, there is always one series capacitor which dominates a certain network mode. Identification of this FSC will enable the application of appropriate countermeasures. Countermeasures includes the traditional approach of bypassing FSCs, or an advanced solution is to replace them with a TCSC.

Frequency scanning has to be performed twice, separately looking into the network and the device (including device transformer) as shown in Fig. 5.3. The frequency scans are finally combined to obtain the equivalent impedance as seen from behind

neutral point of the generator. Impedance dips in the frequency scan profile indicate network resonant points.

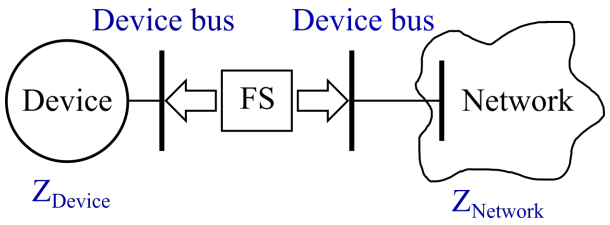


Figure 5.3: Frequency scanning at device bus

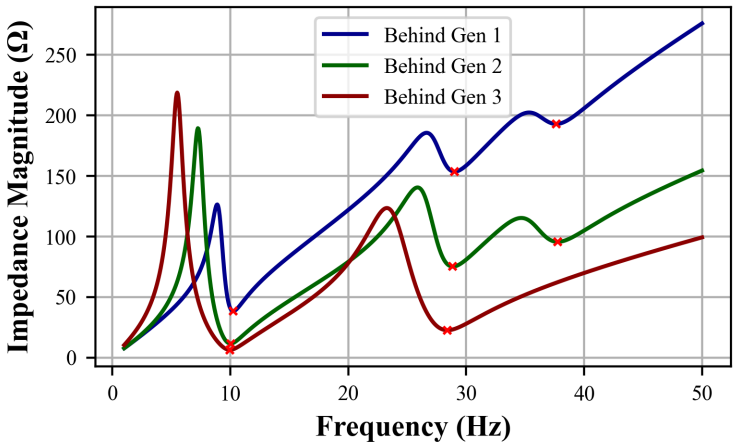


Figure 5.4: Impedance profiles when all FSCs are in service

Frequency scans were obtained behind the neutral points of every generator with all series capacitors in-service and the results are shown in Fig. 5.4. According to [70], points which have at least 5% reactance dip within 3% of the torsional frequency are likely to yield transient torque problems. This theory has found to be generally conservative. As seen from Fig. 5.4, frequency scans at a single location does not reveal all resonant points in the network, but frequency scans at multiple locations reveal all network resonant points which are identified at 10 Hz, 28 Hz and 37 Hz in the impedance profiles. The frequencies at impedance dips are close to the small-

signal stability results. Small-signal stability analysis captures all modes in a single analysis, whereas frequency scanning has to be performed at multiple locations to capture all of the network modes.

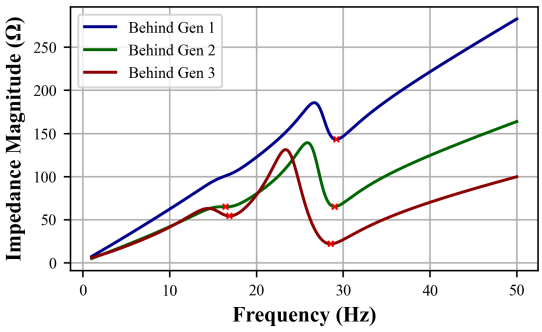


(a) Impedance profiles when FSC 4-5 (1) is bypassed

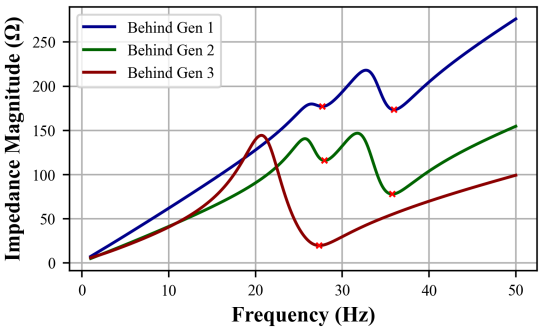


(b) Impedance profiles when FSC 4-5 (2) is bypassed

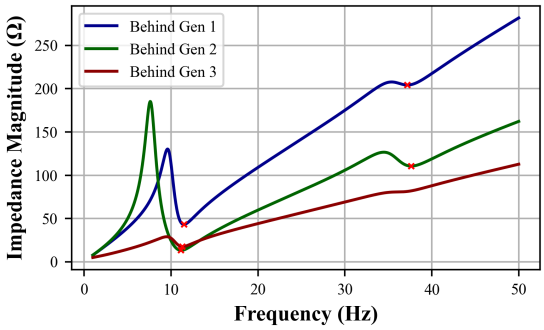


(c) Impedance profiles when FSC 7-8 is bypassed

Figure 5.5: Impedance profiles when FSCs are bypassed

Upon identification of all network resonances in the system, FSC were bypassed one at a time and frequency scans were obtained. As per Fig. 5.5a, the impedance dip at network mode 3 frequency is disappeared when the FSC in the upper parallel branch from bus 4 to 5 is bypassed, while mode 2 frequency remain unchanged. This implies that mode 3 is mostly excited due to the FSC (1) in branch 4 to 5 and mode 2 has negligible effect. This observation is verified through participation factor analysis

in Fig. 5.2c. FSC (1) in branch 4 to 5 partially contributes to the formation of mode 1, as its frequency is detuned upon bypassing. When FSC (2) in branch 4 to 5 is bypassed, the impedance dip at mode 1 frequency is disappeared and impedance dip at the frequency of mode 3 has shifted a little as seen from Fig. 5.5b. It implies that FSC (2) in branch 4 to 5 contributes the most to the formation of mode 2. According to Fig. 5.5c, impedance dip at mode 2 frequency is disappeared when the FSC in branch 7 to 8 is bypassed and the frequency of mode 3 remains unchanged. Thus, it can be concluded that mode 2 is mostly excited due to the FSC in branch 7 to 8 and mode 3 frequency does not have any effect from FSC in branch 7 to 8. Recall that replacing a FSC fully with a TCSC also eliminates the network resonance, similar to bypassing the FSC, even though it introduces a small inductive impedance to the network.

In summary, if SSR conditions are detected in a network at a certain frequency, frequency scanning can be conducted at the screening stage of the study to identify the resonant conditions and locate the FSC which causes the particular SSR, as below,

1. Conduct frequency scans behind every generator/device from frequency $0 - f_0$ Hz

   (a) Plot magnitude and phase of the impedance versus frequency

   (b) Identify the dips of at least 5% in impedance. These are the resonant frequencies at which there may be risks of SSR. Some network resonances such as intra-parallel line resonances may not appear in the impedance profiles. Such resonances are unlikely to cause any interactions with generators as they are not observed at the generator terminals.

2. Bypass each FSC at a time and repeat frequency scans behind every generator/device

   (a) Plot magnitude and phase of the impedance versus frequency

   (b) Notice the disappearing impedance dips and identify the corresponding frequencies. These are the resonances which appear due to the bypassed FSC.

   (c) Locate the critical FSC corresponding to the problematic SSR frequency.

## 5.3 Design of a Sub-Synchronous Damping Controller

In section 4.4, it was highlighted that the inherent damping provided by the TCSC can prevent TIs when the FSC is completely replaced by a TCSC. However, when TCSC levels are low, there is still a possibility of TIs due to the presence of the network resonance. Although primary current controllers can somewhat enhance the inherent damping properties of the TCSC at sub-synchronous frequencies, these controllers are not specifically designed to enhance SSR damping. Therefore, when TCSC levels are low, the mitigation of TIs can be ensured through properly designed SSDCs to be used along with the TCSC. The design procedure of a SSDC through the use of eigenpropertise is shown in this section.

Eigenproperties offer valuable insights into system behavior, enabling the design of controllers to achieve desired stability and performance. Eigenproperties such as Eigenvalues, Eigenvectors, Participation Factors, Controllability, Observability etc.

Table 5.2: Eigenvalues of IEEE 1st benchmark system with series compensation of 31% achieved with 30% TCSC

| Eigenvalue | F (Hz) | D (%) | Type of Mode |
|---|---|---|---|
| $0 \pm 298.17i$ | 47.45 | 0 | TM4 |
| $0.058 \pm 202.53i$ | 32.23 | -0.028 | TM3 |
| $0.011 \pm 160.03i$ | 25.47 | -0.0069 | TM2 |
| $0.0167 \pm 101.03i$ | 16.08 | -0.016 | TM1 |
| $-14.108 \pm 238.89i$ | 38.021 | 5.89 | NM |
| $-0.423 \pm 8.9269i$ | 1.42 | 4.74 | EM |

will be used in the design of the SSDC. Further details on derivations and explanations on Eigenproperties are found in [1].

### 5.3.1 Application of Eigen-Properties for SSDC Design

The design procedure of the SSDC is demonstrated through the adopted IEEE 1$^{st}$ benchmark system for SSR studies, when the total series compensation of 31% is achieved with a combination of 70% FSC and 30% TCSC. As demonstrated in Fig. 4.10b, 30% TCSC is unable to damp the growing torsional oscillations. Eigenvalues of the system are shown in Table 5.2

The SSDC must be designed to damp the undamped torsional oscillations (TM1-TM4). The firing angle of the TCSC is chosen as the control input to the system. The controllability of the modes in Table 5.2 through the firing angle of the TCSC as the input is shown in Table 5.3. Accordingly, the most controllable mode through the firing angle is the network mode. Eventhough the controllability of the torsional modes is relatively low, they are non-zero, indicating that they remain controllable.

The block diagram of the SSDC is shown in Fig. 5.6, which consist of a washout filter, a gain block and one lead/lag filter. The SSDC introduces an additional com-

Table 5.3: Controllability of modes through the TCSC firing angle

| Mode | Controllability index |
|---|---|
| TM4 | 0.00084 |
| TM3 | 0.135 |
| TM2 | 0.087 |
| TM1 | 0.167 |
| NM | 21.4 |
| EM | 1.15 |

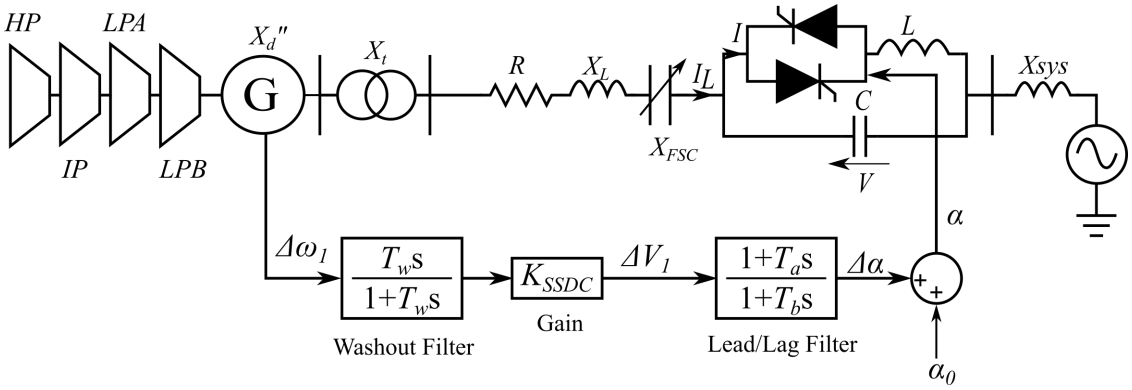


Figure 5.6: IEEE 1st Benchmark Model with a TCSC equipped with an SSDC

ponent ($\Delta\alpha$) to the desired firing angle input ($\alpha_0$) in order to supply the necessary damping. The firing angle input $\alpha_0$ can be generated by primary controllers such as current controllers. However, for this study, it remains constant, corresponding to the required impedance of the TCSC.

When choosing the input signal to the damping controller, two physical quantities that can be measured and available were considered. They are the line current ($I_L$) and the generator speed deviation ($\Delta\omega$). The observability of modes through these two outputs are shown in Table 5.4. It is seen that torsional modes are observable through both outputs, with higher observability through the line current.

It's important to highlight that the network and electromechanical mode, along with the remaining modes, are controllable and observable through the chosen control

Table 5.4: Observability of modes in the time response of line current and generator speed deviation

| Mode | Observability ($I_L$) | Observability ($\Delta\omega$) |
|---|---|---|
| TM4 | 0.001244 | 0.00214 |
| TM3 | 0.4045 | 0.1029 |
| TM2 | 0.2023 | 0.053 |
| TM1 | 0.3524 | 0.0661 |
| NM | 0.338 | 0.00144 |
| EM | 0.466 | 0.007 |

input signal and system outputs. Hence, these modes can also be influenced by the SSDC. The selection of the input signal to the SSDC ($I_L$ or $\Delta\omega$) was determined based on the residues calculated for each mode. Refer the block diagram of the closed loop system in Fig. 5.7.

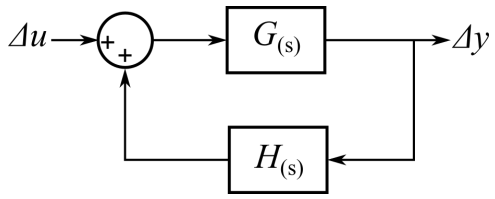


Figure 5.7: Block diagram of a feedback loop system

The closed loop transfer function of the above system can be expressed as (5.1)

$$\frac{\Delta y_{(s)}}{\Delta u_{(s)}} = \frac{G_{(s)}}{1 + G_{(s)}H_{(s)}} \tag{5.1}$$

Closed loop transfer function expressed in terms of Residues as in (5.2).

$$\frac{\Delta y_{(s)}}{\Delta u_{(s)}} = \sum_{i=1}^{n} \left( \frac{\dfrac{R_i}{s-\lambda_i}}{1 + \dfrac{R_i H_{(s)}}{s-\lambda_i}} \right) = \sum_{i=1}^{n} \frac{R_i}{s - \lambda_i + R_i H_{(s)}} \tag{5.2}$$

The impact of the feedback loop on the eigenvalues of the closed-loop system can be seen from (5.2). Hence, the feedback loop can be designed to place the eigenvalues at the desired place in the complex plane. The new eigenvalues of the closed loop

system are '$\lambda_i - R_i H_{\lambda_i}$'. It is important to note that besides the feedback transfer function, residues significantly contribute to the shift in eigenvalues. The larger the magnitude of the residues, the greater their effect on the movement of eigenvalues through the selected input and output.

If the feedback loop system is expressed as a combination of a simple gain $K$ and a dynamic function, the displacement of the eigenvalue $\Delta\lambda_i$ can be expressed as in (5.3).

$$\Delta\lambda_i = -R_i K H_{(\lambda_i)} \tag{5.3}$$

If the feedback loop consists only of a gain factor $K$, according to (5.4), the direction of the movement of the eigenvalue is determined by the angle of the residues.

$$\Delta\lambda_i = -|R_i| K e^{j\angle R_i} \tag{5.4}$$

Therefore, when selecting the input signals to the SSDC, the magnitudes of the residues quantify the influence on the displacement of eigenvalues whereas the angle influence the direction of the movement of eigenvalues. The magnitude and angle of eigenvalue displacement can be expressed as in (5.5) and (5.6).

$$|\Delta\lambda_i| = |R_i| K |H_{(\lambda_i)}| \tag{5.5}$$

$$\angle\Delta\lambda_i = \angle R_i + \angle H_{(\lambda_i)} \tag{5.6}$$

The phase of the feedback transfer function can be designed to move the a particular eigenvalue in the desired direction and the gain of the SSDC can be determined

according to (5.7).

$$K_{SSDC} = \frac{|\Delta\lambda_i|}{|R_i||H_{(\lambda_i)}|} \tag{5.7}$$

Residues calculated for each mode with firing angle as the input and line current and generator speed deviation as the output is given in Table 5.5. Figure 5.8 shows the polar plot of the residues for both outputs to visualize the direction of eigenvalue movement.

Table 5.5: Residues

| **Mode** | **Output** $= \Delta\omega$ | | **Output** $= I_L$ | |
|---|---|---|---|---|
| | $\lvert R_i \rvert$ | $\angle R_i^0$ | $\lvert R_i \rvert$ | $\angle R_i^0$ |
| TM4 | 1.79e-06 | 123.3655 | 1.04e-06 | 3.0755 |
| TM3 | 0.0139 | -73.7234 | 0.0547 | -172.3594 |
| TM2 | 0.0046 | -54.5816 | 0.0176 | -146.8318 |
| TM1 | 0.011 | -37.9347 | 0.0588 | -128.5181 |
| NM | 0.0309 | 105.5679 | 7.2457 | 37.3326 |
| EM | 0.0088 | -0.4357 | 0.5383 | -86.7066 |

In terms of the magnitudes of the residues, the highest values, corresponding to the torsional modes, are obtained when considering the line current as the output (Input to the SSDC). However, to shift the unstable torsional mode 1 (TM1) to the left half of the complex plane without altering its frequency, a phase lag of $142.07^0$ is required when the input to the SSDC is $\Delta\omega$. This phase shift is expected to move other torsional modes and the electromechanical mode towards the left half of the complex plane, except for the TM4. With a phase lag of $142.07^0$, there is a chance of the network mode moving towards the right half of the plane. However, given the low magnitude of the residue and the well-damped network mode, torsional modes damping can be improved at the cost of slight reduction in network mode damping.

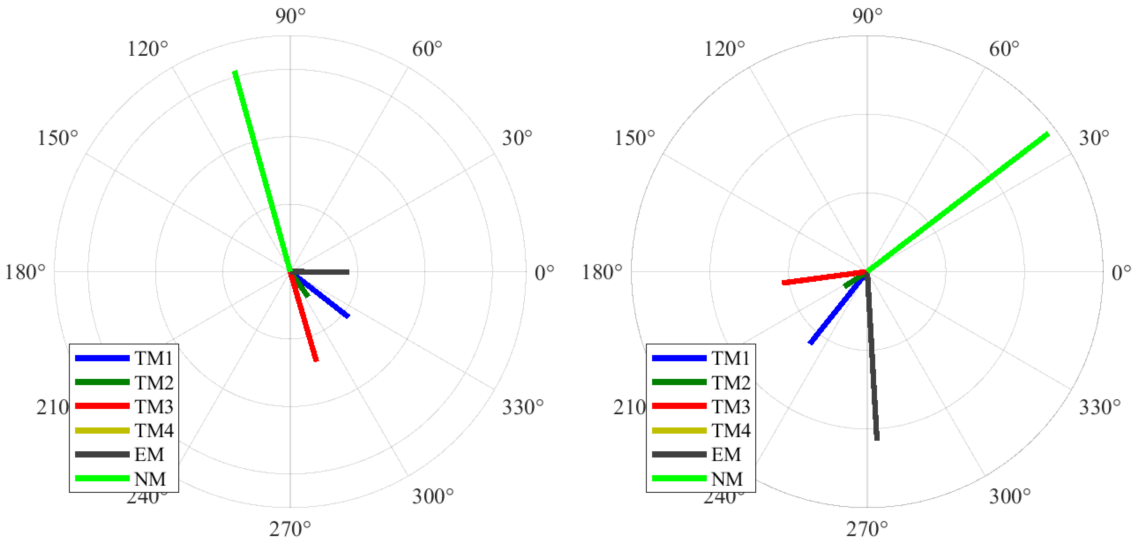


(a) (b)

Figure 5.8: Polar plot of residues with (a) $\Delta\omega$ as the output and (b) $\Delta IL$ as the output

Alternatively, if the line current is chosen as the input to the SSDC, a phase lag of $52^0$ is required to shift TM1. This shift has a positive impact on the torsional and electromechanical modes, while the network mode has a high chance of moving significantly towards the right half of the complex plane with a much larger residue magnitude compared to the speed deviation as the output. Therefore, there is a risk of adverse effects on the network mode stability at high SSDC gains. Hence, the safer option would be to use the generator speed deviation as the input to the SSDC.

By selecting the generator speed deviation as the input signal for the SSDC, the slip speed goes through a washout filter, which essentially acts as a high-pass filter. This filter is designed to only allow oscillations above a certain cutoff frequency to pass through, and prevent it from responding to steady state operation. The washout filter's time constant was set to 5 seconds, allowing it to pass oscillations in $\Delta\omega$ above 0.2 Hz. Determining the SSDC gain and the time constants of the lead-lag filter

depends on the desired location of the unstable eigenvalue. Eigenvalue corresponding to TM1 was chosen to be moved to the left half of the complex plane with a real part of -0.2, while keeping its frequency a constant. Hence the displacement of the eigenvalue corresponding to 16.08 Hz is,

$$\Delta\lambda_{16Hz} = (-0.2 \pm 101.03i) - (0.0167 \pm 101.03i) = -0.2167$$

The required phase compensation from the SSDC at 16.08 Hz is,

$$\angle\Delta\lambda_{16Hz} = 0 = \angle R_{16Hz} + \angle H_{(\lambda_{16Hz})}$$

$$\angle H_{(\lambda_{16Hz})} = +37.9347^0$$

An angle lead of $37.93^0$ must be provided by the combined washout filter and the lead-lag filter. The phase shift introduced by the washout filter at TM1 frequency (16.08 Hz) is as low as $0.1134^0$. Hence the total phase compensation must be provided through the lead-lag block. The time constants of the lead-lag block can be determined according to (5.8) to (5.10).

$$a = \frac{1 - \sin(\theta)}{1 + \sin(\theta)} \tag{5.8}$$

$$T_a = \frac{1}{2\pi f_x \sqrt{a}} \tag{5.9}$$

$$T_b = aT_a \tag{5.10}$$

Where $\theta$ is the required phase compensation and $f_x$ is the frequency of the mode corresponding to the shifted eigenvalue. As a result, the values of Ta and Tb were found as 0.0203 and 0.0079, respectively. The required SSDC gain is found to be 9.6 according to (5.7).

### 5.3.2 Linearized Model of the SSDC

Considering the block diagram of the SSDC shown in Fig. 5.6, two state variables $\Delta V_1$ and $\Delta\alpha$ are identified. The output of the SSDC which is an additional component of the firing angle is now a state variable. The differential equations of the washout filter together with the gain can be written as in (5.11).

$$\dot{\Delta}V_1 = -\frac{1}{T_w}\Delta V_1 + K_{ssdc}\Delta\dot{\omega}_1 \tag{5.11}$$

The differential equations of the lead/lag filter can be formulated as in (5.12)

$$\dot{\Delta}\alpha = -\frac{1}{T_b}\Delta\alpha + \left(\frac{1}{T_b} - \frac{T_a}{T_b T_w}\right)\Delta V_1 + \left(\frac{T_a}{T_b}K_{ssdc}\right)\Delta\dot{\omega}_1 \tag{5.12}$$

The term $\Delta\dot{\omega}_1$ can be obtained from the generator model in terms of generator state variables as follows. Consider the speed of the generator expressed as,

$$\mathbf{\Delta y_g} = \mathbf{C_{gs}}\mathbf{\Delta x_g}$$

Where,

$$\mathbf{C_{gs}}(2,1) = 1 \qquad\qquad \mathbf{\Delta y_g} = [\Delta\omega_1]$$

Then,

$$\mathbf{\Delta\dot{y}_g} = \mathbf{C_{gs}}\mathbf{\Delta\dot{x}_g}$$

$$\Delta\dot{\omega}_1 = \mathbf{C_{gs}}\left(\mathbf{A_g}\mathbf{\Delta x_g} + \mathbf{B_g}\mathbf{\Delta u_g} + \mathbf{E_g}\mathbf{\Delta v_g}\right)$$

The final linearized state space model of the SSDC is expressed in (5.13).

$$\mathbf{\Delta\dot{x}_{SSDC}} = \mathbf{A_{ssdc1}}\mathbf{\Delta x_{SSDC}} + \mathbf{A_{ssdc2}}\mathbf{\Delta x_g} + \mathbf{B_{ssdc}}\mathbf{\Delta u_g} + \mathbf{E_{ssdc}}\mathbf{\Delta v_g} \tag{5.13}$$

Where,

$$\mathbf{\Delta x_{SSDC}} = [\Delta V_1, \Delta\alpha]^T$$

Table 5.6: Eigenvalues of IEEE 1st benchmark system compensated with SSDC on TCSC

| Mode | Without SSDC | | With SSDC | | |
|---|---|---|---|---|---|
| | F (Hz) | D (%) | F (Hz) | D (%) | Eigen Value |
| TM4 | 47.45 | 0 | 47.45 | 0 | $0 \pm 298.17i$ |
| TM3 | 32.23 | -0.028 | 32.28 | 0.126 | $-0.257 \pm 202.8i$ |
| TM2 | 25.47 | -0.0069 | 25.47 | 0.064 | $-0.102 \pm 160.07i$ |
| TM1 | 16.08 | -0.016 | 16.08 | 0.199 | $-0.20 \pm 101.05i$ |
| NM | 38.021 | 5.89 | 37.9 | 5.61 | $-13.387 \pm 238.21i$ |
| EM | 1.42 | 4.74 | 1.417 | 5.68 | $-0.507 \pm 8.914i$ |

$$\mathbf{A_{ssdc1}} = \begin{bmatrix} -\frac{1}{T_w} & 0 \\ \left(\frac{1}{T_b} - \frac{T_a}{T_b T_w}\right) & -\frac{1}{T_b} \end{bmatrix} \qquad \mathbf{A_{ssdc2}} = \begin{bmatrix} K_{ssdc}\mathbf{C_{gs}}\mathbf{A_g} & \frac{T_a}{T_b}K_{ssdc}\mathbf{C_{gs}}\mathbf{A_g} \end{bmatrix}$$

$$\mathbf{B_{ssdc}} = \begin{bmatrix} K_{ssdc}\mathbf{C_{gs}}\mathbf{B_g} & \frac{T_a}{T_b}K_{ssdc}\mathbf{C_{gs}}\mathbf{B_g} \end{bmatrix} \qquad \mathbf{C_{ssdc}} = \begin{bmatrix} K_{ssdc}\mathbf{C_{gs}}\mathbf{E_g} & \frac{T_a}{T_b}K_{ssdc}\mathbf{C_{gs}}\mathbf{E_g} \end{bmatrix}$$

### 5.3.3 Effect of the SSDC

The linearized model of the designed SSDC was added to the linearized model of the system in Fig. 5.6 and the effect of the SSDC activity on the modes are shown in Table 5.6. Note that all torsional modes are well damped and the eigenvalue corresponding to TM1 is at the desired location. The action of SSDC has also improved the damping of the electromechanical mode. However, the damping of the network mode has slightly degraded as expected, but it remains adequately damped.

The impact of high SSDC gains on the modes are shown in Fig. 5.9. The SSDC gain is increased from 9.6 to 200, and the loci of torsional, network and electromechanical mode is plotted in Fig. 5.9. Torsional modes and electromechanical modes becomes more damped with increasing SSDC gains while the network mode tend to become unstable even with a low residue magnitude. However, achieving high levels of torsional mode damping is possible before the network mode becomes unstable.

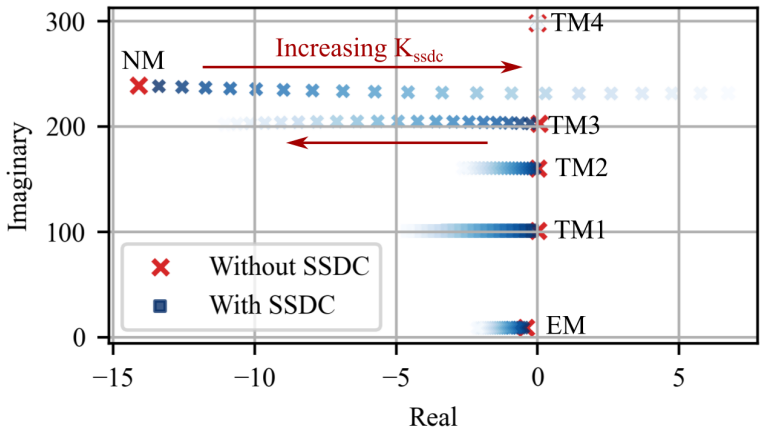


Figure 5.9: Impact of SSDC gains on eigenvalues of SSR modes

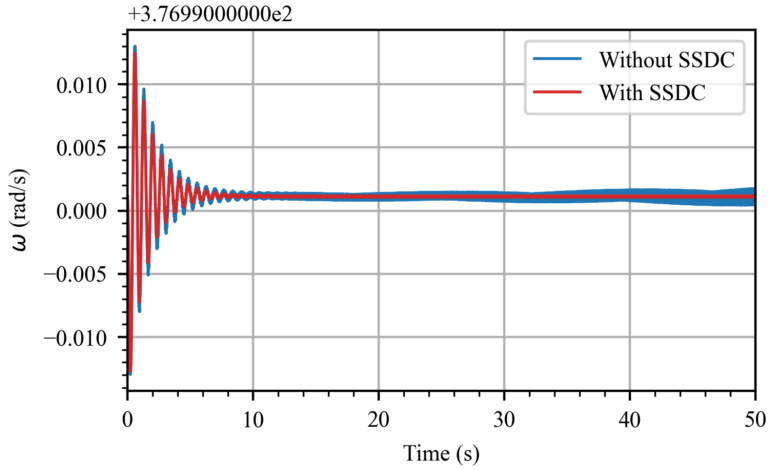


Figure 5.10: Generator speed with and without the SSDC

Selecting the line current as the input to the SSDC may limit the level of damping achievable for torsional modes, given its high residue magnitude.

Figure 5.10 shows EMT simulation results of the generator speed with and without the application of the SSDC. It is evident that the designed SSDC properly mitigates TIs. Comparison of time-domain response of the linearized model against EMT simulation results shown in Fig. 5.11 shows a good match.

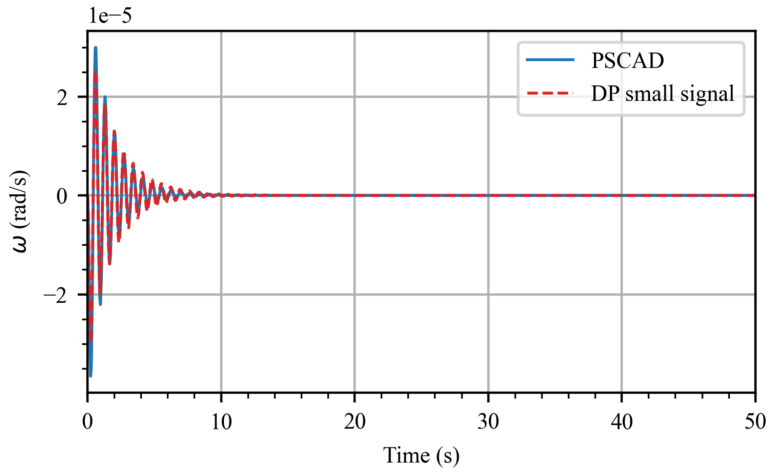


Figure 5.11: Comparison of time responses of the small-signal model with SSDC against EMT simulation results

## 5.4 Study Procedure

This thesis proposes procedures for utilizing TCSCs to address, (1) IGE and, (2) TI in heavily series-compensated networks. The methodology of identifying the critical FSC through screening as discussed in section (5.2), and the design procedure of the SSDC is used in the study procedure. The outcome of the study procedure is a systematic approach for identifying, analysing and mitigating SSR problems with TCSCs in a heavily series compensated networks.

### 5.4.1 Study Procedure for the Application of TCSCs to Address IGE in Multiple Series Compensated Networks

The following procedure is proposed to detect and address IGE in heavily series compensated networks that has multiple CTG in the vicinity. In cases where the studied system is large, it is recommended to reduce and narrow the study area to areas with highly concentrated FSC are present. The reduced network should also

include nearby dynamic devices like CTG and WPP which are susceptible to SSR .

1. **Screening**

   (a) Perform frequency scanning to all dynamic devices in the focus area to capture the true resistance and reactance in the sub-synchronous frequency range. Dynamic frequency scanning through signal injection technique can capture the frequency dependant impedance.

   - Dynamic devices must be detached from the network and the respective operating point must be established through an external voltage/current source behind the short circuit impedance at the POC.
   - Small amplitude (1%-5%) voltage or current signals of frequency '$f$' are superimposed on the external voltage/current source.
   - Measure the voltage and current corresponding to the injected frequency and calculate the impedance of the device at frequency '$f$'.
   - Repeat signal injection for the entire sub-synchronous frequency range with an appropriate step size.

   (b) Obtain static frequency scans of the network for the sub-synchronous frequency range, in the absence of dynamic devices.

   - Static frequency scans are simply a formulation of the admittance matrix at every frequency. Hence, this can be calculated analytically, or static frequency scanning tools available in EMT software can be used with devices disconnected from the network.

   (c) Calculate the equivalent impedance seen behind all dynamic devices in the

study area for the entire sub-synchronous frequency range by combining the static frequency scans and dynamic frequency scans appropriately.

- Impedance profiles of all devices except for the device under study must be attached to the respective diagonal elements of the admittance matrix formulated in step (b).
- Reduce the admittance matrix to the POC bus of the device under study, by eliminating other nodes.
- Combine the reduced impedance with the impedance of the device under study at every frequency by adding.
- Plot magnitude and phase of the impedance versus frequency

(d) The combined impedance profile indicate network resonances seen by the device under study. Identify the network resonances at which the resistance is negative or almost zero (critical network resonances). There are risks of IGE at these frequencies.

(e) Repeat steps (b) and (c) while bypassing FSC at a time to identify the FSC which contributes the most to the excitation of critical network resonances.

i. Note the FSC which makes the critical network resonances disappear from the frequency scans.

ii. It has to be noted that bypassing a certain FSC is likely to affect other network resonances. Careful consideration must be given to track the movement of other network resonances.

iii. In cases where it is difficult to identify the movement and disappearance of network resonances, it is recommended to do a sensitivity study

by changing the FSC value instead of bypassing straight-away.

2. **Detailed Analysis**

   (a) Replace the identified critical FSC fully with a TCSC designed to provide the same level of compensation at a boost factor of 1.2 or above with a reasonable characteristic factor of around 2.5.

      i. At this stage, the TCSC is operated in open-loop configuration with a constant firing angle. The damping provided by the TCSC is purely due to its inherent nature.

      ii. TCSC can also be equipped with additional primary level controls such as current or power controllers upon the requirement. Adding basic controllers is less likely to deteriorate damping unless additional damping is introduced as demonstrated in Chapter 4.

   (b) Perform EMT studies or small-signal stability assessment (if models are available) to ensure that network mode instability is avoided.

   (c) Gradually reduce the percentage of TCSC in EMT simulations or small-signal program and determine the appropriate level of series compensation sufficient to avoid SSR in the study area due to IGE.

      i. It should also be noted that Supplementary Damping controllers are not necessary to avoid IGE as the inherent damping provided by the TCSC itself is sufficient when the TCSC is properly designed.

### 5.4.2 Study Procedure for the Application of TCSCs to Address TI in Multiple Series Compensated Networks

The following procedure is proposed to avoid TIs using TCSCs in multiple series compensated networks.

1. **Screening**

   (a) Upon identification of Torsional instabilities, locate the FSC which excites network resonances close to the unstable torsional oscillations by following the screening procedure described in the study procedure in section (5.4.1)

   - locate the FSC which corresponds to network resonances that are close to the most unstable torsional oscillation of the generator under study while confirming that they are visible in the impedance profiles obtained behind the generator.
   - As described in Chapter 4, most unstable torsional oscillations are the modes which are close to the network resonant frequencies. Hence, these network resonances are more likely to adversely interact with the torsional modes of the CTG.

2. **Detailed studies**

   (a) Replace the critical FSCs fully with TCSCs without additional damping controllers and check if TI are avoided through EMT simulations or small-signal stability analysis.

   - Replacing the FSC with TCSC will eliminate the particular network resonance. However, due to the presence of other network resonances

in the system and if they are seen at the generator terminal, there is still a chance for TI to occur if the mechanical damping is low.

- Replacing few other FSCs with TCSCs, which corresponds to the excitation of network resonances seen at the generator terminal is also another option, but having multiple TCSCs is economically not viable.

(b) If the TI are avoided, the level of TCSC can be gradually reduced to determine an appropriate level.

(c) If TI is not mitigated, SSDCs must be implemented on the TCSC at an appropriate location. Small-signal stability assessment is recommended for the design of SSDC.

i. Choose a location for the TCSC with the SSDC to be installed. Two factors must be considered when choosing the location

A. Location at the inherent damping capability can be maximally utilized - Replace FSC with TCSC operating in open loop and identify the location at which torsional modes are most damped due to the inherent nature of the TCSC.

B. Location at which the unstable torsional modes are most controllable through the firing angle of the TCSC - Use controllability indices.

ii. Choose an appropriate signal as the input to the SSDC.

A. Evaluate residues for the unstable torsional modes corresponding to candidate input signals to the SSDC, and choose the signals which provide the highest residue magnitudes to unstable torsional

modes.

B. If torsional modes of multiple generators are unstable, a single input to the SSDC may not be adequate to damp all torsional modes. Consider the use of combinations of input signals which can provide better results.

iii. Design the SSDC according to the required phase compensation and eigenvalue displacement through small-signal stability assessment.

- Care must be given to other modes of which residues are nonzero, as they are likely to be displaced due to the SSDC action.

iv. Verify the performance of the SSDC through EMT simulations

## 5.5 Case Study

A case study is formulated and the proposed study procedures are applied to resolve IGE and TI problems in the network. The problem formulation draws inspiration from real-world challenges associated with devices near heavily series-compensated network segments, as discussed in section 5.1. Both the inherent damping capability and supplementary damping controllers are utilized as needed in this case study.

### 5.5.1 Test System

A test network of radial nature is developed which includes multiple series compensated lines and CTGs as illustrated in Fig. 5.12. This test network is adopted to demonstrate both the IGE phenomena and TIs, destabilizing multiple torsional modes of nearby CTG. It consist of five series compensated lines and three CTGs.

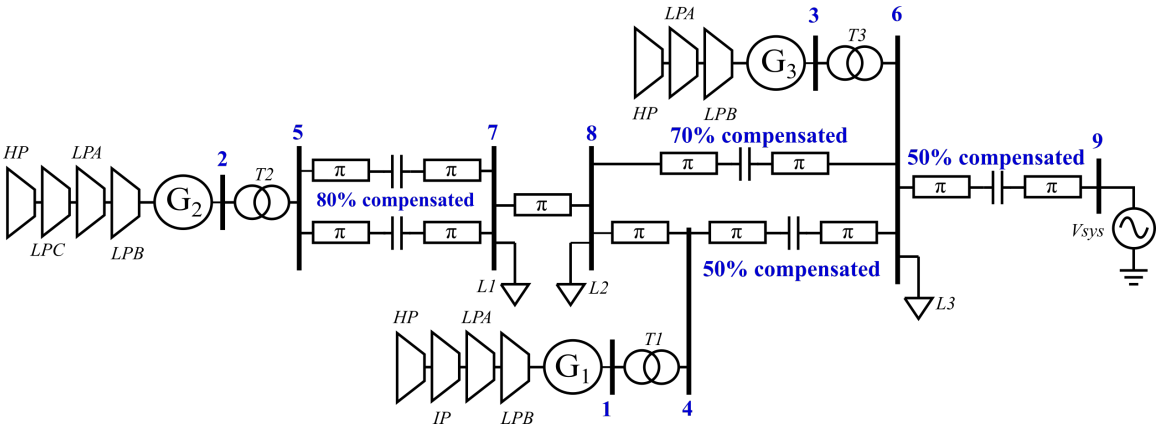


Figure 5.12: Test system

Generator 3 is equipped with an AC4A exciter which is treated as a mechanical mass for torsional interaction studies. The network and generator data are provided in the Appendix E.1.

To demonstrate the IGE phenomena in the above network, all network resistances were assumed to be zero and multi-mass sets are ignored. For TI analysis, resistances are restored to their actual values and the multi-masses are enabled. Mechanical damping of all multi-mass models were assumed to be zero for worst case scenario.

### 5.5.2 Application of the Study Procedure to Mitigate IGE

The procedure described in section (5.4.1) is applied to the test system in Fig. 5.12. The frequency scans behind all three CTGs obtained at step (d) are shown in Fig. 5.13 and it reveals four series resonant points. As there are five FSC, there should be five network resonances. However, as the two parallel lines between bus 5 and 7 are of same series compensation level, the intra parallel line network resonance is not visible to any generator. It can be identified that a critical network resonance exist at 39.25 Hz at which the resistance seen from all three generators are negative, while

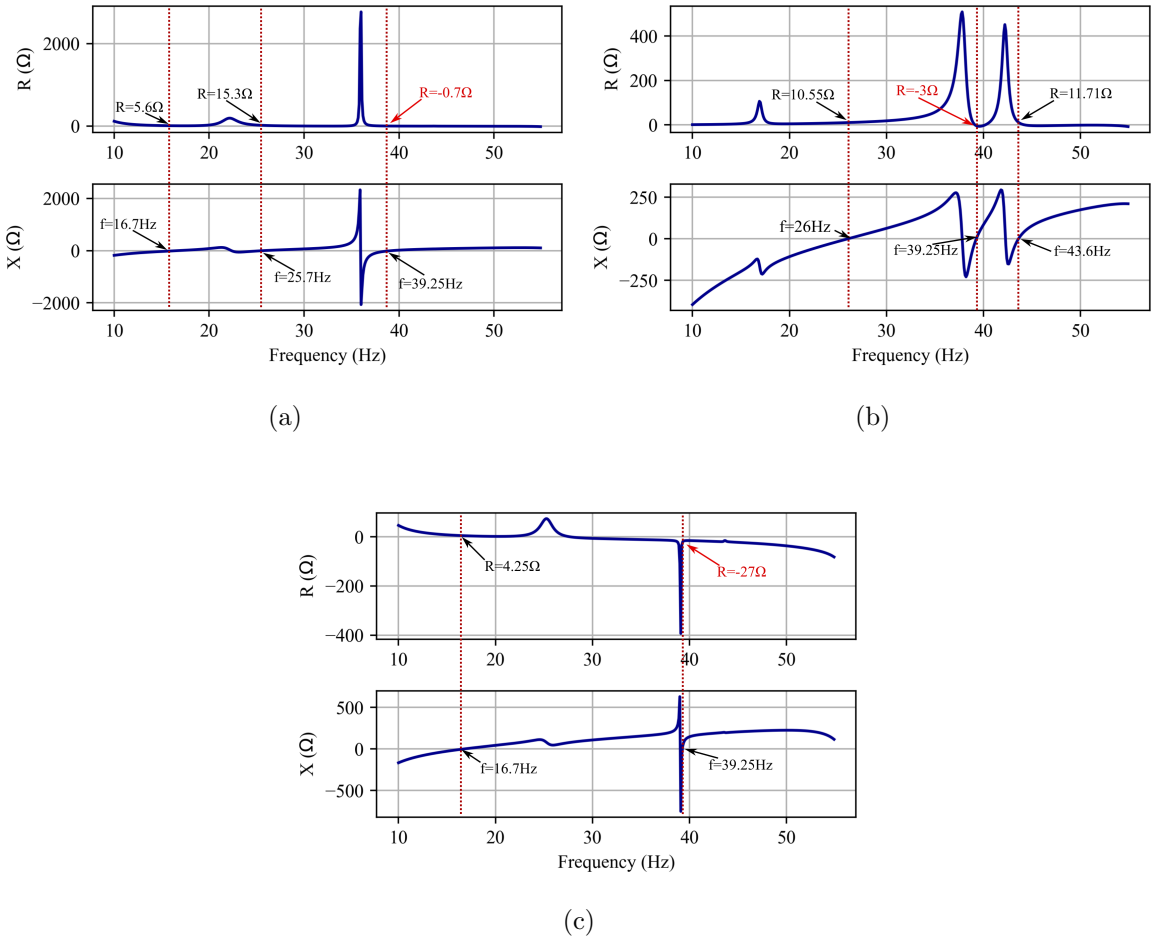


Figure 5.13: Impedance profiles behind neutral point of CTGs (a) G1, (b) G2, and (c) G3

all other network resonances are positively damped.

To identify the critical FSC which contributes the most to the formation of 39.25 Hz network resonance, step (e) is performed. Two FSC which eliminates the critical network resonance were identified: FSC from bus 6-9 and bus 4-6. Frequency scans obtained while bypassing these two FSCs are shown in Fig. 5.14. When FSC 6-9 is bypassed, 39.25 Hz resonance has disappeared in Fig.5.14a (Behind G1) and Fig.5.14b (Behind G2). Furthermore, 43.6 Hz resonance remains unchanged, while other two resonances are slightly detuned. However, none of the detuned resonances

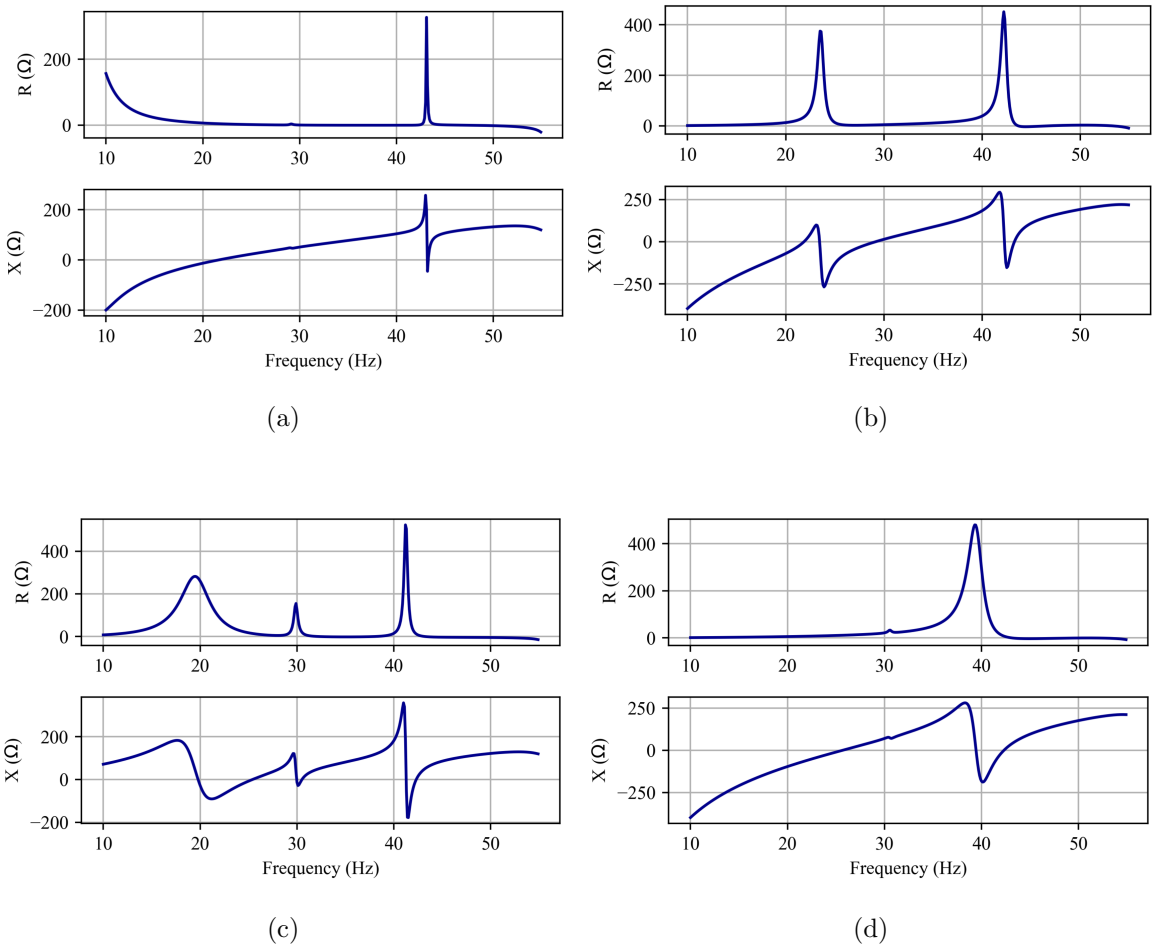


Figure 5.14: Impedance profiles behind neutral point of CTG (a) G1 when FSC 6-9 is bypassed, (b) G2 when FSC 6-9 is bypassed, (c) G1 when FSC 4-6 is bypassed, and (d) G2 when FSC 4-6 is bypassed

were found to be negatively damped upon bypassing. Similarly, when FSC from 4-6 is bypassed, 39.25 Hz resonance disappears, while 43.6 Hz and 25.7 Hz resonances remains unchanged.

After choosing the two candidate locations, line 4-6 and line 6-9, for TCSC installation, detailed EMT and small-signal studies were conducted. FSCs were fully replaced with TCSCs designed at a boost factor of 1.2 and a characteristic factor of 2.5. TCSC was operated to provide the same level of compensation at a fixed

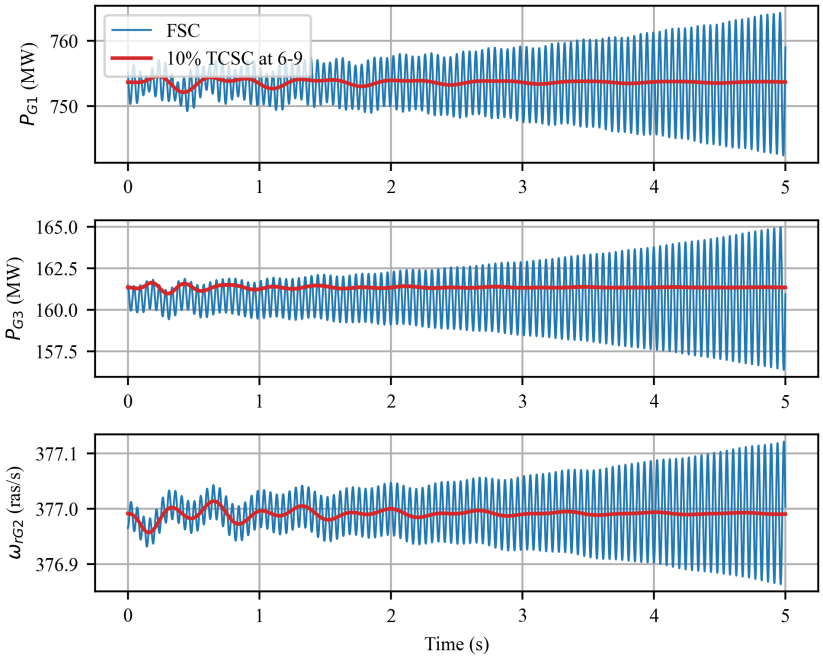


Figure 5.15: PSCAD responses for active power output of generator 1, 2 and rotor speed of generator 3 when 10% of line 6-9 is replaced with a TCSC

firing angle. The level of TCSC was then reduced and Fig. 5.15 shows responses from EMT simulation when line 6-9 has only 10% of TCSC. Figure 5.16 also confirms that replacing 10% of series compensation in line 4-6 with a TCSC also mitigates IGE. When the FSC in line 8-6 is fully replaced with a TCSC, as shown in Fig. 5.17, IGE is not eliminated despite TCSC's inherent damping capability. Hence, it is evident that even a TCSC level as low as 10% is able to avoid IGE in multiple series compensated networks, through its inherent damping capability, provided that it is installed at the right location.

Results from small-signal stability assessment are shown in Table 5.7, which compares the network resonances and their damping when there FSCs and TCSCs at different locations. It is evident that the 20.75 Hz unstable network resonance (39.25 Hz

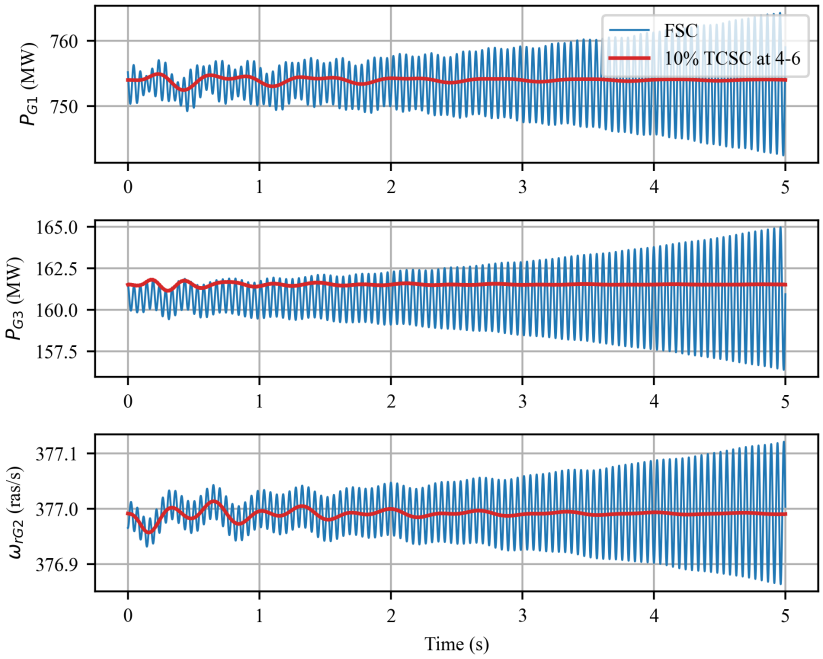


Figure 5.16: PSCAD responses for active power output of generator 1, 2 and rotor speed of generator 3 when 10% of line 4-6 is replaced with a TCSC

Table 5.7: Network modes in the test system with FSCs, 100% TCSC at 6-9, 100% TCSC at 4-6 and 100% TCSC at 8-6 (frequencies are in rotor reference frame)

| **FSC** | | **100% TCSC at 6-9** | | **100% TCSC at 4-6** | | **100% TCSC at 8-6** | |
|---|---|---|---|---|---|---|---|
| **F (Hz)** | **D (%)** | **F (Hz)** | **D (%)** | **F (Hz)** | **D (%)** | **F (Hz)** | **D (%)** |
| 43.24 | 0.601 | 39.85 | 5.47 | 34.14 | 2.79 | 37.54 | 11.22 |
| 34.03 | 1.75 | 32.11 | 4.53 | 32.44 | 15.07 | 33.9 | 2.42 |
| 20.75 | -0.19 | - | - | - | - | 20.75 | -0.19 |
| 16.37 | 0.56 | 16.76 | 0.80 | 17.89 | 2.09 | - | - |
| 6.55 | 0.006 | 6.54 | 0.006 | 6.55 | 0.006 | 6.55 | 0.006 |

in frequency scan profiles) is eliminated in both scenarios, i.e. when the FSC in line 6-9 and 4-6 is replaced with a TCSC. However, when the FSC in line 8-6 is replaced with a TCSC, the unstable network resonance is not eliminated.

It was observed that the network resonances obtained when the FSC is fully replaced with a TCSC are somewhat similar to the network resonances observed

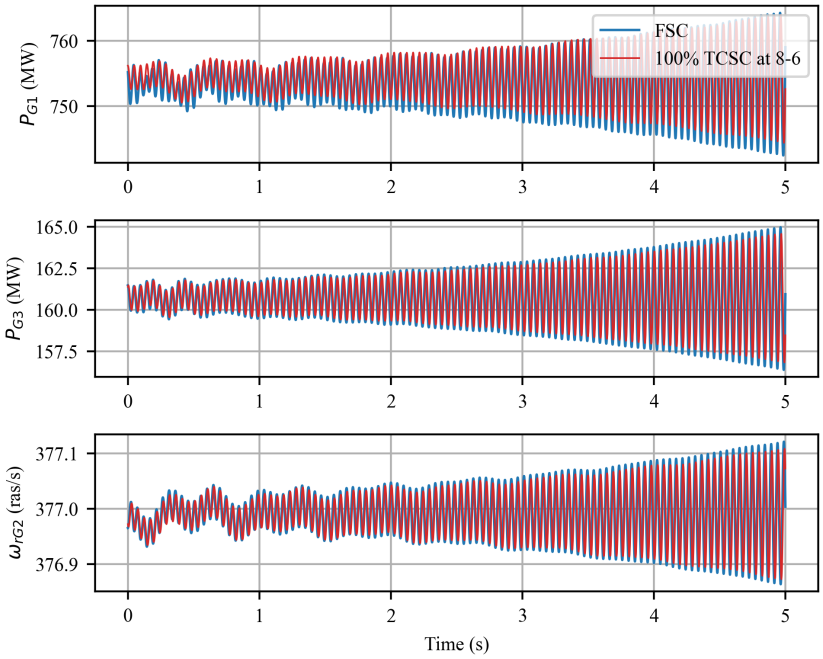


Figure 5.17: PSCAD responses for active power output of generator 1, 2 and rotor speed of generator 3 when 100% of line 8-6 is replaced with a TCSC

when the FSC is bypassed. Refer the Table 5.8 which shows network modes when the corresponding FSC are bypassed. Note that the frequencies are close to that obtained when there is a TCSC, except that the TCSC adds more damping. This implies that frequency scans obtained by bypassing the FSC provide insight into the resulting network resonance frequencies when the same FSC is fully replaced with a TCSC. Hence, selecting critical FSC locations as candidate locations for TCSCs is justified, as they are likely to yield similar network resonances but with increased damping.

Table 5.8: Network modes in the test system with FSC at 6-9, 4-6 and 7-8 bypassed (frequencies are in rotor reference frame)

| **FSC** | | **Bypass FSC 6-9** | | **Bypass FSC 4-6** | | **Bypass FSC 8-6** | |
|---|---|---|---|---|---|---|---|
| **F (Hz)** | **D (%)** | **F (Hz)** | **D (%)** | **F (Hz)** | **D (%)** | **F (Hz)** | **D (%)** |
| 43.24 | 0.601 | 38.28 | 1.37 | 34.37 | 1.84 | 34.70 | 1.48 |
| 34.03 | 1.75 | 30.86 | 0.46 | 29.39 | 0.71 | 31.93 | 0.44 |
| 20.75 | -0.19 | - | - | - | - | 20.75 | -0.19 |
| 16.37 | 0.56 | 16.70 | 0.34 | 17.67 | 0.49 | - | - |
| 6.55 | 0.006 | 6.54 | 0.006 | 6.55 | 0.006 | 6.55 | 0.006 |

### 5.5.3 Application of the Study Procedure to the Case Study to Mitigate TIs

The study procedure proposed in section (5.4.2) is applied to the test system in Fig. 5.12. When the system is disturbed, growing 16 Hz oscillation was observed in CTG 1 an 20 Hz oscillation was observed in CTG 2. It has to be noted that, since the mechanical damping has been ignored, it's not only these two torsional modes that are unstable, but other torsional modes are likely to be unstable as well. However, CTG 3 did not show any torsional instabilities with regard to its own torsional modes.

As found from the frequency scans behind all generators, there are network resonances at frequencies 16.3 Hz and 20.7 Hz (43.7 Hz and 39.3 Hz in impedance profiles), which are very close to the two excited torsional frequencies. However, 16.3 Hz (43.7 Hz in impedance profile) resonance is not seen at CTG 1 (Fig. 5.13a ) but observed at CTG 2 impedance scans. But, 20.7 Hz resonance is indicated at the CTG 2 impedance profile (Fig. 5.13b).

The critical FSC which corresponds to 20 Hz network frequency was identified as FSCs in either of the branches 6-9 or 4-6 from the previous study. In an attempt to identify whether the inherent damping capability is sufficient to mitigate multiple TIs

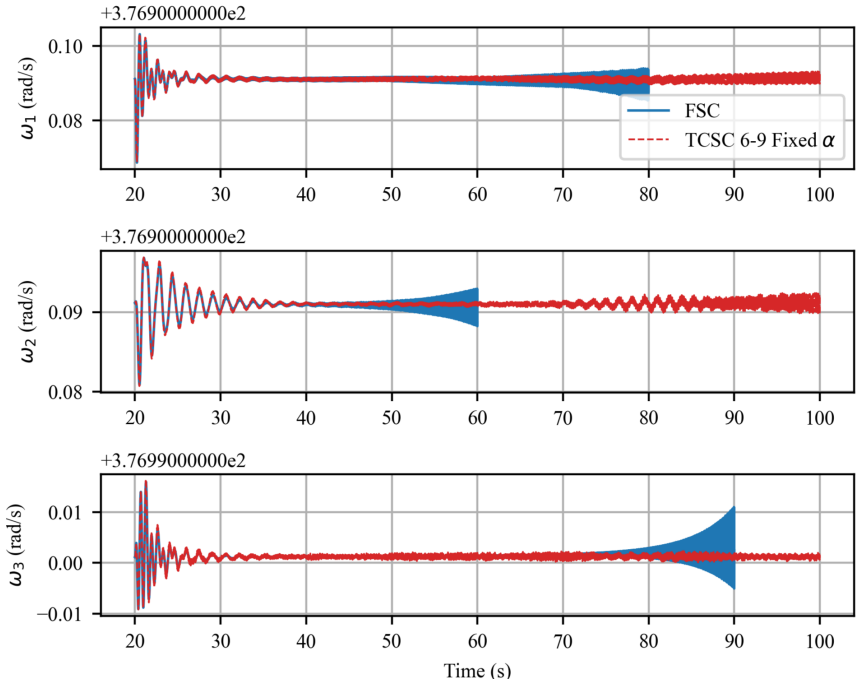


Figure 5.18: EMT simulation results of CTG speed responses following a disturbance with FSC and TCSC at line 6-9 (Fixed firing angle operation)

within the network, a TCSC is designed to replace the FSC in line 6-9 at a boost factor of 1.3 and characteristic factor of 2.5 and operated at fixed firing angle. However, due to the presence of other network resonances spanned over the sub-synchronous frequency range, TI were not fully mitigated as seen from EMT simulation results in Fig. 5.18. The inherent damping nature of the TCSC enhances torsional oscillation damping but does not fully eliminate it in networks with multiple series capacitors. Thus, to guarantee mitigation of multiple torsional instabilities, use of SSDCs must be considered. It should be noted that this system is prepared to demonstrate the worst case scenario by assuming zero mechanical damping. Hence, in practice, with a reasonable level of mechanical damping, the inherent damping capability might be sufficient after thorough analysis and verification.

Moving to the detailed analysis stage, eigenvalue results of the test system with

Table 5.9: Torsional modes of the test system with FSC and TCSC operating with fixed firing angle

| | F(Hz) | FSC | TCSC 6-9 | TCSC 6-9 & 8-6 |
|---|---|---|---|---|
| | | D (%) | D (%) | D (%) |
| G1 | 16.14 | -0.026 | -0.018 | 0.017 |
| | 25.47 | -0.008 | 0.000 | -0.008 |
| | 32.23 | -0.043 | -0.015 | -0.061 |
| | 47.46 | 0 | 0 | 0 |
| G2 | 8.31 | 0.031 | 0.039 | 0.052 |
| | 15.24 | -0.104 | -0.042 | 0.001 |
| | 20.26 | -0.129 | -0.035 | -0.012 |
| | 23.65 | 0 | 0 | 0 |
| G3 | 19.18 | 0.016 | 0.021 | 0.022 |
| | 23.65 | 0.076 | 0.090 | 0.085 |
| | 29.69 | 0.002 | -0.002 | -0.007 |
| | 52.74 | 0 | 0 | 0 |

FSCs, TCSC at 6-9 is shown in Table.5.9. Additionally, the effect of adding another TCSC at 8-6 (FSC at 8-6 is the most contributing FSC to 16.3 Hz network resonance) is also shown in the table. It is seen that most of torsional modes of generator 1 and 2 are unstable with FSCs, and with the addition of TCSCs operating in fixed firing angle control, the torsional instability is not avoided but damping is improved. Having two TCSC at the two locations improve damping of some modes (G2: torsional modes, G1 16 Hz mode) while deteriorating some of generator 1 modes. This is due to the detuning of remaining network resonances. Thus, in networks with multiple network resonances, and CTGs with multiple torsional instabilities, inherent damping capability of the TCSC alone may not be sufficient.

To identify the location of the TCSC with the SSDC to be implemented, controllability indices were assessed for firing angles of TCSCs placed at each location. The most controllable input is then selected as the candidate location for the TCSC to be installed with the SSDC. Additionally, to utilize the maximum inherent damping

capability, the improvement in torsional mode damping is also considered together with the controllability index. The torsional mode damping (due to TCSC's inherent damping) and controllability indices calculated for the above network are given in the Appendix E.2. It was found that unstable torsional modes are most controllable when the TCSC is placed in lines 6-9 or 5-7, However, improvement in the torsional mode damping due to TCSC's inherent damping capability is less when TCSC is at 5-7. Hence, line 6-9 was chosen as the location to install the TCSC and control torsional mode damping through an SSDC.

In order to select the input signal to the SSDC, two signals: speed deviations of CTG 1 and CTG 2 were considered. Since CTG 3 does not indicate torsional instabilities on it's own, speed deviation of it was not considered. The residues of the torsional modes corresponding to speed deviations as outputs are shown in Table 5.10. It can be seen that the residue magnitudes of torsional modes of a generator corresponding to its own speed deviation are non zero, while residues corresponding to speed deviation of the other generator are zero. This is advantageous as it shows that the torsional modes of CTG 1 and CTG 2 can be influenced without affecting those of CTG 3, given that they are already stable. However, it also indicates that its is unlikely to stabilize torsional modes of both generators if one of the speed deviations is considered. It should be noted that, there are some torsional modes such as 47 Hz in CTG1 and 23 Hz in CTG2 which are neither controllable nor observable and hence not considered in the design.

Hence, it is proposed to consider a combination of inputs to the SSDC, considering the residue magnitudes, to stabilize all torsional modes. In this case study, summation of speed deviations of CTG 1 and CTG 2 indicated satisfactory results. Residues

Table 5.10: Residues corresponding to torsional modes of CTGs in the test network

| | F(Hz) | Residues for G1 $\Delta\omega_1$ | | Residues for G2 $\Delta\omega_1$ | | Residues for $\Delta\omega_1 + \Delta\omega_2$ | |
|---|---|---|---|---|---|---|---|
| | | $—R_i—$ | $\angle R_i^0$ | $—R_i—$ | $\angle R_i^0$ | $—R_i—$ | $\angle R_i^0$ |
| G1 | 16.14 | 0.033 | -61.190 | 0. | 107.905 | 0.032 | -60.837 |
| | 25.47 | 0.012 | -88.406 | 0 | 86.647 | 0.012 | -88.366 |
| | 32.23 | 0.032 | -79.433 | 0 | 78.520 | 0.032 | -79.294 |
| | 47.46 | 0 | 73.972 | 0 | -163.604 | 0 | 74.007 |
| G2 | 8.31 | 0 | 125.155 | 0.014 | -51.413 | 0.013 | -51.386 |
| | 15.24 | 0 | -87.072 | 0.015 | -72.703 | 0.016 | -73.424 |
| | 20.26 | 0 | 91.849 | 0.014 | -75.525 | 0.014 | -75.433 |
| | 23.65 | 0 | -110.220 | 0 | -86.796 | 0 | -86.797 |
| G3 | 47.45 | 0 | 114.907 | 0 | -76.429 | 0 | 123.288 |
| | 23.65 | 0 | 129.922 | 0 | 150.115 | 0 | 149.449 |
| | 29.69 | 0 | -149.509 | 0 | -168.689 | 0 | -167.879 |
| | 52.74 | 0 | 4.520 | 0 | -10.853 | 0 | 0.495 |

of the combined output is shown in the same Table 5.10. Note that the residues corresponding to $\Delta\omega_1 + \Delta\omega_2$ are non zero for all unstable torsional modes of generator 1 and 2 and are zero for torsional modes of CTG3. Furthermore, almost all residue angles corresponding to unstable torsional modes lies in the 4th quadrant and hence phase compensation is likely to improve damping of all torsional modes.

Choosing the eigenvalue corresponding to 15.23 Hz torsional mode of generator 2 to be shifted to the left side of the complex plane without changing its frequency, SSDC gain and lead/lag filter time constants were chosen according to (5.7) and (5.8 - 5.10) respectively. An SSDC gain of 2 was adequate to improve the damping of 15.23 Hz torsional mode to 0.18%. Time constants of the lead/lag filter, $T_a$ and $T_b$ are 0.0710 s and 0.0016 s respectively, to achieve a phase lead of $73.42^0$. A washout filter time constant of 5 seconds was considered.

Comparison of torsional modes under different conditions: with FSC, TCSC under fixed firing angle control, TCSC with SSDC using $\Delta\omega_1$ as the input, TCSC with

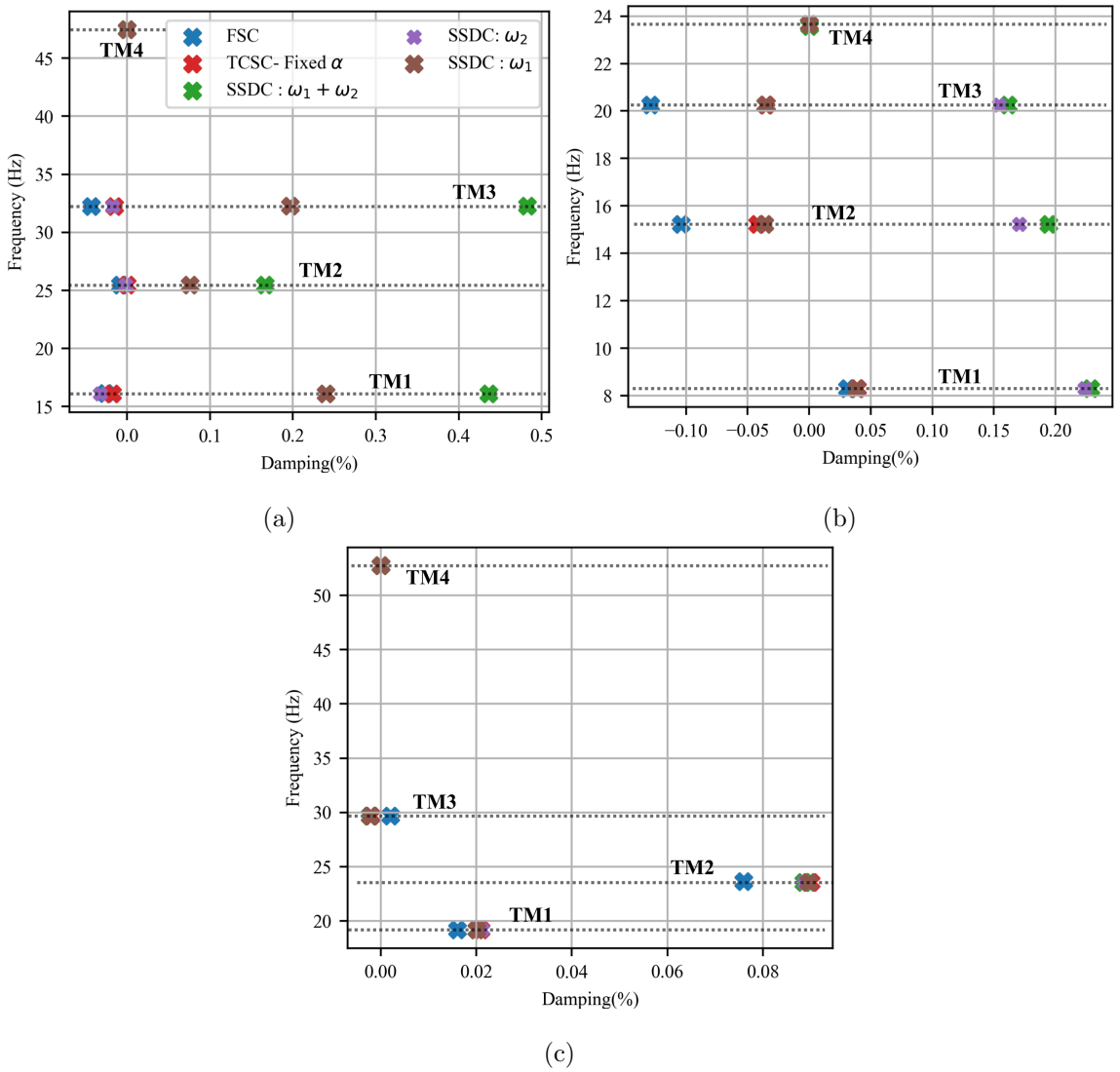


Figure 5.19: Frequency and damping of torsional modes of (a) CTG1, (b) CTG2, and (c) CTG3 with FSC, TCSC operating in open loop, SSDC designed with $\Delta\omega_1$ as the input, SSDC designed with $\Delta\omega_2$ as the input, and SSDC designed with $\Delta\omega_1 + \Delta\omega_2$ as the input

SSDC using $\Delta\omega_2$ as the input, and TCSC with SSDC using $\Delta\omega_1 + \Delta\omega_2$ as the input is illustrated in Fig. 5.19. Note the following observations:

- Replacing FSC in line 6-9 with a TCSC operating with a fixed firing angle has enhanced the damping of torsional modes of CTG 1 (though not enough to

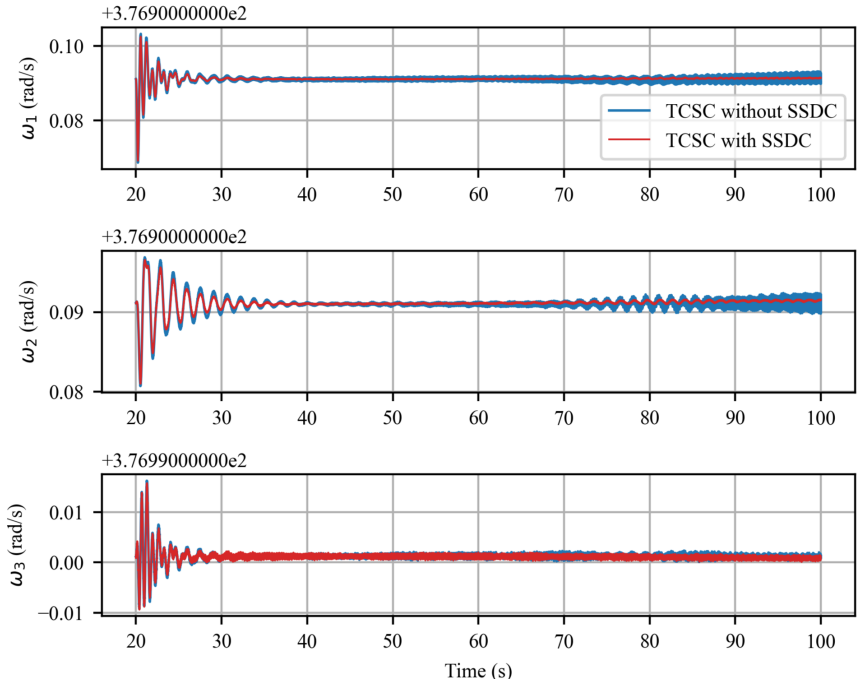


Figure 5.20: EMT simulation results of speed responses of CTGs following a disturbance with and without SSDC

completely mitigate TI), with little effect on the others.

- SSDC designed using the speed deviation of one generator, improves the damping of torsional modes of that specific generator, while the damping of other torsional modes remains unchanged.
- SSDC designed with a combination of $\Delta\omega_1 + \Delta\omega_2$ improves damping of all torsional modes.
- Frequency of torsional modes remains unchanged while damping is improved.
- Torsional modes of CTG 3 is not affected and remains stable.

The designed SSDC was tested in EMT simulations, and Fig. 5.20 presents a comparison of speed responses from the three CTGs after a disturbance, demonstrating

the effectiveness of the SSDC.

## 5.6 Design of Multiple SSDCs

In modern power systems where multiple series compensators are used, multiple SSDCs may be required to damp sub-synchronous oscillations. Coordination of these controllers becomes critical in such scenarios. If the SSDCs are not properly coordinated, they may interact with each other, potentially leading to system instability. In other words, the damping performance of an SSDC must not degrade other oscillation modes within the system. Therefore, designing multiple SSDCs in complex power systems is a challenging task. Additionally, an SSDC may require multiple lead-lag blocks to ensure the damping of various modes over a range of frequencies, further adding to the complexity of the design problem. In such a complex system, the design of SSDCs can be formulated as an optimization problem and solved using appropriate optimization techniques [71], by utilizing the linearized models of the system. The goal is to select optimal controller parameters (SSDC gains and lead-lag block time constants) that ensure effective damping performance across a wide range of oscillation modes.

The design of SSDCs through optimization requires the formulation of an objective function. The objective function can be designed to either re-locate unstable eigenvalues, improve the damping of critical modes, or both [71]. It is essential to carefully select the dominant modes to be included in the objective function. Indices such as controllability, residues, and participation can be useful for this purpose. For instance, by analysing controllability and residues, critical modes that may be

influenced by the selected inputs for SSDCs can be identified.

Once the objective function is formulated, an appropriate optimization technique can be employed for parameter optimization. Heuristic optimization algorithms such as Genetic Algorithms (GA) [72], Particle Swarm Optimization (PSO) [73, 74], and Simulated Annealing (SA) are commonly used for such complex problems where large number of parameters are involved, which increases the complexity of the optimization problem.

With the designed SSDCs, time-domain simulations can be conducted to validate their damping performance. Since SSDCs are designed based on the linear model of the power system, the best practice is to verify the performance using non-linear model simulations for more accurate results.

## 5.7 Conclusions

In networks with multiple series compensated lines, there can be many network resonances which can create IGE or destabilize torsional modes of multiple CTG which are in the vicinity. Replacing all FSCs in a network with TCSCs is not economically viable. A systematic way of addressing IGE and TIs through the use of TCSCs is proposed. The methodology includes a screening stage and a detailed analysis phase. A methodology is proposed in the screening stage to utilize frequency scans to locate critical FSC which contributes the most to the excitation of a critical network resonance. A single frequency scan does not reveal enough information to identify the critical FSC but multiple frequency scans at many locations can identify. The detailed analysis phase comprise of EMT and small-signal stability studies. It is

found that the inherent damping capability of the TCSC is sufficient to avoid IGE in networks with multiple series compensated lines and CTG, if installed at the proper location, without the need for additional damping controllers. The same procedure can be followed in similar networks with multiple Type-3 WPP to mitigate W-SSCIs.

If torsional instabilities of multiple CTG occur due to heavily series compensated networks being in the vicinity, the inherent damping capability alone may not be sufficient to mitigate TIs. This is due to the remaining and detuned network resonances spanning over the sub-synchronous frequency range. Such situations calls for proper SSDCs to be installed along with TCSCs at appropriate locations. The proposed methodology demonstrates choosing the best location for the TCSC with SSDC to be installed while maximally utilizing the inherent damping capability. The design of SSDC is carried out through small-signal stability assessment with the use of eigenproperties. The proposed methodology is applied to a case study of a test network with multiple FSCs and CTGs. It is shown through the case study that torsional instabilities of multiple CTG can be avoided through proper design of a single SSDC on a TCSC. In such cases, it is proposed to use a combination input signals to the SSDC.

# Chapter 6

# Conclusion and Recommendation for Future Work

## 6.1 General Conclusions

A simplified DP model of the TCSC is proposed for small-signal stability assessment of SSR, that accurately captures the inherent characteristics of the TCSC, important for damping SSR. This thesis identifies the requirement of various modelling details in an existing higher order DP model of the TSCC for accurate SSR studies.

The capability of the TCSC in damping SSR in power systems through its inherent damping capability is evaluated in this thesis. The types of SSR analysed in this thesis include Induction Generator Effect and Torsional Interactions which occur in systems with Series Compensated lines and Conventional Turbine Generators, and Wind -Sub-Synchronous Controller Interactions with Type-3 Wind Power

Plants. This thesis proposes the use of a simplified Dynamic Phasor model of the TCSC for small signal stability assessment of SSR. The simplified DP model contains only the dynamics of the fundamental frequency component. It can be readily integrated with Dynamic phasor models of other power system components, making it straightforward to implement in commercial dynamic phasor based small-signal stability analysis software. The simplified model has been used to evaluate the inherent damping capability of the TCSC in mitigating IGE, TI and W-SSCI through small-signal stability assessment. This thesis also proposes a procedure to utilize TCSCs to mitigate IGE and TI in heavily series compensated networks with multiple Conventional Turbine Generators. The procedure comprise of a screening stage followed by a detailed analysis phase.

Linearized model development of power system components for the analysis of SSR is discussed in Chapter 2 and the models are validated against EMT simulations in Chapter 3. The linearized models showed a good agreement with EMT simulation. A simplified simplified DP model of the TCSC is proposed for SSR analysis. This thesis identifies the requirement of various modelling details in an existing higher order DP model of the TSCC for accurate studies of SSR and based on these findings, corresponding simplifications of the higher order TCSC model are implemented. The simplified linearized model of the TCSC is validated against EMT simulations.

Evaluation of the inherent damping capability of the TCSC using the simplified DP model of the TCSC is presented in Chapter 3. When the series compensation is fully achieved with a TCSC operating at a fixed firing angle, the network resonance appears in a very narrow range of it's operating points. The network resonance is seen when the TCSC is operating very close to a boost factor of 1(almost a FSC) and

disappears at high boost factors, eliminating the root cause for IGE, TI and W-SSCI phenomena. Furthermore, the network resonant mode is well damped compared to that with an FSC even in the region where the network resonance exist, due to the resistive nature of the TCSC.

The design parameters of the TCSC, particularly the boost factor and the proportion/level of TCSC out of the total compensation impacts the inherent damping capability of the TCSC. When the TCSC is used along with an FSC, the network resonance exist. However, the inherent damping capability of the TCSC is sufficient to avoid IGE even with low levels of TCSC with proper choice of its design parameters. Furthermore, it is also shown that the inherent damping capability of the TCSC is also sufficient to avoid W-SSCI problems between Type-3 WPP and series compensated network. Both IGE and W-SSCI is caused due to negatively damped network resonance. The resistive-inductive nature of the TCSC in the sub-synchronous frequency range can mitigate these phenomena even without additional damping controllers.

However, low levels of TCSC cannot guarantee mitigation of TI through its inherent damping capability. This is due to the presence of detuned network resonance when the TCSC is used along with an FSC. Even though the TCSC presents a resistive nature at sub-synchronous frequencies, TI can still occur if the mechanical damping of the system is low. Therefore, SSDCs are required at low levels of TCSC to guarantee mitigation of TI. If the FSC is fully replaced with a TCSC designed at a proper boost factor (possibly high boost factors of beyond 1.2), operation beyond its designed boost factor can avoid TI through its inherent damping capability. Hence, the TCSC must be designed to provide the required minimum compensation level at an appropriate boost factor to prevent operation below its designed boost

factor. Otherwise, a minimum operational boost factor must be determined through a small-signal stability studies, to prevent operation at low boost factors, which can guarantee mitigation of TI. Additionally, the ability of the TCSC to shift the network resonance when used along with an FSC is advantageous in shifting the network resonances away from torsional frequencies, which eventually improves the damping of torsional modes.

At high levels of TCSC and high boost factors, damping of the electromechanical mode degrades when the TCSC is operated in fixed firing angle control. This is improved with closed loop primary current controls, allowing high levels of TCSC and boost factors to be achieved, which helps in the mitigation of TI. It is shown that torsional mode damping is sensitive to TCSC current controller gains. But, the purpose of primary controls of the TCSC is not to add damping to SSR conditions and are not particularly designed to do so. Therefore, the damping contributed by the primary controls is also regarded as part of the inherent damping characteristics of the TCSC.

A procedure to utilize TCSCs to mitigate IGE and TI in networks with multiple series capacitors and multiple CTG is developed in Chapter 5. In such networks, there can be many network resonances which can cause IGE or destabilize torsional modes of multiple CTG. The procedure is proposed to locate the best location to place the TCSC to avoid SSR conditions. Furthermore, a methodology is proposed to utilize frequency scans at the screening stage to identify critical FSC which contributes the most to the excitation of a critical network resonance. Upon the identification of the location of the critical FSC, detailed analysis has to be carried out to determine the appropriate level of TCSC to be installed or to design appropriate sub-synchronous

damping controllers. It is shown through a case study that IGE in a multiple series compensated system can be avoided through the inherent damping capability of the TCSC by placing it at the right location. However, to avoid multiple torsional mode instabilities of multiple CTG, the inherent damping capability alone is insufficient. Use of SSDCs is a more economical solution in such situations than replacing more FSC with TCSCs operating without additional damping controllers. The location of the TCSC is chosen to maximally utilize the inherent damping capability and to provide additional damping through the SSDC. To damp multiple torsional mode instabilities in heavily series compensated networks, it is proposed to consider combinations of input signals to the SSDC.

## 6.2 Contributions

The main contributions of this thesis are presented below.

- Developed a simplified small-signal dynamic phasor model of the TCSC for the analysis of SSR. Identified that that the dynamics of higher-order harmonics are not critical to the inherent characteristics of the TCSC that are important for SSR, while it is crucial to model the transient phase shift associated with fundamental components. The adequacy of the simplified small-signal dynamic phasor model and the accurate representation of the inherent damping nature is validated for sub-synchronous frequencies.

- Evaluated the inherent damping capability of the TCSC in mitigating different SSR phenomena. The adequacy of the inherent damping capability to mitigate IGE, TIs and W-SSCIs is determined and the need for additional damping

controllers is identified.

- Identified the impact of TCSC parameters on the inherent damping capability and recommendations are provided to achieve better damping with the TCSC to avoid IGE and TIs. Small-signal stability assessment is proposed to design the TCSC parameters in order to maximise its inherent damping capability.

- Developed a methodology to identify the critical FSC which contributes the most to the excitation of critical network resonances in multiple series compensated networks.

- Proposed a procedure to utilize TCSCs to mitigate IGE and TIs in heavily series compensated networks. The proposed procedure to address IGE issues is also applicable for W-SSCI problems as well. Designed Sub-synchronous Damping Controllers to damp multiple torsional mode instabilities of multiple CTG while maximally utilizing inherent damping capability in multiple series compensated networks.

The contributions of this work have led to the following publications:

- D. R. Weerakoon, C. Karawita and U. D. Annakkage, "Evaluation of Inherent Damping Introduced by Thyristor Controlled Series Compensators", IEEE Open Access Journal of Power and Energy 10, Feb 2023, pp 259-269.

- D. R. Weerakoon, U. D. Annakkage and C. Karawita, "Damping of Sub-Synchronous Resonance by placing Thyristor Controlled Series Compensators (TCSC)", CIGRE Canada, Oct/Nov. 2022.

- D. R. Weerakoon, U. D. Annakkage and C. Karawita, "A Review on Sub-Synchronous Resonance Damping with Thyristor Controlled Series Compensators", Journal of Advances in Engineering and Technology, Vol. 01, no 02, pp 24-34, 2023.

- D. R. Weerakoon, U. D. Annakkage and C. Karawita, "Analysis of Sub Synchronous Resonant Modes in Series Compensated Networks Using Multiple Frequency Scans", CIGRE Toronto, Oct.19-22, 2020.

Publications in progress:

- D. R. Weerakoon, C. Karawita, D. H. R. Suriyaarachchi and U. D. Annakkage, "Thyristor Controlled Series Compensators to Mitigate Wind-Sub Synchronous Controller Interactions," CIGRE Canada (Paper Submitted).

Contributions to CIGRE Technical Brochure:

- "Guidelines for Subsynchronous Oscillation Studies in Power Electronics Dominated Power Systems", TB 909, CIGRE, 2023.
  Contributions are related to screening for potential SSO risk and requirement of TCSCs for mitigation of SSO.

## 6.3 Recommendations for Future Work

- Design parameters of the TCSC governs the size and rating of it and eventually the cost of the TCSC. Therefore, when the location of the TCSC is decided, the process of determining the TCSC design parameters could be enhanced by transforming it into an optimization problem that incorporates the economic

considerations of TCSCs. Given that TCSCs are generally more expensive than FSC, finding optimal TCSC design parameters while minimizing costs would be advantageous for utilities before committing to an investment. Linearized models can be utilized for this optimization. Furthermore, Artificial Intelligence (AI) algorithms can be applied to select the optimal location for the TCSC and its parameters.

- The heavily series compensated network examined in this case study includes only CTGs. However, networks with a combination of WPPs, CTGs, and other dynamic devices near FSC concentrated network areas are seen in practical systems. Exploring the interactions when CTGs and WPPs are both nearby and investigating how TCSCs can address such challenges would be interesting.

- The modern power system is complex with many power electronic interfaces and FACTS devices. With multiple series compensators in the system, multiple SSDCs may be required. Design of one or more optimal SSDCs for maximal damping will become challenging in such systems. Linearized models developed in this thesis can be utilized to address this challenge by formulating it as an optimization problem.

# Appendix A

# Linearized Model of the TCSC

State equations of the TCSC are,

$$\frac{dV_{1R}}{dt} = \frac{I_{L_{1R}}}{C} - \frac{I_{1R}}{C} + \omega_0 V_{1I} \tag{A.1}$$

$$\frac{dV_{1I}}{dt} = \frac{I_{L_{1I}}}{C} - \frac{I_{1I}}{C} - \omega_0 V_{1R} \tag{A.2}$$

$$\frac{dI_{1R}}{dt} = \frac{\langle qv \rangle_{1R}}{L} + \omega_0 I_{1I} \tag{A.3}$$

$$\frac{dI_{1I}}{dt} = \frac{\langle qv \rangle_{1I}}{L} - \omega_0 I_{1R} \tag{A.4}$$

where,

$$\langle q \rangle_{1R} = V_{3R}(q_{4R} + q_{2R}) + V_{3I}(q_{4I} + q_{2I}) + V_{5R}(q_{6R} + q_{4R}) + V_{5I}(q_{6I} + q_{4I}) +$$
$$V_{1R}(q_{2R} + q_0) + V_{1I}(q_{2I})$$

$$\langle q \rangle_{1I} = V_{3R}(q_{4I} - q_{2I}) + V_{3I}(-q_{4R} + q_{2R}) + V_{5R}(q_{6I} - q_{4I}) + V_{5I}(-q_{6R} + q_{4R}) +$$
$$V_{1R}(q_{2I}) + V_{1I}(-q_{2R} + q_0)$$

Higher order harmonic components of the TCSC voltage are treated as algebraic variables. Therefore, the algebraic equations of the TCSC are,

$$0 = V_{3R}(q_{6R} + q_0 - 9LC\omega_0^2) + V_{3I}(q_{6I}) + V_{5R}(q_{8R} + q_{2R}) + V_{5I}(q_{8I} + q_{2I}) +$$
$$V_{1R}(q_{4R} + q_{2R}) + V_{1I}(q_{4I} - q_{2I}) \tag{A.5}$$

$$0 = V_{3R}(q_{6I}) + V_{3I}(-q_{6R} + q_0 - 9LC\omega_0^2) + V_{5R}(q_{8I} - q_{2I}) + V_{5I}(-q_{8R} + q_{2R}) +$$
$$V_{1R}(q_{4I} + q_{2I}) + V_{1I}(q_{2R} - q_{4R}) \tag{A.6}$$

$$0 = V_{3R}(q_{8R} + q_{2R}) + V_{3I}(q_{8I} - q_{2I}) + V_{5R}(q_{10R} + q_0 - 25LC\omega_0^2) + V_{5I}(q_{10I}) +$$
$$V_{1R}(q_{6R} + q_{4R}) + V_{1I}(q_{6I} - q_{4I}) \tag{A.7}$$

$$0 = V_{3R}(q_{8I} + q_{2I}) + V_{3I}(-q_{8R} + q_{2R}) + V_{5R}(q_{10I}) + V_{5I}(-q_{10R} + q_0 - 25LC\omega_0^2) +$$
$$V_{1R}(q_{6I} + q_{4I}) + V_{1I}(q_{4R} - q_{6R}) \tag{A.8}$$

where,

$$q_{kR} = \frac{2}{k\pi}\sin\left(\frac{k\sigma}{2}\right)\cos(k(\zeta+\phi)) \qquad q_{kI} = -\frac{2}{k\pi}\sin\left(\frac{k\sigma}{2}\right)\sin(k(\zeta+\phi))$$
$$q_0 = \frac{\sigma}{\pi} \qquad for \qquad k = 2,4,6,8,10$$

From (2.23) and (2.43),

$$\sigma = 2(\frac{\pi}{2} + \delta_m - \alpha + \angle - I_1^*) \qquad \zeta + \phi = \angle - I_1^*$$

Hence,

$$q_{kR/I} = f(\alpha, \delta_m, I_{1R}, I_{1I})$$

To derive the complete state space model of the TCSC, linearized state equations (A.1-A.4) and algebraic equations (A.5-A.8) can expressed as in (A.9) and (A.10) respectively.

$$\mathbf{\Delta\dot{x}_{tcsc}} = \mathbf{A_1\Delta x_{tcsc}} + \mathbf{B_1\Delta u_{tcsc}} + \mathbf{H_1\Delta w_{tcsc}} + \mathbf{C_1\Delta Z_{tcsc}} \tag{A.9}$$

$$0 = \mathbf{D_1\Delta x_{tcsc}} + \mathbf{E_1\Delta u_{tcsc}} + \mathbf{F_1\Delta w_{tcsc}} + \mathbf{G_1\Delta z_{tcsc}} \tag{A.10}$$

where,

$$\mathbf{\Delta x_{tcsc}} = [\Delta V_{1R}, \Delta V_{1I}, \Delta I_{1R}, \Delta I_{1I}]^T \qquad \mathbf{\Delta u_{tcsc}} = [\Delta\alpha]$$

$$\mathbf{\Delta w_{tcsc}} = [\Delta I_{L_{1R}}, \Delta I_{L_{1I}}, \Delta\delta_m]^T \qquad \mathbf{\Delta z_{tcsc}} = [\Delta V_{3R}, \Delta V_{3I}, \Delta V_{5R}, \Delta V_{5I}]^T$$

Eliminating the higher order algebraic terms from (A.9) and (A.10) will result in the complete state space model of the TCSC,

$$\mathbf{\Delta\dot{x}_{tcsc}} = \mathbf{A_{tcsc}\Delta x_{tcsc}} + \mathbf{B_{tcsc}\Delta u_{tcsc}} + \mathbf{H_{tcsc}\Delta w_{tcsc}}$$

where,

$$\mathbf{A_{tcsc}} = \mathbf{A_1} - \mathbf{C_1}{\mathbf{G_1}}^{-1}\mathbf{D_1}$$

$$\mathbf{B_{tcsc}} = \mathbf{B_1} - \mathbf{C_1}{\mathbf{G_1}}^{-1}\mathbf{E_1}$$

$$\mathbf{H_{tcsc}} = \mathbf{H_1} - \mathbf{C_1}{\mathbf{G_1}}^{-1}\mathbf{F_1}$$

Elements of matrix $\mathbf{A_1}$ are,

$$\mathbf{A_1}(1,2) = \omega_0 \qquad \mathbf{A_1}(2,1) = -\omega_0$$

$$\mathbf{A_1}(3,1) = \frac{1}{L}(q^0_{2R} + q^0_0) \qquad \mathbf{A_1}(3,2) = \frac{1}{L}(q^0_{2I})$$

$$\mathbf{A_1}(3,3) = \frac{1}{L}\left[\begin{array}{c}\left[\begin{array}{cccc}\left(\frac{\partial q^0_{4R}}{\partial I_{1R}} + \frac{\partial q^0_{2R}}{\partial I_{1R}}\right) & \left(\frac{\partial q^0_{4I}}{\partial I_{1R}} + \frac{\partial q^0_{2I}}{\partial I_{1R}}\right) & \left(\frac{\partial q^0_{6R}}{\partial I_{1R}} + \frac{\partial q^0_{4R}}{\partial I_{1R}}\right) & \left(\frac{\partial q^0_{6I}}{\partial I_{1R}} + \frac{\partial q^0_{4I}}{\partial I_{1R}}\right)\end{array}\right]V^0_{35} \\ +\left[\begin{array}{cc}\left(\frac{\partial q^0_0}{\partial I_{1R}} + \frac{\partial q^0_{2R}}{\partial I_{1R}}\right) & \left(\frac{\partial q^0_{2I}}{\partial I_{1R}}\right)\end{array}\right]\end{array}\right]\left[\begin{array}{c}V^0_{1R}\\ V^0_{1I}\end{array}\right]$$

$$\mathbf{A_1}(3,4) = \frac{1}{L}\left[\begin{array}{c}\left[\begin{array}{cccc}\left(\frac{\partial q^0_{4R}}{\partial I_{1I}} + \frac{\partial q^0_{2R}}{\partial I_{1I}}\right) & \left(\frac{\partial q^0_{4I}}{\partial I_{1I}} + \frac{\partial q^0_{2I}}{\partial I_{1I}}\right) & \left(\frac{\partial q^0_{6R}}{\partial I_{1I}} + \frac{\partial q^0_{4R}}{\partial I_{1I}}\right) & \left(\frac{\partial q^0_{6I}}{\partial I_{1I}} + \frac{\partial q^0_{4I}}{\partial I_{1I}}\right)\end{array}\right]V^0_{35} \\ +\left[\begin{array}{cc}\left(\frac{\partial q^0_0}{\partial I_{1I}} + \frac{\partial q^0_{2R}}{\partial I_{1I}}\right) & \left(\frac{\partial q^0_{2I}}{\partial I_{1I}}\right)\end{array}\right]\end{array}\right]\left[\begin{array}{c}V^0_{1R}\\ V^0_{1I}\end{array}\right] + \omega_0$$

$$\mathbf{A_1}(4,1) = \frac{1}{L}(q^0_{2I}) \qquad \mathbf{A_1}(4,2) = \frac{1}{L}(-q^0_{2R} + q^0_0)$$

$$\mathbf{A_1}(4,3) = \frac{1}{L}\left[\begin{array}{c}\left[\begin{array}{cccc}\left(\frac{\partial q^0_{4I}}{\partial I_{1R}} - \frac{\partial q^0_{2I}}{\partial I_{1R}}\right) & \left(\frac{\partial q^0_{2R}}{\partial I_{1R}} - \frac{\partial q^0_{4R}}{\partial I_{1R}}\right) & \left(\frac{\partial q^0_{6I}}{\partial I_{1R}} - \frac{\partial q^0_{4I}}{\partial I_{1R}}\right) & \left(\frac{\partial q^0_{4R}}{\partial I_{1R}} - \frac{\partial q^0_{6R}}{\partial I_{1R}}\right)\end{array}\right]V^0_{35} \\ +\left[\begin{array}{cc}\left(\frac{\partial q^0_{2I}}{\partial I_{1R}}\right) & \left(\frac{\partial q^0_0}{\partial I_{1R}} - \frac{\partial q^0_{2R}}{\partial I_{1R}}\right)\end{array}\right]\end{array}\right]\left[\begin{array}{c}V^0_{1R}\\ V^0_{1I}\end{array}\right]$$

$$-\omega_0$$

$$\mathbf{A_1}(4,4) = \frac{1}{L}\left[\begin{array}{c}\left[\begin{array}{cccc}\left(\frac{\partial q^0_{4I}}{\partial I_{1I}} - \frac{\partial q^0_{2I}}{\partial I_{1I}}\right) & \left(\frac{\partial q^0_{2R}}{\partial I_{1I}} - \frac{\partial q^0_{4R}}{\partial I_{1I}}\right) & \left(\frac{\partial q^0_{6I}}{\partial I_{1I}} - \frac{\partial q^0_{4I}}{\partial I_{1I}}\right) & \left(\frac{\partial q^0_{4R}}{\partial I_{1I}} - \frac{\partial q^0_{6R}}{\partial I_{1I}}\right)\end{array}\right]V^0_{35} \\ +\left[\begin{array}{cc}\left(\frac{\partial q^0_{2I}}{\partial I_{1I}}\right) & \left(\frac{\partial q^0_0}{\partial I_{1I}} - \frac{\partial q^0_{2R}}{\partial I_{1I}}\right)\end{array}\right]\end{array}\right]\left[\begin{array}{c}V^0_{1R}\\ V^0_{1I}\end{array}\right]$$

Elements of matrix $\mathbf{B_1}$ are,

$$\mathbf{B_1}(3,1) = \frac{1}{L}\left[\begin{array}{c}\left[\begin{array}{cccc}\left(\frac{\partial q^0_{4R}}{\partial \alpha} + \frac{\partial q^0_{2R}}{\partial \alpha}\right) & \left(\frac{\partial q^0_{4I}}{\partial \alpha} + \frac{\partial q^0_{2I}}{\partial \alpha}\right) & \left(\frac{\partial q^0_{6R}}{\partial \alpha} + \frac{\partial q^0_{4R}}{\partial \alpha}\right) & \left(\frac{\partial q^0_{6I}}{\partial \alpha} + \frac{\partial q^0_{4I}}{\partial \alpha}\right)\end{array}\right]V^0_{35} \\ +\left[\begin{array}{cc}\left(\frac{\partial q^0_0}{\partial \alpha} + \frac{\partial q^0_{2R}}{\partial \alpha}\right) & \left(\frac{\partial q^0_{2I}}{\partial \alpha}\right)\end{array}\right]\end{array}\right]\left[\begin{array}{c}V^0_{1R}\\ V^0_{1I}\end{array}\right]$$

$$\mathbf{B_1}(4,1) = \frac{1}{L}\left[\begin{array}{c}\left[\begin{array}{cccc}\left(\frac{\partial q^0_{4I}}{\partial \alpha} - \frac{\partial q^0_{2I}}{\partial \alpha}\right) & \left(\frac{\partial q^0_{2R}}{\partial \alpha} - \frac{\partial q^0_{4R}}{\partial \alpha}\right) & \left(\frac{\partial q^0_{6I}}{\partial \alpha} - \frac{\partial q^0_{4I}}{\partial \alpha}\right) & \left(\frac{\partial q^0_{4R}}{\partial \alpha} - \frac{\partial q^0_{6R}}{\partial \alpha}\right)\end{array}\right]V^0_{35} \\ +\left[\begin{array}{cc}\left(\frac{\partial q^0_{2I}}{\partial \alpha}\right) & \left(\frac{\partial q^0_0}{\partial \alpha} - \frac{\partial q^0_{2R}}{\partial \alpha}\right)\end{array}\right]\end{array}\right]\left[\begin{array}{c}V^0_{1R}\\ V^0_{1I}\end{array}\right]$$

Elements of matrix $\mathbf{H_1}$ are,

$$\mathbf{H_1}(1,1) = \frac{1}{C} \qquad \mathbf{H_1}(2,2) = \frac{1}{C}$$

$$\mathbf{H_1}(3,3) = \frac{1}{L}\left[\begin{array}{c}\left[\begin{array}{cccc}\left(\frac{\partial q^0_{4R}}{\partial \delta_m} + \frac{\partial q^0_{2R}}{\partial \delta_m}\right) & \left(\frac{\partial q^0_{4I}}{\partial \delta_m} + \frac{\partial q^0_{2I}}{\partial \delta_m}\right) & \left(\frac{\partial q^0_{6R}}{\partial \delta_m} + \frac{\partial q^0_{4R}}{\partial \delta_m}\right) & \left(\frac{\partial q^0_{6I}}{\partial \delta_m} + \frac{\partial q^0_{4I}}{\partial \delta_m}\right)\end{array}\right]V^0_{35} \\ +\left[\begin{array}{cc}\left(\frac{\partial q^0_0}{\partial \delta_m} + \frac{\partial q^0_{2R}}{\partial \delta_m}\right) & \left(\frac{\partial q^0_{2I}}{\partial \delta_m}\right)\end{array}\right]\end{array}\right]\left[\begin{array}{c}V^0_{1R}\\ V^0_{1I}\end{array}\right]$$

$$\mathbf{H_1}(4,3) = \frac{1}{L}\left[\begin{array}{c}\left[\begin{array}{cccc}\left(\frac{\partial q^0_{4I}}{\partial \delta_m} - \frac{\partial q^0_{2I}}{\partial \delta_m}\right) & \left(\frac{\partial q^0_{2R}}{\partial \delta_m} - \frac{\partial q^0_{4R}}{\partial \delta_m}\right) & \left(\frac{\partial q^0_{6I}}{\partial \delta_m} - \frac{\partial q^0_{4I}}{\partial \delta_m}\right) & \left(\frac{\partial q^0_{4R}}{\partial \delta_m} - \frac{\partial q^0_{6R}}{\partial \delta_m}\right)\end{array}\right]V^0_{35} \\ +\left[\begin{array}{cc}\left(\frac{\partial q^0_{2I}}{\partial \delta_m}\right) & \left(\frac{\partial q^0_0}{\partial \delta_m} - \frac{\partial q^0_{2R}}{\partial \delta_m}\right)\end{array}\right]\end{array}\right]\left[\begin{array}{c}V^0_{1R}\\ V^0_{1I}\end{array}\right]$$

Elements of matrix $\mathbf{C_1}$ are,

$$\mathbf{C_1}(3,1) = \frac{1}{L}(q^0_{4R} + q^0_{2R}) \quad \mathbf{C_1}(3,2) = \frac{1}{L}(q^0_{4I} + q^0_{2I}) \qquad \mathbf{C_1}(3,3) = \frac{1}{L}(q^0_{6R} + q^0_{4R})$$

$$\mathbf{C_1}(3,4) = \frac{1}{L}(q^0_{6I} + q^0_{4I}) \quad \mathbf{C_1}(4,1) = \frac{1}{L}(q^0_{4I} - q^0_{2I}) \qquad \mathbf{C_1}(4,2) = \frac{1}{L}(-q^0_{4R} + q^0_{2R})$$

$$\mathbf{C_1}(4,3) = \frac{1}{L}(q^0_{6I} - q^0_{4I}) \quad \mathbf{C_1}(4,4) = \frac{1}{L}(-q^0_{6R} + q^0_{4R})$$

Elements of matrix $\mathbf{D_1}$ are,

$$\mathbf{D_1}(1,1) = q^0_{4R} + q^0_{2R}$$

$$\mathbf{D_1}(1,2) = q^0_{4I} - q^0_{2I}$$

$$\mathbf{D_1}(1,3) = \begin{bmatrix} \left[ \begin{array}{cccc} \left(\frac{\partial q^0_{6R}}{\partial I_{1R}} + \frac{\partial q^0_0}{\partial I_{1R}}\right) & \left(\frac{\partial q^0_{6I}}{\partial I_{1R}}\right) & \left(\frac{\partial q^0_{8R}}{\partial I_{1R}} + \frac{\partial q^0_{2R}}{\partial I_{1R}}\right) & \left(\frac{\partial q^0_{8I}}{\partial I_{1R}} + \frac{\partial q^0_{2I}}{\partial I_{1R}}\right) \end{array} \right] V^0_{35} \\ + \left[ \begin{array}{cc} \left(\frac{\partial q^0_{4R}}{\partial I_{1R}} + \frac{\partial q^0_{2R}}{\partial I_{1R}}\right) & \left(\frac{\partial q^0_{4I}}{\partial I_{1R}} - \frac{\partial q^0_{2I}}{\partial I_{1R}}\right) \end{array} \right] \end{bmatrix} \begin{bmatrix} V^0_{1R} \\ V^0_{1I} \end{bmatrix}$$

$$\mathbf{D_1}(1,4) = \begin{bmatrix} \left[ \begin{array}{cccc} \left(\frac{\partial q^0_{6R}}{\partial I_{1I}} + \frac{\partial q^0_0}{\partial I_{1I}}\right) & \left(\frac{\partial q^0_{6I}}{\partial I_{1I}}\right) & \left(\frac{\partial q^0_{8R}}{\partial I_{1I}} + \frac{\partial q^0_{2R}}{\partial I_{1I}}\right) & \left(\frac{\partial q^0_{8I}}{\partial I_{1I}} + \frac{\partial q^0_{2I}}{\partial I_{1I}}\right) \end{array} \right] V^0_{35} \\ + \left[ \begin{array}{cc} \left(\frac{\partial q^0_{4R}}{\partial I_{1I}} + \frac{\partial q^0_{2R}}{\partial I_{1I}}\right) & \left(\frac{\partial q^0_{4I}}{\partial I_{1I}} - \frac{\partial q^0_{2I}}{\partial I_{1I}}\right) \end{array} \right] \end{bmatrix} \begin{bmatrix} V^0_{1R} \\ V^0_{1I} \end{bmatrix}$$

$$\mathbf{D_1}(2,1) = q^0_{4I} + q^0_{2I}$$

$$\mathbf{D_1}(2,2) = q^0_{2R} - q^0_{4R}$$

$$\mathbf{D_1}(2,3) = \begin{bmatrix} \left[ \begin{array}{cccc} \left(\frac{\partial q^0_{6I}}{\partial I_{1R}}\right) & \left(\frac{\partial q^0_0}{\partial I_{1R}} - \frac{\partial q^0_{6R}}{\partial I_{1R}}\right) & \left(\frac{\partial q^0_{8I}}{\partial I_{1R}} - \frac{\partial q^0_{2I}}{\partial I_{1R}}\right) & \left(\frac{\partial q^0_{2R}}{\partial I_{1R}} - \frac{\partial q^0_{8R}}{\partial I_{1R}}\right) \end{array} \right] V^0_{35} \\ + \left[ \begin{array}{cc} \left(\frac{\partial q^0_{4I}}{\partial I_{1R}} + \frac{\partial q^0_{2I}}{\partial I_{1R}}\right) & \left(\frac{\partial q^0_{2R}}{\partial I_{1R}} - \frac{\partial q^0_{4R}}{\partial I_{1R}}\right) \end{array} \right] \end{bmatrix} \begin{bmatrix} V^0_{1R} \\ V^0_{1I} \end{bmatrix}$$

$$\mathbf{D_1}(2,4) = \begin{bmatrix} \left[ \begin{array}{cccc} \left(\frac{\partial q^0_{6I}}{\partial I_{1I}}\right) & \left(\frac{\partial q^0_0}{\partial I_{1I}} - \frac{\partial q^0_{6R}}{\partial I_{1I}}\right) & \left(\frac{\partial q^0_{8I}}{\partial I_{1I}} - \frac{\partial q^0_{2I}}{\partial I_{1I}}\right) & \left(\frac{\partial q^0_{2R}}{\partial I_{1I}} - \frac{\partial q^0_{8R}}{\partial I_{1I}}\right) \end{array} \right] V^0_{35} \\ + \left[ \begin{array}{cc} \left(\frac{\partial q^0_{4I}}{\partial I_{1I}} + \frac{\partial q^0_{2I}}{\partial I_{1I}}\right) & \left(\frac{\partial q^0_{2R}}{\partial I_{1I}} - \frac{\partial q^0_{4R}}{\partial I_{1I}}\right) \end{array} \right] \end{bmatrix} \begin{bmatrix} V^0_{1R} \\ V^0_{1I} \end{bmatrix}$$

$$\mathbf{D_1}(3,1) = q^0_{6R} + q^0_{4R}$$

$$\mathbf{D_1}(3,2) = q^0_{6I} - q^0_{4I}$$

$$\mathbf{D_1}(3,3) = \begin{bmatrix} \left[ \begin{array}{cccc} \left(\frac{\partial q^0_{8R}}{\partial I_{1R}} + \frac{\partial q^0_{2R}}{\partial I_{1R}}\right) & \left(\frac{\partial q^0_{8I}}{\partial I_{1R}} - \frac{\partial q^0_{2I}}{\partial I_{1R}}\right) & \left(\frac{\partial q^0_{10R}}{\partial I_{1R}} + \frac{\partial q^0_0}{\partial I_{1R}}\right) & \left(\frac{\partial q^0_{10I}}{\partial I_{1R}}\right) \end{array} \right] V^0_{35} \\ + \left[ \begin{array}{cc} \left(\frac{\partial q^0_{6R}}{\partial I_{1R}} + \frac{\partial q^0_{4R}}{\partial I_{1R}}\right) & \left(\frac{\partial q^0_{6I}}{\partial I_{1R}} - \frac{\partial q^0_{4I}}{\partial I_{1R}}\right) \end{array} \right] \end{bmatrix} \begin{bmatrix} V^0_{1R} \\ V^0_{1I} \end{bmatrix}$$

$$\mathbf{D_1}(3,4) = \begin{bmatrix} \left[ \begin{array}{cccc} \left(\frac{\partial q^0_{8R}}{\partial I_{1I}} + \frac{\partial q^0_{2R}}{\partial I_{1I}}\right) & \left(\frac{\partial q^0_{8I}}{\partial I_{1I}} - \frac{\partial q^0_{2I}}{\partial I_{1I}}\right) & \left(\frac{\partial q^0_{10R}}{\partial I_{1I}} + \frac{\partial q^0_0}{\partial I_{1I}}\right) & \left(\frac{\partial q^0_{10I}}{\partial I_{1I}}\right) \end{array} \right] V^0_{35} \\ + \left[ \begin{array}{cc} \left(\frac{\partial q^0_{6R}}{\partial I_{1I}} + \frac{\partial q^0_{4R}}{\partial I_{1I}}\right) & \left(\frac{\partial q^0_{6I}}{\partial I_{1I}} - \frac{\partial q^0_{4I}}{\partial I_{1I}}\right) \end{array} \right] \end{bmatrix} \begin{bmatrix} V^0_{1R} \\ V^0_{1I} \end{bmatrix}$$

$$\mathbf{D_1}(4,1) = q^0_{6I} + q^0_{4I}$$

$$\mathbf{D_1}(4,2) = q^0_{4R} - q^0_{6R}$$

$$\mathbf{D_1}(4,3) = \begin{bmatrix} \left[\begin{array}{cccc} \left(\frac{\partial q^0_{8I}}{\partial I_{1R}} + \frac{\partial q^0_{2I}}{\partial I_{1R}}\right) & \left(\frac{\partial q^0_{2R}}{\partial I_{1R}} - \frac{\partial q^0_{8R}}{\partial I_{1R}}\right) & \left(\frac{\partial q^0_{10I}}{\partial I_{1R}}\right) & \left(\frac{\partial q^0_{0}}{\partial I_{1R}} - \frac{\partial q^0_{10R}}{\partial I_{1R}}\right) \end{array}\right] V^0_{35} \\ + \left[\begin{array}{cc} \left(\frac{\partial q^0_{6I}}{\partial I_{4I}} + \frac{\partial q^0_{2R}}{\partial I_{1R}}\right) & \left(\frac{\partial q^0_{4R}}{\partial I_{1R}} - \frac{\partial q^0_{6R}}{\partial I_{1R}}\right) \end{array}\right] \end{bmatrix} \begin{bmatrix} V^0_{1R} \\ V^0_{1I} \end{bmatrix}$$

$$\mathbf{D_1}(4,4) = \begin{bmatrix} \left[\begin{array}{cccc} \left(\frac{\partial q^0_{8I}}{\partial I_{1I}} + \frac{\partial q^0_{2I}}{\partial I_{1I}}\right) & \left(\frac{\partial q^0_{2R}}{\partial I_{1I}} - \frac{\partial q^0_{8R}}{\partial I_{1I}}\right) & \left(\frac{\partial q^0_{10I}}{\partial I_{1I}}\right) & \left(\frac{\partial q^0_{0}}{\partial I_{1I}} - \frac{\partial q^0_{10R}}{\partial I_{1I}}\right) \end{array}\right] V^0_{35} \\ + \left[\begin{array}{cc} \left(\frac{\partial q^0_{6I}}{\partial I_{1R}} + \frac{\partial q^0_{4I}}{\partial I_{1R}}\right) & \left(\frac{\partial q^0_{4R}}{\partial I_{1R}} - \frac{\partial q^0_{6R}}{\partial I_{1I}}\right) \end{array}\right] \end{bmatrix} \begin{bmatrix} V^0_{1R} \\ V^0_{1I} \end{bmatrix}$$

Elements of matrix $\mathbf{E_1}$ are,

$$\mathbf{E_1}(1,1) = \begin{bmatrix} \left[\begin{array}{cccc} \left(\frac{\partial q^0_{6R}}{\partial \alpha} + \frac{\partial q^0_{0}}{\partial \alpha}\right) & \left(\frac{\partial q^0_{6I}}{\partial \alpha}\right) & \left(\frac{\partial q^0_{8R}}{\partial \alpha} + \frac{\partial q^0_{2R}}{\partial \alpha}\right) & \left(\frac{\partial q^0_{8I}}{\partial \alpha} + \frac{\partial q^0_{2I}}{\partial \alpha}\right) \end{array}\right] V^0_{35} \\ + \left[\begin{array}{cc} \left(\frac{\partial q^0_{4R}}{\partial \alpha} + \frac{\partial q^0_{2R}}{\partial \alpha}\right) & \left(\frac{\partial q^0_{4I}}{\partial \alpha} - \frac{\partial q^0_{2I}}{\partial \alpha}\right) \end{array}\right] \end{bmatrix} \begin{bmatrix} V^0_{1R} \\ V^0_{1I} \end{bmatrix}$$

$$\mathbf{E_1}(2,1) = \begin{bmatrix} \left[\begin{array}{cccc} \left(\frac{\partial q^0_{6I}}{\partial \alpha}\right) & \left(\frac{\partial q^0_{0}}{\partial \alpha} - \frac{\partial q^0_{6R}}{\partial \alpha}\right) & \left(\frac{\partial q^0_{8I}}{\partial \alpha} - \frac{\partial q^0_{2I}}{\partial \alpha}\right) & \left(\frac{\partial q^0_{2R}}{\partial \alpha} - \frac{\partial q^0_{8R}}{\partial \alpha}\right) \end{array}\right] V^0_{35} \\ + \left[\begin{array}{cc} \left(\frac{\partial q^0_{4I}}{\partial \alpha} + \frac{\partial q^0_{2I}}{\partial \alpha}\right) & \left(\frac{\partial q^0_{2R}}{\partial \alpha} - \frac{\partial q^0_{4R}}{\partial \alpha}\right) \end{array}\right] \end{bmatrix} \begin{bmatrix} V^0_{1R} \\ V^0_{1I} \end{bmatrix}$$

$$\mathbf{E_1}(3,1) = \begin{bmatrix} \left[\begin{array}{cccc} \left(\frac{\partial q^0_{8R}}{\partial \alpha} + \frac{\partial q^0_{2R}}{\partial \alpha}\right) & \left(\frac{\partial q^0_{8I}}{\partial \alpha} - \frac{\partial q^0_{2I}}{\partial \alpha}\right) & \left(\frac{\partial q^0_{10R}}{\partial \alpha} + \frac{\partial q^0_{0}}{\partial \alpha}\right) & \left(\frac{\partial q^0_{10I}}{\partial \alpha}\right) \end{array}\right] V^0_{35} \\ + \left[\begin{array}{cc} \left(\frac{\partial q^0_{6R}}{\partial \alpha} + \frac{\partial q^0_{4R}}{\partial \alpha}\right) & \left(\frac{\partial q^0_{6I}}{\partial \alpha} - \frac{\partial q^0_{4I}}{\partial \alpha}\right) \end{array}\right] \end{bmatrix} \begin{bmatrix} V^0_{1R} \\ V^0_{1I} \end{bmatrix}$$

$$\mathbf{E_1}(4,1) = \begin{bmatrix} \left[\begin{array}{cccc} \left(\frac{\partial q^0_{8I}}{\partial \alpha} + \frac{\partial q^0_{2I}}{\partial \alpha}\right) & \left(\frac{\partial q^0_{2R}}{\partial \alpha} - \frac{\partial q^0_{8R}}{\partial \alpha}\right) & \left(\frac{\partial q^0_{10I}}{\partial \alpha}\right) & \left(\frac{\partial q^0_{0}}{\partial \alpha} - \frac{\partial q^0_{10R}}{\partial \alpha}\right) \end{array}\right] V^0_{35} \\ + \left[\begin{array}{cc} \left(\frac{\partial q^0_{6I}}{\partial \alpha} + \frac{\partial q^0_{2R}}{\partial \alpha}\right) & \left(\frac{\partial q^0_{4R}}{\partial \alpha} - \frac{\partial q^0_{6R}}{\partial \alpha}\right) \end{array}\right] \end{bmatrix} \begin{bmatrix} V^0_{1R} \\ V^0_{1I} \end{bmatrix}$$

Elements of matrix $\mathbf{F_1}$ are,

$$\mathbf{F_1}(1,3) = \begin{bmatrix} \left[ \left(\frac{\partial q^0_{6R}}{\partial \delta_m} + \frac{\partial q^0_0}{\partial \delta_m}\right) \left(\frac{\partial q^0_{6I}}{\partial \delta_m}\right) \left(\frac{\partial q^0_{8R}}{\partial \delta_m} + \frac{\partial q^0_{2R}}{\partial \delta_m}\right) \left(\frac{\partial q^0_{8I}}{\partial \delta_m} + \frac{\partial q^0_{2I}}{\partial \delta_m}\right) \right] V^0_{35} \\ + \left[ \left(\frac{\partial q^0_{4R}}{\partial \delta_m} + \frac{\partial q^0_{2R}}{\partial \delta_m}\right) \left(\frac{\partial q^0_{4I}}{\partial \delta_m} - \frac{\partial q^0_{2I}}{\partial \delta_m}\right) \right] \end{bmatrix} \begin{bmatrix} V^0_{1R} \\ V^0_{1I} \end{bmatrix}$$

$$\mathbf{F_1}(2,3) = \begin{bmatrix} \left[ \left(\frac{\partial q^0_{6I}}{\partial \delta_m}\right) \left(\frac{\partial q^0_0}{\partial \delta_m} - \frac{\partial q^0_{6R}}{\partial \delta_m}\right) \left(\frac{\partial q^0_{8I}}{\partial \delta_m} - \frac{\partial q^0_{2I}}{\partial \delta_m}\right) \left(\frac{\partial q^0_{2R}}{\partial \delta_m} - \frac{\partial q^0_{8R}}{\partial \delta_m}\right) \right] V^0_{35} \\ + \left[ \left(\frac{\partial q^0_{4I}}{\partial \delta_m} + \frac{\partial q^0_{2I}}{\partial \delta_m}\right) \left(\frac{\partial q^0_{2R}}{\partial \delta_m} - \frac{\partial q^0_{4R}}{\partial \delta_m}\right) \right] \end{bmatrix} \begin{bmatrix} V^0_{1R} \\ V^0_{1I} \end{bmatrix}$$

$$\mathbf{F_1}(3,3) = \begin{bmatrix} \left[ \left(\frac{\partial q^0_{8R}}{\partial \delta_m} + \frac{\partial q^0_{2R}}{\partial \delta_m}\right) \left(\frac{\partial q^0_{8I}}{\partial \delta_m} - \frac{\partial q^0_{2I}}{\partial \delta_m}\right) \left(\frac{\partial q^0_{10R}}{\partial \delta_m} + \frac{\partial q^0_0}{\partial \delta_m}\right) \left(\frac{\partial q^0_{10I}}{\partial \delta_m}\right) \right] V^0_{35} \\ + \left[ \left(\frac{\partial q^0_{6R}}{\partial \delta_m} + \frac{\partial q^0_{4R}}{\partial \delta_m}\right) \left(\frac{\partial q^0_{6I}}{\partial \delta_m} - \frac{\partial q^0_{4I}}{\partial \delta_m}\right) \right] \end{bmatrix} \begin{bmatrix} V^0_{1R} \\ V^0_{1I} \end{bmatrix}$$

$$\mathbf{F_1}(4,3) = \begin{bmatrix} \left[ \left(\frac{\partial q^0_{8I}}{\partial \delta_m} + \frac{\partial q^0_{2I}}{\partial \delta_m}\right) \left(\frac{\partial q^0_{2R}}{\partial \delta_m} - \frac{\partial q^0_{8R}}{\partial \delta_m}\right) \left(\frac{\partial q^0_{10I}}{\partial \delta_m}\right) \left(\frac{\partial q^0_0}{\partial \delta_m} - \frac{\partial q^0_{10R}}{\partial \delta_m}\right) \right] V^0_{35} \\ + \left[ \left(\frac{\partial q^0_{6I}}{\partial \delta_m} + \frac{\partial q^0_{2R}}{\partial \delta_m}\right) \left(\frac{\partial q^0_{4R}}{\partial \delta_m} - \frac{\partial q^0_{6R}}{\partial \delta_m}\right) \right] \end{bmatrix} \begin{bmatrix} V^0_{1R} \\ V^0_{1I} \end{bmatrix}$$

Elements of matrix $\mathbf{G_1}$ are,

$\mathbf{G_1}(1,1) = q^0_{6R} + q^0_0 - 9LC\omega^2_0$ $\quad$ $\mathbf{G_1}(1,2) = q^0_{6I}$ $\quad$ $\mathbf{G_1}(1,3) = q^0_{8R} + q^0_{2R}$

$\mathbf{G_1}(1,4) = q^0_{8I} + q^0_{2I}$ $\quad$ $\mathbf{G_1}(2,1) = q^0_{6I}$ $\quad$ $\mathbf{G_1}(2,2) = q^0_0 - q^0_{6R} - 9LC\omega^2_0$

$\mathbf{G_1}(2,3) = q^0_{8I} - q^0_{2I}$ $\quad$ $\mathbf{G_1}(2,4) = q^0_{2R} - q^0_{8R}$ $\quad$ $\mathbf{G_1}(3,1) = q^0_{8R} + q^0_{2R}$

$\mathbf{G_1}(3,2) = q^0_{8I} - q^0_{2I}$ $\quad$ $\mathbf{G_1}(3,3) = q^0_{10R} + q^0_0 - 25LC\omega^2_0$ $\quad$ $\mathbf{G_1}(3,4) = q^0_{10I}$

$\mathbf{G_1}(4,1) = q^0_{8I} + q^0_{2I}$ $\quad$ $\mathbf{G_1}(4,2) = q^0_{2R} - q^0_{8R}$ $\quad$ $\mathbf{G_1}(4,3) = q^0_{10I}$

$\mathbf{G_1}(4,4) = q^0_0 - q^0_{10R} - 25LC\omega^2_0$

where,

$$\mathbf{V^0_{35}} = \begin{bmatrix} (q^0_{6R} + q^0_0 - 9LC\omega^2_0) & (q^0_{6I}) & (q^0_{8R} + q^0_{2R}) & (q^0_{8I} + q^0_{2I}) \\ (q^0_{6I}) & (q^0_0 - q^0_{6R} - 9LC\omega^2_0) & (q^0_{8I} - q^0_{2I}) & (q^0_{2R} - q^0_{8R}) \\ (q^0_{8R} + q^0_{2R}) & (q^0_{8I} - q^0_{2I}) & (q^0_{10R} + q^0_0 - 25LC\omega^2_0) & (q^0_{10I}) \\ (q^0_{8I} + q^0_{2I}) & (q^0_{2R} - q^0_{8R}) & (q^0_{10I}) & (q^0_0 - q^0_{10R} - 25LC\omega^2_0) \end{bmatrix}^{-1}$$

$$\times \begin{bmatrix} (-q^0_{4R} - q^0_{2R}) & (q^0_{2I} - q^0_{4I}) \\ (-q^0_{4I} - q^0_{2I}) & (q^0_{4R} - q^0_{2R}) \\ (-q^0_{6R} - q^0_{4R}) & (q^0_{4I} - q^0_{6I}) \\ (-q^0_{6I} - q_{4I^0}) & (q^0_{6R} - q^0_{4R}) \end{bmatrix}$$

$$\frac{\partial q^0_{kR}}{\partial I_{1R}} = \frac{2}{\pi}\frac{\partial \beta^0}{\partial I_{1R}}\Big\{\cos\big(\frac{k\sigma}{2} + k(\zeta+\phi)\big)\Big\} \qquad \frac{\partial q^0_{kI}}{\partial I_{1R}} = \frac{-2}{\pi}\frac{\partial \beta^0}{\partial I_{1R}}\Big\{\sin\big(\frac{k\sigma}{2} + k(\zeta+\phi)\big)\Big\}$$

$$\frac{\partial q^0_{kR}}{\partial I_{1I}} = \frac{2}{\pi}\frac{\partial \beta^0}{\partial I_{1I}}\Big\{\cos\big(\frac{k\sigma}{2} + k(\zeta+\phi)\big)\Big\} \qquad \frac{\partial q^0_{kI}}{\partial I_{1I}} = \frac{-2}{\pi}\frac{\partial \beta^0}{\partial I_{1I}}\Big\{\sin\big(\frac{k\sigma}{2} + k(\zeta+\phi)\big)\Big\}$$

$$\frac{\partial q^0_{kR}}{\partial \alpha^*} = \frac{-2}{\pi}\cos\big(k(\zeta+\phi)\big)\cos\big(\frac{k\sigma}{2}\big) \qquad \frac{\partial q^0_{kI}}{\partial \alpha^*} = \frac{2}{\pi}\sin\big(k(\zeta+\phi)\big)\cos\big(\frac{k\sigma}{2}\big)$$

$$\frac{\partial q^0_{kR}}{\partial \delta_m} = \frac{2}{\pi}\cos\big(k(\zeta+\phi)\big)\cos\big(\frac{k\sigma}{2}\big) \qquad \frac{\partial q^0_{kI}}{\partial \delta_m} = \frac{-2}{\pi}\sin\big(k(\zeta+\phi)\big)\cos\big(\frac{k\sigma}{2}\big)$$

$$\frac{\partial q^0_0}{\partial I_{1I}} = \frac{2}{\pi}\frac{\partial \beta^0}{\partial I_{1I}} \qquad \frac{\partial q^0_0}{\partial I_{1R}} = \frac{2}{\pi}\frac{\partial \beta^0}{\partial I_{1R}}$$

$$\frac{\partial q^0_0}{\partial \alpha^*} = \frac{-2}{\pi} \qquad \frac{\partial q^0_0}{\partial \delta_m} = \frac{2}{\pi}$$

Note that the initial value of $\phi$ is 0 and therefore, the initial value of $\sigma = \pi - 2\alpha$.

$$\beta = \angle I_1$$

$$\frac{\partial \beta^0}{\partial I_{1R}} = \frac{I^0_{1I}}{|I^0_1|^2} \qquad \frac{\partial \beta^0}{\partial I_{1I}} = \frac{-I^0_{1R}}{|I^0_1|^2}$$

Note: Superscript $^0$ denotes the initial values of the respective variable

Elements of the output matrix of the TCSC $\mathbf{C_{tcsc}}$ are,

$$\mathbf{C_{tcsc}} = \begin{bmatrix} 1 & 0 & 0 & 0 \\ 0 & 1 & 0 & 0 \end{bmatrix}$$

# Appendix B

# Linearized Model of the Synchronous Generator

Linearized dq axis currents ($i_d$ and $i_q$) of the generator can be expressed as,

$$\Delta i_d = K_{\Delta i_d,\Delta\psi_d}\Delta\psi_d + K_{\Delta i_d,\Delta\psi_{fd}}\Delta\psi_{fd} + K_{\Delta i_d,\Delta\psi_{1d}}\Delta\psi_{1d}$$

$$\Delta i_q = K_{\Delta i_q,\Delta\psi_q}\Delta\psi_q + K_{\Delta i_q,\Delta\psi_{1q}}\Delta\psi_{1q} + K_{\Delta i_q,\Delta\psi_{2q}}\Delta\psi_{2q}$$

where,

$$K_{\Delta i_d,\Delta\psi_d} = \frac{-L_{ad}L''_d(L_{fd}+L_{1d})}{L_l L_d L_{fd} L_{1d}} - \frac{1}{L_d} \qquad K_{\Delta i_q,\Delta\psi_q} = \frac{-L_{aq}L''_q(L_{1q}+L_{2q})}{L_l L_q L_{1q} L_{2q}} - \frac{1}{L_q}$$

$$K_{\Delta i_d,\Delta\psi_{fd}} = \frac{L''_d}{L_l L_{fd}} \qquad K_{\Delta i_q,\Delta\psi_{1q}} = \frac{L''_q}{L_l L_{1q}}$$

$$K_{\Delta i_d,\Delta\psi_{1d}} = \frac{L^{"}_d}{L_l L_{1d}} \qquad K_{\Delta i_q,\Delta\psi_{2q}} = \frac{L^{"}_q}{L_l L_{2q}}$$

Elements of the state matrix of the generator $\mathbf{A_g}$ are,

$$\mathbf{A_g}(1,1) = \omega_0 R_a K^0_{\Delta i_d, \Delta\psi_d} \qquad \mathbf{A_g}(1,2) = \omega_0 \qquad \mathbf{A_g}(1,3) = \omega_0 R_a K^0_{\Delta i_d, \Delta\psi_{fd}}$$

$$\mathbf{A_g}(1,4) = \omega_0 R_a K^0_{\Delta i_d, \Delta\psi_{1d}} \qquad \mathbf{A_g}(1,7) = \omega_0 \psi^0_q \qquad \mathbf{A_g}(1,8) = \omega_0 e^0_q$$

$$\mathbf{A_g}(2,1) = -\omega_0 \qquad \mathbf{A_g}(2,2) = -\omega_0 R_a K^0_{\Delta i_q, \Delta\psi_q} \qquad \mathbf{A_g}(2,5) = -\omega_0 R_a K^0_{\Delta i_q, \Delta\psi_{1q}}$$

$$\mathbf{A_g}(2,6) = -\omega_0 R_a K^0_{\Delta i_q, \Delta\psi_{2q}} \qquad \mathbf{A_g}(2,7) = -\omega_0 \psi^0_d \qquad \mathbf{A_g}(2,8) = -\omega_0 e^0_d$$

$$\mathbf{A_g}(3,1) = \frac{\omega_0 R_{fd} L^{"}_d}{L_{fd} L_l} \qquad \mathbf{A_g}(3,3) = \frac{-\omega_0 R_{fd} L^{"}_d}{L_{fd}} \left( \frac{1}{L_l} + \frac{1}{L_{ad}} + \frac{1}{L_{ld}} \right)$$

$$\mathbf{A_g}(3,4) = \frac{\omega_0 R_{fd} L^{"}_d}{L_{fd} L_{1d}} \qquad \mathbf{A_g}(4,1) = \frac{\omega_0 R_{1d} L^{"}_d}{L_{1d} L_l}$$

$$\mathbf{A_g}(4,3) = \frac{\omega_0 R_{1d} L^{"}_d}{L_{1d} L_{fd}} \qquad \mathbf{A_g}(4,4) = \frac{-\omega_0 R_{1d} L^{"}_d}{L_{1d}} \left( \frac{1}{L_l} + \frac{1}{L_{ad}} + \frac{1}{L_{fd}} \right)$$

$$\mathbf{A_g}(5,2) = \frac{\omega_0 R_{1q} L^{"}_q}{L_{1q} L_l} \qquad \mathbf{A_g}(5,5) = \frac{-\omega_0 R_{1q} L^{"}_q}{L_{1q}} \left( \frac{1}{L_l} + \frac{1}{L_{aq}} + \frac{1}{L_{2q}} \right)$$

$$\mathbf{A_g}(5,6) = \frac{\omega_0 R_{1q} L^{"}_q}{L_{1q} L_{2q}} \qquad \mathbf{A_g}(6,2) = \frac{\omega_0 R_{2q} L^{"}_q}{L_{2q} L_l}$$

$$\mathbf{A_g}(6,5) = \frac{\omega_0 R_{2q} L^{"}_q}{L_{1q} L_{2q}} \qquad \mathbf{A_g}(6,6) = \frac{-\omega_0 R_{2q} L^{"}_q}{L_{2q}} \left( \frac{1}{L_l} + \frac{1}{L_{aq}} + \frac{1}{L_{1q}} \right)$$

$$\mathbf{A_g}(7,1) = \frac{1}{2H_1} \left( -i^0_q + \psi^0_q K_{\Delta i_d, \Delta\psi_d} \right) \qquad \mathbf{A_g}(7,2) = \frac{1}{2H_1} \left( i^0_d - \psi^0_d K_{\Delta i_q, \Delta\psi_q} \right)$$

$$\mathbf{A_g}(7,3) = \frac{1}{2H_1} \psi^0_q K_{\Delta i_d, \Delta\psi_{fd}} \qquad \mathbf{A_g}(7,4) = \frac{1}{2H_1} \psi^0_q K_{\Delta i_d, \Delta\psi_{1d}}$$

$$\mathbf{A_g}(7,5) = \frac{-1}{2H_1} \psi^0_d K_{\Delta i_q, \Delta\psi_{1q}} \qquad \mathbf{A_g}(7,6) = \frac{-1}{2H_1} \psi^0_d K_{\Delta i_q, \Delta\psi_{2q}}$$

$$\mathbf{A_g}(7,7) = \frac{-D_1}{2H_1} \qquad \mathbf{A_g}(7,8) = \frac{-K_{12}}{2H_1}$$

$$\mathbf{A_g}(7,10) = \frac{K_{12}}{2H_1} \qquad \mathbf{A_g}(8,7) = \omega_0$$

$$\mathbf{A_g}(9,8) = \frac{K_{12}}{2H_2} \qquad \mathbf{A_g}(9,9) = \frac{-D_2}{2H_2}$$

$$\mathbf{A_g}(9,10) = -\frac{K_{23}+K_{12}}{2H_2} \qquad \mathbf{A_g}(9,12) = \frac{K_{23}}{2H_2}$$

$$\mathbf{A_g}(10,9) = \omega_0 \qquad \mathbf{A_g}(11,10) = \frac{K_{23}}{2H_3}$$

$$\mathbf{A_g}(11,11) = \frac{-D_3}{2H_3} \qquad \mathbf{A_g}(11,12) = -\frac{K_{23}+K_{34}}{2H_3}$$

$$\mathbf{A_g}(11,14) = \frac{K_{34}}{2H_3} \qquad \mathbf{A_g}(12,11) = \omega_0$$

$$\mathbf{A_g}(13,12) = \frac{K_{34}}{2H_4} \qquad \mathbf{A_g}(13,13) = \frac{-D_4}{2H_4}$$

$$\mathbf{A_g}(13,14) = -\frac{K_{45}+K_{34}}{2H_4} \qquad \mathbf{A_g}(13,16) = \frac{K_{45}}{2H_4}$$

$$\mathbf{A_g}(14,13) = \omega_0 \qquad \mathbf{A_g}(15,14) = \frac{K_{45}}{2H_5}$$

$$\mathbf{A_g}(15,15) = \frac{-D_5}{2H_5} \qquad \mathbf{A_g}(15,16) = \frac{-K_{45}}{2H_5}$$

$$\mathbf{A_g}(16,15) = \omega_0$$

Elements of the generator input matrix $\mathbf{B_g}$ are,

$$\mathbf{B_g}(3,1) = \frac{\omega_0 R_{fd}}{L_{ad}} \qquad \mathbf{B_g}(9,2) = \frac{T_{LP_A(\%)}}{2H_2}$$

$$\mathbf{B_g}(11,2) = \frac{T_{LP_B(\%)}}{2H_3} \qquad \mathbf{B_g}(13,2) = \frac{T_{IP(\%)}}{2H_4}$$

$$\mathbf{B_g}(15,2) = \frac{T_{HP(\%)}}{2H_5}$$

Elements of the generator interface voltage matrix $\mathbf{E_g}$ are,

$$\mathbf{E_g}(1,1) = \omega_0 \sin\delta_0 \qquad \mathbf{E_g}(1,2) = -\omega_0 \cos\delta_0$$

$$\mathbf{E_g}(2,1) = \omega_0 \cos\delta_0 \qquad \mathbf{E_g}(2,2) = \omega_0 \sin\delta_0$$

Elements of the generator output current matrix $\mathbf{C_g}$ are,

$$\mathbf{C_g}(1,1) = \sin(\delta^0)K_{\Delta i_d,\Delta\psi_d} \qquad \mathbf{C_g}(2,1) = -\cos(\delta^0)K_{\Delta i_d,\Delta\psi_d}$$

$$\mathbf{C_g}(1,2) = \cos(\delta^0)K_{\Delta i_q,\Delta\psi_q} \qquad \mathbf{C_g}(2,2) = \sin(\delta^0)K_{\Delta i_q,\Delta\psi_q}$$

$$\mathbf{C_g}(1,3) = \sin(\delta^0)K_{\Delta i_d,\Delta\psi_{fd}} \qquad \mathbf{C_g}(2,3) = -\cos(\delta^0)K_{\Delta i_d,\Delta\psi_{fd}}$$

$$\mathbf{C_g}(1,4) = \sin(\delta^0)K_{\Delta i_d,\Delta\psi_{1d}} \qquad \mathbf{C_g}(2,4) = -\cos(\delta^0)K_{\Delta i_d,\Delta\psi_{1d}}$$

$$\mathbf{C_g}(1,5) = \cos(\delta^0)K_{\Delta i_q,\Delta\psi_{1q}} \qquad \mathbf{C_g}(2,5) = \sin(\delta^0)K_{\Delta i_q,\Delta\psi_{1q}}$$

$$\mathbf{C_g}(1,6) = \cos(\delta^0)K_{\Delta i_q,\Delta\psi_{2q}} \qquad \mathbf{C_g}(2,6) = \sin(\delta^0)K_{\Delta i_q,\Delta\psi_{2q}}$$

$$\mathbf{C_g}(1,8) = -I^0_{gI} \qquad \mathbf{C_g}(2,8) = I^0_{gR}$$

# Appendix C

# Wind Power Plant Test system Data

Table C.1: WPP test system data

| Parameter | Value |
|---|---|
| **Operating conditions** | |
| Initial wind speed | $12ms^{-1}$ |
| Stator reactive power | 0.1pu |
| GSC power factor | 1 |
| **Wind turbine parameters** | |
| Rated Power ($S_{-1}$) | 2MW |
| Blade length | 37.5m |
| Performance coefficient ($C_p$) | 0.25 |
| Air density ($\rho$) | 1.225 $kgm^{-3}$ |
| Wind Speed/rotor speed | 10.909 |
| No of Wind turbines | 100 |
| **Generator parameters** | |
| Rated Voltage | 690V |
| Base MVA | 2MVA |
| Stator resistance | 0.001164 Ω |
| Rotor resistance | 0.00131 Ω |
| Stator leakage inductance | 0.0584 mH |
| Rotor leakage inductance | 0.0629 mH |
| Mutual inductance | 2.4961 mH |

| Parameter | Value |
|---|---|
| **DC Capacitor and Unit transformer parameters** | |
| DC Capacitance | 25 mF |
| DC Voltage | 1000 V |
| Converter transformer base | 0.3*S0 |
| Transformer leakage reactance | 0.1 pu |
| **Drive Train Parameters** | |
| Blade inertia | 4 s |
| Hub inertia | 0.3 s |
| Generator inertia | 0.42 s |
| Shaft stiffness constants | 0.3 (pu T/rad) |
| **Internal Network Parameters** | |
| Internal network voltage | 33 kV |
| POC Transformer MVA | 200 MVA |
| POC transformer leakage reactance | 0.06 pu |
| Internal network resistance | 0.4713 Ω |
| Internal network reactance | 0.7766 Ω |
| Internal network suceptance | $5.42 \times 10^{-4}$S |
| **Transmission line parameters** | |
| Line resistance | 0.05 Ω/km |
| Line inductance | 1.3mH Ω/km |
| Line Capacitance | 0.0089 $\mu$/km |
| Line length | 400 km |
| Transmission Voltage | 230 kV |
| **Rotor Side Converter (RSC) controller parameters** | |
| DFIG stator reactive power controller proportional gain ($K_{pQs}$) | 0.5 |
| DFIG stator reactive power controller integral gain ($K_{iQs}$) | 2.5 |
| DFIG speed controller proportional gain ($K_{pws}$) | 50 |
| DFIG speed controller integral gain ($K_{iws}$) | 62.5 |
| d axis Inner current controller proportional gain ($K_{pdr}$) | 0.115 |
| d axis Inner current controller integral gain ($K_{idr}$) | 2.3 |
| q axis Inner current controller proportional gain ($K_{pqr}$) | 0.115 |
| q axis Inner current controller integral gain ($K_{iqr}$) | 2.3 |
| **Grid Side Converter (GSC) controller parameters** | |
| DC capacitor voltage controller proportional gain ($K_{pdc}$) | 5 |
| DC capacitor voltage controller controller integral gain ($K_{idc}$) | 250 |
| GSC reactive power controller proportional gain ($K_{pQg}$) | 10 |
| GSC reactive power controller integral gain ($K_{iQg}$) | 100 |
| d axis Inner current controller proportional gain ($K_{pdg}$) | 1 |
| d axis Inner current controller integral gain ($K_{idg}$) | 200 |
| q axis Inner current controller proportional gain ($K_{pqg}$) | 1 |
| q axis Inner current controller integral gain ($K_{iqg}$) | 100 |

# Appendix D

# Frequency Scanning Test System Data

Table D.1: Generator Electrical Data

| Parameter | Generator 1 | Generator 2 | Generator 3 |
|---|---|---|---|
| MVA | 384 | 590 | 892.4 |
| kV | 24 | 22 | 26 |
| T'do (s) | 5.2000 | 4.2000 | 4.3000 |
| T"do (s) | 0.042 | 0.032 | 0.0320 |
| T'qo (s) | 1.5000 | 0.5650 | 0.8500 |
| T"qo (s) | 0.0420 | 0.062 | 0.0500 |
| H (s) | 2.6200 | 2.3186 | 0.8685 |
| D | 0.0000 | 0.0000 | 0.0000 |
| Xd (pu) | 1.798 | 2.1100 | 1.7900 |
| Xq (pu) | 1.778 | 2.0200 | 1.7100 |
| X'd (pu) | 0.324 | 0.2800 | 0.1690 |
| X'q (pu) | 1.0000 | 0.4900 | 0.2280 |
| X"d (pu) | 0.2600 | 0.2150 | 0.1350 |
| X"q (pu) | 0.2600 | 0.2150 | 0.1350 |
| Xl (pu) | 0.1930 | 0.1550 | 0.1300 |

Generator impedances are expressed on machine base MVA

Table D.2: Multi-Mass Data of Generator 3

| Component | H (s) | Component | K (pu) |
|---|---|---|---|
| LPA | 0.884215 | Gen-LPA | 26713 |
| LPB | 0.85867 | LPA-LPB | 19618 |
| IP | 0.155589 | LPB-IP | 13168 |
| HP | 0.092897 | IP-HP | 7277 |

Table D.3: Transformer Data

| Parameter | Generator 1 | Generator 2 | Generator 3 |
|---|---|---|---|
| Voltage (kV) | 24/500 | 22/500 | 26/500 |
| Reactance (pu) | 0.12 | 0.13 | 0.14 |
| MVA | 384 | 590 | 892.4 |

Impedances are expressed on machine base MVA

Table D.4: Line Data

| Line | R (pu) | $X_L$ (pu) | $X_C$ (pu) |
|---|---|---|---|
| 2 - 4 | 0.008567 | 0.085670 | 0 |
| 4 - 9 (1) | 0.017134 | 0.17134 | 0.137 |
| 4 - 5 (2) | 0.017134 | 0.17134 | 0.0342 |
| 5 - 7 | 0.004283 | 0.042835 | 0 |
| 7 - 8 | 0.017134 | 0.17134 | 0.119938 |

Impedances are expressed on 100 MVA base

Table D.5: Load Data

| Bus | P (MW) | Q (MVar) |
|---|---|---|
| 5 | 400 | 390 |
| 7 | 330 | 255 |

# Appendix E

# Case Study Test System Data

## E.1 Test System Parameters

Table E.1: Line Data

| Line | R (pu) | $X_L$ (pu) | B (pu) | $X_C$ (pu) |
|---|---|---|---|---|
| 5 - 7 (1) | 0.0074 | 0.08 | 0.2 | 0.064 |
| 5 - 7 (2) | 0.0074 | 0.08 | 0.2 | 0.064 |
| 7 - 8 | 0.0014 | 0.03 | 0.2 | 0 |
| 8 - 4 | 0.0024 | 0.025 | 0.2 | 0 |
| 8 - 6 | 0.004 | 0.06 | 0.2 | 0.042 |
| 4 - 6 | 0.002 | 0.05 | 0.2 | 0.025 |
| 6 - 9 | 0.0036 | 0.07 | 0.2 | 0.035 |

Impedances are expressed on 100 MVA base

Table E.2: Generator Electrical Data

| Parameter | Generator 1 | Generator 2 | Generator 3 |
|---|---|---|---|
| MVA | 892.4 | 960 | 191 |
| kV | 22 | 22 | 22 |
| T'do (s) | 4.3 | 7.9 | 5.9 |
| T"do (s) | 0.032 | 0.032 | 0.033 |
| T'qo (s) | 0.85 | 0.41 | 0.535 |
| T"qo (s) | 0.05 | 0.055 | 0.078 |
| H (s) | 0.868495 | 0.8684328 | 0.946 |
| Ra | 0 | 0.0048 | 0.0026 |
| Xd (pu) | 1.79 | 1.79 | 1.651 |
| Xq (pu) | 1.71 | 1.66 | 1.59 |
| X'd (pu) | 0.169 | 0.355 | 0.232 |
| X'q (pu) | 0.288 | 0.570 | 0.171 |
| X"d (pu) | 0.135 | 0.275 | 0.171 |
| X"q (pu) | 0.2 | 0.275 | 0.380 |
| Xl (pu) | 0.13 | 0.215 | 0.1020 |

Generator impedances are expressed on their machine base MVA

Table E.3: Multi-Mass Data of Generators

| Component | H (s) | | | Component | K (pu) | | |
|---|---|---|---|---|---|---|---|
| | G1 | G2 | G3 | | G1 | G2 | G3 |
| LPA | 0.884215 | 1.427 | 3.68 | Gen-LPA | 26713 | 14043.5 | 31192.2 |
| LPB | 0.85867 | 1.4269 | - | LPA-LPB | 19618 | 11804.2 | 30879.3 |
| IP | 0.155589 | 1.4264 | 0.337 | LPB-IP | 13168 | 10428.2 | - |
| HP | 0.092897 | 0.17553 | 0.099 | IP-HP | 7277 | 6701.5 | 14306.9 |

Table E.4: Transformer Data

| Parameter | T1 | T2 | T3 |
|---|---|---|---|
| Voltage (kV) | 22/500 | 22/500 | 22/500 |
| Reactance (pu) | 0.0224 | 0.02 | 0.02 |
| MVA | 892.4 | 960 | 191 |

Impedances are expressed on 100 MVA

Table E.5: Load Data

| Load | P (MW) | Q (MVar) |
|---|---|---|
| L1 | 250 | 25 |
| L2 | 300 | 150 |
| L3 | 250 | 100 |

## E.2 Controllability Indices

Table E.6: Controllability Indices

| Gen. | Torsional Mode | TCSC at 6-9 | | TCSC at 4-6 | | TCSC at 8-6 | | TCSC at 5-7 | |
|---|---|---|---|---|---|---|---|---|---|
| | | Damp. (%) | Cont. | Damp. (%) | Cont. | Damp. (%) | Cont. | Damp. (%) | Cont. |
| G1 | 16.104 | -0.018 | 4.085 | -0.094 | 2.278 | -0.027 | 0.118 | -0.026 | 0.705 |
| | 25.474 | 0.000 | 0.832 | -0.003 | 0.492 | -0.009 | 0.214 | -0.044 | 1.439 |
| | 32.237 | -0.015 | 2.190 | -0.052 | 0.979 | -0.062 | 1.934 | -0.013 | 0.773 |
| | 47.456 | 0.000 | 0.003 | 0.000 | 0.003 | 0.000 | 0.003 | 0.000 | 0.003 |
| G2 | 8.305 | 0.039 | 2.030 | 0.029 | 0.195 | 0.034 | 1.083 | -0.009 | 0.452 |
| | 15.229 | -0.042 | 1.959 | -0.070 | 0.764 | -0.008 | 0.577 | -0.193 | 2.505 |
| | 20.264 | -0.035 | 1.140 | -0.097 | 1.072 | 0.000 | 0.003 | -0.115 | 2.843 |
| | 23.649 | 0.000 | 0.008 | 0.000 | 0.002 | -0.097 | 1.323 | 0.000 | 0.011 |
| G3 | 19.180 | 0.021 | 0.667 | 0.022 | 0.224 | 0.015 | 0.092 | 0.017 | 0.186 |
| | 23.560 | 0.090 | 0.861 | 0.045 | 3.055 | 0.071 | 1.223 | 0.019 | 3.530 |
| | 29.690 | -0.002 | 0.613 | -0.015 | 0.887 | 0.001 | 0.230 | 0.001 | 0.202 |
| | 52.738 | 0.000 | 0.031 | 0.000 | 0.017 | 0.000 | 0.015 | 0.000 | 0.001 |

# Bibliography

[1] P. Kundur, N. J. Balu, and M. G. Lauby, *"Power system stability and control"*. New York: McGraw-Hill Education, 1994, vol. 7, ch. Sub-Synchronous resonance, pp. 1025–1105.

[2] J. Adams, C. Carter, and S.-H. Huang, "Ercot experience with sub-synchronous control interaction and proposed remediation," in *PES T&D Conf. Expo. 2012*. IEEE, 2012, pp. 1–5.

[3] J. Butler and C. Concordia, "Analysis of series capacitor application problems," *Electrical Engineering*, vol. 56, no. 8, pp. 975–988, 1937.

[4] D. Walker, C. Bowler, R. Jackson, and D. Hodges, "Results of subsynchronous resonance test at Mohave," *IEEE Transactions on Power Apparatus and Systems*, vol. 94, no. 5, pp. 1878–1889, 1975.

[5] C. E. Bowler, D. N. Ewart, and C. Concordia, "Self excited torsional frequency oscillations with series capacitors," *IEEE Transactions on Power Apparatus and Systems*, no. 5, pp. 1688–1695, 1973.

[6] M. Bahrman, E. Larsen, R. Piwko, and H. Patel, "Experience with HVDC-

turbine-generator torsional interaction at Square Butte," *IEEE Transactions on Power Apparatus and Systems*, no. 3, pp. 966–975, 1980.

[7] C. Karawita, "HVDC interaction studies using small signal stability assessment," Ph.D. dissertation, University of Manitoba, 2009.

[8] N. Rostamkolai, R. Piwko, E. Larsen, D. Fisher, M. Mobarak, and A. Poitras, "Subsynchronous interactions with static VAR compensators-concepts and practical implications," *IEEE Transactions on Power Systems*, vol. 5, no. 4, pp. 1324–1332, 1990.

[9] D. Lee, R. Beaulieu, and G. Rogers, "Effects of governor characteristics on turbo-generator shaft torsionals," *IEEE transactions on power apparatus and systems*, no. 6, pp. 1254–1261, 1985.

[10] "Terms, definitions and symbols for subsynchronous oscillations," *IEEE Transactions on Power Apparatus and Systems*, vol. 104, no. 6, pp. 1326–1334, 1985.

[11] "Reader's guide to subsynchronous resonance," in *IEEE Transactions on Power Apparatus and Systems*, vol. 7, no. 1, 1992, pp. 150–157.

[12] J. Shair, X. Xie, L. Wang, W. Liu, J. He, and H. Liu, "Overview of emerging subsynchronous oscillations in practical wind power systems," *Renewable and Sustainable Energy Reviews*, vol. 99, pp. 159–168, 2019.

[13] IEEE SSR Working Group, "Proposed terms and definitions for subsynchronous resonance," *IEEE Transactions on Power Apparatus and Systems*, vol. 2, pp. 506–511, 1980.

[14] L. Wang, X. Xie, Q. Jiang, H. Liu, Y. Li, and H. Liu, "Investigation of SSR in practical DFIG-based wind farms connected to a series-compensated power system," *IEEE Transactions on Power Systems*, vol. 30, no. 5, pp. 2772–2779, 2014.

[15] X. Xie, X. Zhang, H. Liu, H. Liu, Y. Li, and C. Zhang, "Characteristic analysis of subsynchronous resonance in practical wind farms connected to series-compensated transmissions," *IEEE Transactions on Energy Conversion*, vol. 32, no. 3, pp. 1117–1126, 2017.

[16] Y. Li, L. Fan, and Z. Miao, "Replicating real-world wind farm SSR events," *IEEE Transactions on Power Delivery*, vol. 35, no. 1, pp. 339–348, 2019.

[17] Y. Xu and Y. Cao, "Sub-synchronous oscillation in PMSGs based wind farms caused by amplification effect of GSC controller and PLL to harmonics," *IET Renewable Power Generation*, vol. 12, no. 7, pp. 844–850, 2018.

[18] N. Hatziargyriou, J. Milanovic, C. Rahmann, V. Ajjarapu, C. Canizares, I. Erlich, D. Hill, I. Hiskens, I. Kamwa, B. Pal *et al.*, "Definition and classification of power system stability–revisited & extended," *IEEE Transactions on Power Systems*, vol. 36, no. 4, pp. 3271–3281, 2020.

[19] "Guidelines for subsynchronous oscillation studies in power electronics dominated power systems." CIGRE, 2023.

[20] D. H. R. Suriyaarachchi, "Sub-synchronous interactions in a wind integrated power system," Ph.D. dissertation, University of Manitoba, 2014.

[21] R. Piwko and E. Larsen, "HVDC system control for damping of subsynchronous oscillations," *IEEE Transactions on power apparatus and systems*, no. 7, pp. 2203–2211, 1982.

[22] M. S. Annakkage, C. Karawita, and U. D. Annakkage, "Frequency scan based screening method for device dependent sub-synchronous oscillations," *IEEE Transactions on Power Systems*, vol. 31, no. 3, pp. 1872–1878, 2015.

[23] A. M. Liapunov, *Stability of Motion*. Academic Press Inc., 1967.

[24] P. M. Anderson, B. L. Agrawal, and J. E. Van Ness, *Subsynchronous resonance in power systems*. John Wiley & Sons, 1999, vol. 9.

[25] I. Canay, "A novel approach to the torsional interaction and electrical damping of the synchronous machine part I: Theory," *IEEE Transactions on Power Apparatus and Systems*, no. 10, pp. 3630–3638, 1982.

[26] N. Prabhu and K. Padiyar, "Investigation of subsynchronous resonance with VSC-based HVDC transmission systems," *IEEE Transactions on Power Delivery*, vol. 24, no. 1, pp. 433–440, 2008.

[27] D. H. Baker, G. E. Boukarim, R. D'Aquila, and R. J. Piwko, "Subsynchronous resonance studies and mitigation methods for series capacitor applications," in *Proc. Inaugural IEEE PES Conference and Exposition in Africa*. IEEE, 2005, pp. 386–392.

[28] "Countermeasures to subsynchronous resonance problems," *Trans. on Power Apatatus and Systems*, vol. PAS-99, no. 5, pp. 1810–1818, 1980.

[29] R. Farmer, A. Schwalb, and E. Katz, "Navajo project report on subsynchronous resonance analysis and solutions," *IEEE Transactions on Power Apparatus and Systems*, vol. 96, no. 4, pp. 1226–1232, 1977.

[30] C. Bowler, D. Baker, N. Mincer, and P. Vandiveer, "Operation and test of the navajo SSR protective equipment," *IEEE Transactions on Power Apparatus and Systems*, no. 4, pp. 1030–1035, 1978.

[31] L. Kilgore, D. Ramey, and W. South, "Dynamic filter and other solutions to the subsynchronous resonance problem," in *Proc. Am. Power Conf.(United States)*, vol. 37. Westinghouse Electric Corp., East Pittsburgh, PA, 1975.

[32] R. Hedin, K. Stump, and N. Hingornai, "A new scheme for subsynchronous resonance damping of torsional oscillations and transient torque-part II, performance," *IEEE Transactions on Power Apparatus and Systems*, no. 4, pp. 1856–1863, 1981.

[33] R. M. Mathur and R. K. Varma, *Thyristor-based FACTS controllers for electrical transmission systems*. John Wiley & Sons, 2002.

[34] X. Zheng, Z. Xu, and J. Zhang, "A supplementary damping controller of TCSC for mitigating SSR," in *2009 IEEE Power & Energy Society General Meeting*. IEEE, 2009, pp. 1–5.

[35] K. Dey, M. K. Das, and A. Kulkarni, "Comparison of dynamic phasor, discrete-time and frequency scanning based SSR models of a TCSC," *Electric Power Systems Research*, vol. 196, p. 107237, 2021.

[36] S. Joshi, E. Cheriyan, and A. Kulkarni, "Output feedback SSR damping controller design based on modular discrete-time dynamic model of TCSC," *IET generation, transmission & distribution*, vol. 3, no. 6, pp. 561–573, 2009.

[37] R. Zheng, T. Joseph, S. Wang, and J. Liang, "A control strategy for TCSC to mitigate SSR with local measurements," 2017.

[38] W. Zhu, R. Spee, R. Mohler, G. Alexander, W. Mittelstadt, and D. Maratukulam, "An EMTP study of SSR mitigation using the thyristor controlled series capacitor," *IEEE Transactions on Power Delivery*, vol. 10, no. 3, pp. 1479–1485, 1995.

[39] L. A. Pilotto, A. Bianco, W. F. Long, and A.-A. Edris, "Impact of TCSC Slaat control methodologies on subsynchronous oscillations," *IEEE transactions on Power Delivery*, vol. 18, no. 1, pp. 243–252, 2003.

[40] R. Piwko, C. Wegner, S. Kinney, and J. Eden, "Subsynchronous resonance performance tests of the Slatt thyristor-controlled series capacitor," *IEEE Transactions on Power Delivery*, vol. 11, no. 2, pp. 1112–1119, 1996.

[41] S. Subhash, B. Sarkar, and K. Padiyar, "A novel control strategy for TCSC to damp subsynchronous oscillations," in *Seventh International Conference on AC-DC Power Transmission*. IET, 2001, pp. 181–186.

[42] N. Christl, "Advanced series compensation (ASC) with thyristor controlled impedance," *Cigré paper*, pp. 14–37, 1992.

[43] S. Nyati, C. Wegner, R. Delmerico, R. Piwko, D. Baker, and A. Edris, "Effectiveness of thyristor controlled series capacitor in enhancing power system dynamics:

an analog simulator study," *IEEE Transactions on Power Delivery*, vol. 9, no. 2, pp. 1018–1027, 1994.

[44] A. Daneshpooy and A. Gole, "Frequency response of the thyristor controlled series capacitor," *IEEE Transactions on Power Delivery*, vol. 16, no. 1, pp. 53–58, 2001.

[45] K. Kabiri, S. Henschel, and H. W. Dommel, "Resistive behavior of thyristor-controlled series capacitors at subsynchronous frequencies," *IEEE transactions on Power Delivery*, vol. 19, no. 1, pp. 374–379, 2004.

[46] R. Zheng, "SSR mitigation with tcsc in power systems," Ph.D. dissertation, Cardiff University, 2017.

[47] D. Holmberg, M. Danielsson, P. Halvarsson, and L. Angquist, "The stode thyristor controlled series capacitor," *Cigre Paris*, 1998.

[48] L. Ängquist, G. Ingeström, and H.-Å. Jönsson, "Dynamical performance of TCSC schemes," *CIGRE Session–1996, Paper*, pp. 14–302, 1996.

[49] M.-Q. Tran, M.-C. Dinh, S.-J. Lee, J.-I. Lee, M. Park, C. H. Lee, and J. Yoon, "Analysis and mitigation of subsynchronous resonance in a korean power network with the first TCSC installation," *Energies*, vol. 12, no. 15, p. 2847, 2019.

[50] S. G. Jalali, R. H. Lasseter, and I. Dobson, "Dynamic response of a thyristor controlled switched capacitor," *IEEE transactions on Power Delivery*, vol. 9, no. 3, pp. 1609–1615, 1994.

[51] A. Ghosh and G. Ledwich, "Modelling and control of thyristor-controlled series compensators," *IEE Proceedings-Generation, Transmission and Distribution*, vol. 142, no. 3, pp. 297–304, 1995.

[52] R. Rajaraman, I. Dobson, R. H. Lasseter, and Y. Shern, "Computing the damping of subsynchronous oscillations due to a thyristor controlled series capacitor," *IEEE transactions on power delivery*, vol. 11, no. 2, pp. 1120–1127, 1996.

[53] H. A. Othman and L. Angquist, "Analytical modeling of thyristor-controlled series capacitors for SSR studies," *IEEE Transactions on Power Systems*, vol. 11, no. 1, pp. 119–127, 1996.

[54] B. K. Perkins and M. Iravani, "Dynamic modeling of a TCSC with application to SSR analysis," *IEEE transactions on Power systems*, vol. 12, no. 4, pp. 1619–1625, 1997.

[55] K. Kabiri, S. Henschel, J. R. Martí, and H. W. Dommel, "A discrete state-space model for SSR stabilizing controller design for TCSC compensated systems," *IEEE Transactions on power delivery*, vol. 20, no. 1, pp. 466–474, 2005.

[56] S. Joshi and A. Kulkarni, "Comparative evaluation of discrete-time dynamic models of TCSC," in *Proc. 16th Power Systems Computation Conf.*, 2008.

[57] P. Mattavelli, G. C. Verghese, and A. M. Stankovic, "Phasor dynamics of thyristor-controlled series capacitor systems," *IEEE Transactions on Power Systems*, vol. 12, no. 3, pp. 1259–1267, 1997.

[58] P. Mattavelli, A. M. Stankovic, and G. C. Verghese, "SSR analysis with dynamic

phasor model of thyristor-controlled series capacitor," *IEEE Transactions on Power Systems*, vol. 14, no. 1, pp. 200–208, 1999.

[59] T. Demiray, "Simulation of power system dynamics using dynamic phasor models," Ph.D. dissertation, ETH Zurich, 2008.

[60] M. K. Das, "Dq and dynamic phasor based frequency scanning analysis of grid-connected power electronic systems," Ph.D. dissertation, Ph. D thesis, Indian Institute of Technology, Bombay, 2016.

[61] R. Pintelon and J. Schoukens, *System identification: a frequency domain approach*. John Wiley & Sons, 2012.

[62] "First benchmark model for computer simulation of subsynchronous resonance," *IEEE transactions on power apparatus and systems*, vol. 96, no. 5, pp. 1565–1572, 1977.

[63] R. Zheng, G. Li, and J. Liang, "Capability of TCSC on SSR mitigation," *Journal of Power and Energy Engineering*, vol. 3, no. 04, pp. 232–239, 2015.

[64] T. Rauhala, J. Jyrinsalo, and H. Kuisti, "Enhancing the transmission capability using FACTS: The Finnish experience," in *9th IET International Conference on AC and DC Power Transmission (ACDC 2010)*. IET, 2010, pp. 1–5.

[65] "Subsynchronous oscillation risks of wind power plants connecting to finnish series compensated network," 2020.

[66] T. auhala, "Subsynchronous oscillations – aspects and experiences from

Finland," Nov 2016. [Online]. Available: https://energiforskmedia.blob.core.windows.net/media/21858/rauhala_presentation.pdf/

[67] S. Haanpää, "Electricity transmission is monitored at finland's cross-sections," Sep 2022. [Online]. Available: https://www.fingridlehti.fi/en/electricity-transmission-is-monitored-at-finlands-cross-sections/

[68] O.-P. Janhunen, R. Korhonen, L. Linnamaa, A. Kuusela, and T. Rauhala, "Experiences on studies for subsynchronous oscillation risks of wind power plants connected in the vicinity of Finnish series compensated network," Ph.D. dissertation, 2021.

[69] J. Daniel, C. Han, S. Hutchinson, R. Koessler, D. Martin, G. Shen, and W. Willie, "ERCOT CREZ reactive power compensation study," 2010.

[70] B. Agrawal and R. Farmer, "Use of frequency scanning techniques for subsynchronous resonance analysis," *IEEE Transactions on Power Apparatus and Systems*, no. 2, pp. 341–349, 1979.

[71] M. A. Hannan, N. N. Islam, A. Mohamed, M. S. H. Lipu, P. J. Ker, M. M. Rashid, and H. Shareef, "Artificial intelligent based damping controller optimization for the multi-machine power system: A review," *IEEE Access*, vol. 6, pp. 39 574–39 594, 2018.

[72] L. H. Hassan, M. Moghavvemi, H. A. Almurib, K. Muttaqi, and V. G. Ganapathy, "Optimization of power system stabilizers using participation factor and genetic algorithm," *International Journal of Electrical Power & Energy Systems*, vol. 55, pp. 668–679, 2014.

[73] M. Eslami, H. Shareef, M. R. Taha, and M. Khajehzadeh, "Adaptive particle swarm optimization for simultaneous design of UPFC damping controllers," *International Journal of Electrical Power & Energy Systems*, vol. 57, pp. 116–128, 2014.

[74] D. Mondal, A. Chakrabarti, and A. Sengupta, "Optimal placement and parameter setting of SVC and TCSC using PSO to mitigate small signal stability problem," *International Journal of Electrical Power & Energy Systems*, vol. 42, no. 1, pp. 334–340, 2012.